

**Verliezen door spreidingsflux
in permanentemagneetbekerachtigde synchrone machines met axiale flux**

Fringing Flux Losses in Axial Flux Permanent Magnet Synchronous Machines

Bart Scheerlinck

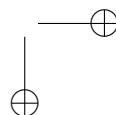
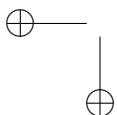
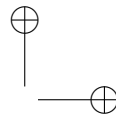
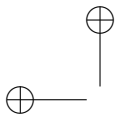
Promotoren: prof. dr. ir. P. Sergeant, prof. dr. ing. L. Cardon
Proefschrift ingediend tot het behalen van de graad van
Doctor in de ingenieurswetenschappen: werktuigkunde-elektrotechniek

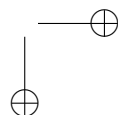
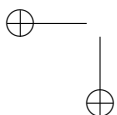
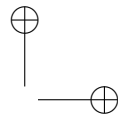
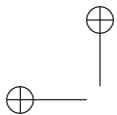


**UNIVERSITEIT
GENT**

Vakgroep Elektrische Energie, Metalen, Mechanische Constructies en Systemen
Voorzitter: prof. dr. ir. L. Dupré
Faculteit Ingenieurswetenschappen en Architectuur
Academiejaar 2016 - 2017

ISBN 978-90-8578-984-0
NUR 959, 978
Wettelijk depot: D/2017/10.500/19





Fringing Flux Losses in Axial Flux Permanent Magnet Synchronous Machines

Bart Scheerlinck

Dissertation submitted to obtain the academic degree of
Doctor of Electromechanical Engineering

Supervisors:

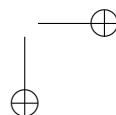
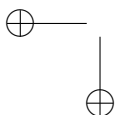
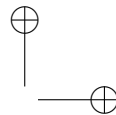
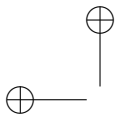
Prof. dr. ir. Peter Sergeant
Department of Electrical Energy, Metals, Mechanical Constructions and Systems
(EEMMeCS)
Faculty of Engineering and Architecture
Ghent University
Tech Lane Ghent Science Park 913
B-9052 Zwijnaarde, Belgium
<http://www.ugent.be/ea/eemmecs/en>

Prof. dr. ing Ludwig Cardon
Department of Materials, Textiles and Chemical Engineering (MaTCh)
Faculty of Engineering and Architecture
Ghent University
Tech Lane Ghent Science Park 915
B-9052 Zwijnaarde, Belgium
<http://www.ugent.be/ea/match/en>

Members of the examining board:

Prof. dr. ir. Patrick De Baets (chairman)
Prof. dr. ir. Alex Van den Bossche (secretary)
Prof. dr. ir. Peter Sergeant (supervisor)
Prof. dr. ing. Ludwig Cardon (supervisor)
Prof. dr. ir. Luc Dupré
Prof. dr. Marc Vanhaelst
Prof. dr. ing. Kurt Stockman
Prof. dr. ir. Johan Gyselinck
Prof. dr. ir. Herbert De Gersem

Ghent University
Ghent University
Ghent University
Ghent University
Ghent University
Ghent University
Ghent University
Université libre de Bruxelles
Technische Universität Darmstadt





Preface

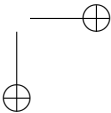
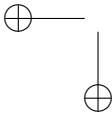
The European Union leaders have made several agreements to continually reduce CO₂ emissions by 2050. For this purpose several initiatives are taken, including the 20-20-20 target, which is a climate and energy package of legislation aimed at ensuring that CO₂ emissions in 2020 decrease by 20%. The goals for 2020 are:

- 20% less CO₂ emissions with respect to 1990
- 20% less energy consumption
- 20% of the total energy consumption must come from renewable energy such as wind and solar power.

Electric motor systems are estimated to account for 46% of global electricity use [1]. Electric motors could be called the workhorses of industry, converting electrical energy to mechanical energy, they drive compressors, rotate pumps, move materials, run fans, blowers, drills or mixers and so on. It is estimated that for industrial applications, motor systems approximately account for 70% of electricity consumption [1]. Small improvements of such huge consumers of electricity, can lead to large energy savings. For this reason, the International Electrotechnical Commission (IEC) introduced four levels of motor efficiency, summarized in the IEC International Standard: IEC 60034-30-1:2014:

- IE1 Standard efficiency
- IE2 High efficiency
- IE3 Premium efficiency
- IE4 Super premium efficiency.

These four IE codes are voluntary and can help regulators to determine the minimum efficiency levels for electric motor energy performance in their regulations. The IEC 60034-30-1 classification system has improved the competition between motor manufacturers and caused massive technological improvements. Although the IEC international standards are voluntary, the IEC classification system is adopted in the European Union (EU) and numerous other countries. The EU



directive 640/2009, which is effective from January 2015 for motors with a rated output from 7,5-375 kW and from 2017 for motors with a rated output from 0,75-375 kW, is generally referred as the EU Minimum Energy Performance Standard (MEPS). This measure, is expected to result in energy efficiency improvements of 20% to 30% [2]. With respect to these legislations, research towards axial flux permanent magnet machines was started at the department of Electrical Energy, Systems and Automation of Ghent University in 2008 by prof. dr. ir. Alex Van den Bossche and prof. dr. ir. Peter Sergeant as a generator in a domestic combined heat and power application [3]. Already at an early stage, the axial flux permanent magnet machine technology showed superior properties such as excellent energy efficiency and high power density. Nevertheless, more research on this machine was necessary. Therefore, a BOF association research project was requested and granted to prof. dr. ir. Peter Sergeant and prof. dr. ing. Ludwig Cardon. This research project would focus on the energy efficiency of axial flux permanent magnet machines.

I would like to acknowledge the Ghent University College for granting the project “Composite Electric Machines” and Ghent University for their financial support by the special research fund (BOF).

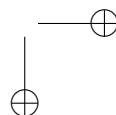
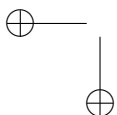
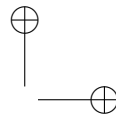
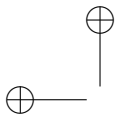
Also special thanks to the people who directly contributed to this research: Prof. dr. ir. Peter Sergeant for his insightful guidance during this research and being my promotor. Prof. dr. ing. Ludwig Cardon for his help in the selection of the material used in the prototype machine and being my co-promotor. Prof. dr. ir. Herbert De Gersem (Technische Universität Darmstadt) for his excellent guidance during this research and his many splendid ideas. Dr. Ir. Hendrik Vansompel for providing me his preliminary research files and the construction of the prototype machine. Prof. dr. ir. Luc Dupré for providing me measurement loss data files and his customized setup. Prof. dr. ir. Joris Degrieck and Dr. Ir. Ives De Baere with the many help on the construction of the prototype machine.

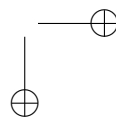
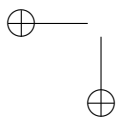
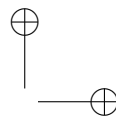
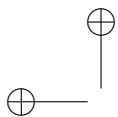
I also like to thank the many friends I made at the research group. I would like to mention Bert Hannon and Jan De Bisschop (who started with me in September 2012) in particular, for the many coffee breaks and good talks towards a PhD.

Also special thanks is given to my family and my girlfriend Lisa, whose steady support and love made me stand strong through the rough times.

At last I like to thank the technicians of Ghent University and all the colleagues of the EESA research group.

Bart Scheerlinck, 16 December 2016



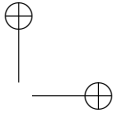
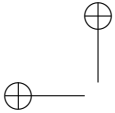


Contents

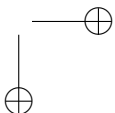
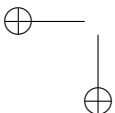
Preface	v
Contents	xii
Summary	xiii
Samenvatting	xvii
List of Abbreviations	xxi
List of Symbols	xxiii
1 Introduction to the Axial Flux PM Machine	1
1.1 Introduction	1
1.1.1 Features of the axial flux PM synchronous machine	1
1.1.2 Basic Axial Flux PM Machine	2
1.1.3 Topologies	4
1.2 Yokeless And Segmented Armature (YASA) Topology	6
1.2.1 From Torus to YASA	9
1.2.2 Geometry and construction of the YASA machine	10
1.3 Research on the YASA machine	12
1.4 Problem statement	13
1.5 Conclusion	13
2 Field models for lamination eddy currents	15
2.1 Introduction	15
2.2 Eddy currents in laminations	17
2.2.1 Causes of eddy currents in laminations	17
2.2.2 Skin and penetration depths	19
2.2.3 Quantifying inductance and resistance limited eddy currents	20
2.3 Finite-element modelling	22
2.3.1 The challenge of modelling fringing flux in laminations . .	22
2.3.2 Model geometry	23

2.3.3	2D Finite Element model	24
2.3.4	Multilayer 2D finite element model	27
2.3.5	3D finite integration technique model	27
2.3.6	3D finite element method model	28
2.3.7	Mesh generation	29
2.4	Conclusion	30
3	Magnetic material characterisation	31
3.1	Introduction about characteristics and losses of magnetic materials	31
3.1.1	Isotropic materials	31
3.1.2	Anisotropic materials	32
3.1.3	Magnetic measurements with the Epstein Frame	33
3.2	Characteristics of magnetic materials used in this PhD	35
3.2.1	Magnetic characteristics of grain oriented M100-23P	35
3.2.2	Magnetic characteristics of Soft Magnetic Composite	35
3.2.3	Magnetic characteristics of ferromagnetic wire	37
3.3	Loss modelling in magnetic materials	39
3.3.1	Quasi-static loss component	39
3.3.2	Classical loss component: low frequency approximation	41
3.3.3	Classical loss component: 1D diffusion problem	41
3.3.4	Excess loss component	43
3.4	Losses of magnetic materials used in the PhD	44
3.4.1	Losses of grain oriented M100-23P	44
3.4.2	Losses of Soft Magnetic Composite	48
3.4.3	Losses of ferromagnetic wire	49
3.5	Homogenisation methods for eddy-current losses in steel laminations	49
3.5.1	Methods for homogenising the magnetic behaviour	50
3.5.2	Methods for homogenising the electric behaviour	53
3.5.3	Stacking factor of a lamination stack	53
3.6	Equivalent geometry model for laminated media	55
3.7	Post processing of finite element results	55
3.7.1	Lamination stack: individually modelled sheets	56
3.7.2	Lamination stack: homogenisation of the stack	57
3.8	Conclusion	57
4	Fringing flux losses due to the armature reaction	59
4.1	Introduction	59
4.2	Simplified non-rotating experimental setup	60
4.3	Comparison and discussion of different models	60
4.3.1	The models: 2D FEM, 3D FIT, and 3D FEM	60
4.3.2	Validation in the linear case	62
4.3.3	Validation in the non-linear case	64
4.4	Detailed analysis of eddy currents in Laminated Silicon Steel Sheets	66

Contents	xi
4.5 Fringing flux losses as function of flux density	68
4.6 Techniques for reducing fringing flux loss from armature reaction	71
4.6.1 Top & bottom laminations segmented along axial direction	71
4.6.2 SMC tooth tips for capturing fringing flux	72
4.6.3 Ferromagnetic wires as closing path for the fringing flux .	73
4.7 Performance of the three proposed loss reduction techniques . . .	73
4.7.1 Top & bottom laminations segmented along axial direction	74
4.7.2 SMC tooth tips for capturing fringing flux	75
4.7.3 Ferromagnetic wires as a closing path for the fringing flux	76
4.8 Conclusion	78
5 Fringing flux loss in the complete Axial Flux Synchronous Machine	79
5.1 Introduction	79
5.2 The machine under study	82
5.2.1 The considered YASA machine	82
5.2.2 Global design of the machine for high efficiency	83
5.3 Loss analysis in the YASA machine	84
5.3.1 Stator core losses	84
5.3.2 Copper losses	88
5.3.3 Eddy-current losses in the permanent magnets	90
5.3.4 Windage losses and bearing losses	91
5.3.5 Influence of lamination stacking and magnet shapes . . .	92
5.3.6 Summary of the losses in the YASA machine	96
5.4 Construction of the prototype	97
5.4.1 Overview of the prototype construction	97
5.4.2 Construction of the rotors	97
5.4.3 Construction of the modular stator element	99
5.4.4 Casting techniques for the stator	100
5.4.5 Mechanical assembly allowing adjustable airgaps	106
5.4.6 Search coils for fringing flux	107
5.5 Experimental set-up	107
5.5.1 Overview of the complete setup	107
5.5.2 Measurements of torque and total losses	108
5.5.3 Low noise data acquisition of the fringing flux coil signal .	108
5.6 At no-load: fringing flux caused by the permanent magnets	110
5.6.1 Waveforms of flux in the tooth search coil	110
5.6.2 Waveforms of emf in the fringing flux search coil	110
5.6.3 Origin of the dips in the emf waveform	113
5.6.4 Fringing flux losses	116
5.7 At load: fringing flux caused by PM's and stator currents	116
5.7.1 Waveforms of emf in the fringing flux search coil	116
5.7.2 Influence of stator current amplitude on fringing flux . . .	118
5.8 Fringing flux as a function of rotation speed	120



5.9	Fringing flux as a function of airgap width	121
5.10	Conclusion	121
6	Concluding Remarks	125
6.1	Conclusion	125
6.2	Recommendation for future research	126





Summary

Electric motor systems are estimated to account for 46% of global electricity use. Electric motors could be called the workhorses of industry, converting electrical energy to mechanical energy. They drive compressors, rotate pumps, move materials, run fans, blowers, drills or mixers and so on. It is estimated that for industrial applications, motor systems approximately account for 70% of electricity consumption. Small improvements of such huge consumers of electricity, can lead to large energy savings. The share of electrical motors in total energy consumption will even increase, based on today's automobile market. Most stakeholders assume a realistic market share for new electrically chargeable vehicles to be in the range of 2 to 8% by 2020 to 2025. This increase in electrically chargeable vehicles in the near future will decrease the use of fossil-fuel. Because of the growing electricity use due to electrical motors, two European Union legislations has been passed in the EU:

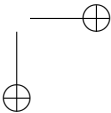
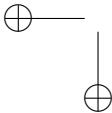
The EU directive 640/2009, which is effective from January 2015 for motors with a rated output from 7.5 to 375 kW and from January 2017 for motors with a rated output from 0.75 to 375 kW, is generally referred as the EU Minimum Performance Standard (MEPS). This directive is expected to result in energy efficiency improvements of 20% to 30%.

Directive 2009/28/EC of 23 April 2009 on renewable energy, discusses energy consumption and the increased use of energy from renewable sources, together with energy savings and increased energy efficiency.

Both legislations ask for higher efficiency and energy savings in electric drives, even in the most demanding conditions.

With respect to the electrical motor technology, the axial flux permanent magnet machine shows many advantages. Axial flux permanent magnet machines are particularly suitable for applications whereby the axial length is limited (built-in applications). They can be applied for a variety of rotational speeds, low speed high torque or high speed low torque, together with a high efficiency and power density.

Although a number of variants on the axial flux permanent magnet topologies exist, this work focuses on the double rotor, single stator topology, which is in literature often referred to as the yokeless and segmented armature or segmented armature torus topology. This topology requires no stator yoke, which increases



the compactness and the power density of the machine. The stator in the yokeless and segmented armature topology is built of individually stator core elements, each provided of aeastooth coil winding. These stator core elements can be manufactured individually and finally arranged together into a stator. This means that the winding process takes place out of the machine, which makes the winding process easy, resulting in a good filling factor of the stator slots. All these advantages of the yokeless and segmented armature topology make it possible to meet the demands on economical manufacturing cost and energy efficiency.

The good energy efficiency is the most important benefit of the axial flux permanent magnet technology in general and particularly of the yokeless and segmented armature topology. Nevertheless, the aim of this work is to further increase the energy efficiency focusing first of all on the existence of specific iron losses in the machine and secondly on the reduction of these specific iron losses.

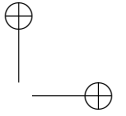
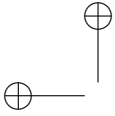
Chapter 1 presents the working principle of axial flux permanent magnet machines, in particular the yokeless and segmented armature topology. It is explained why the yokeless and segmented armature is an interesting topology for further research. A comparison was made with other competing topologies. The global construction of the yokeless and segmented armature topology is explained.

Chapter 2 explains the behaviour of eddy currents in laminations and the influence of several electromagnetic parameters. Skin effect and penetration depth are studied in a stack of laminates. The numerical field models used in this research, together with their model requirements are discussed: 2D Finite Element Method (FEM), 2D multislice technique, 3D Finite Integration Technique (FIT) and 3D FEM.

Chapter 3 starts with a study of the magnetic characteristics of the materials and the losses in these materials: silicon steel (grain oriented and non-oriented), soft magnetic composite (SMC) and ferromagnetic wire. After that, several homogenization techniques are compared in order to model the laminated materials in finite element models.

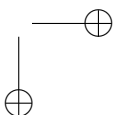
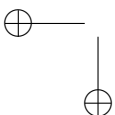
Chapter 4 presents a detailed study of the losses caused by fringing flux coming from the armature reaction on a simplified non-rotating setup, consisting of two tooth coils and a return yoke. The validated field simulations give a very good idea of the cause and the behaviour of fringing flux losses coming from the armature reaction. The last part of this chapter discusses three approaches for reducing these losses. The first method directly restricts the eddy-current losses by segmenting the lamination surface. The second method deflects the fringing flux by using Soft Magnetic Composite (SMC). The third method magnetically short-circuits the fringing flux using ferromagnetic wires. Here the magnetic characterisation from chapter 3 is included in the modelling.

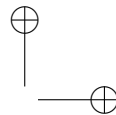
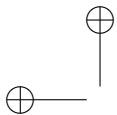
Chapter 5 presents a study of the losses caused by fringing flux coming from the armature reaction and the permanent magnets of the complete axial flux machine. The study is done as a function of several parameters such as rotational speed and air gap size. In addition, in contrast to several cited papers that consider no-load



only, the influence of the stator current is investigated. In the last sections of the chapter, we consider first the no-load situation. Here, the fringing flux losses are caused only by the rotating permanent magnets. Then, full load is considered. At full load, the stator currents cause additional fringing fluxes. Finally, the effect of speed and air gap thickness is explained.

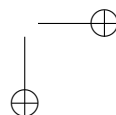
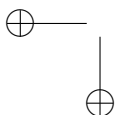
Chapter 6 gives the general conclusion of this research.





xvi

Summary





Samenvatting

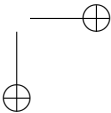
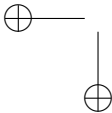
Het aandeel van elektrische motoren en elektrische aandrijvingen wordt geschat op 46% van het wereldwijde elektriciteitsverbruik. Elektrische motoren kunnen de werkpaarden van de industrie worden genoemd. Ze zetten elektrische energie om naar mechanische energie, drijven compressors en pompen aan, zorgen voor de verplaatsing van materialen, drijven ventilatoren, blazers, boren, mixers, ... Voor industriële applicaties staan elektrische motoren naar schatting in voor 70% van het elektriciteitsverbruik. Kleine verbeteringen aan dergelijke grote elektriciteitsverbruikers kunnen aanleiding geven tot grote energiebesparingen. Het aandeel van elektrische motoren in het totale energieverbruik zal zelfs stijgen in de nabije toekomst. Gebaseerd op de visie binnen de hedendaagse automobielsector, verwachten de meeste aandeelhouders een realistisch marktaandeel voor nieuwe elektrisch oplaadbare voertuigen van 2 tot 8% tegen 2020 tot 2025. Deze stijging in de nabije toekomst van elektrisch oplaadbare voertuigen zal het gebruik van fossiele brandstoffen doen dalen. Door het stijgend elektriciteitsverbruik afkomstig van elektrische motoren, heeft de Europese Unie twee wetgevingen opgesteld:

De EU richtlijn 640/2009, die in voege is vanaf januari 2015 voor motoren met een nominaal vermogen van 7,5 tot 375kW en vanaf januari 2017 voor motoren met een nominaal vermogen van 0,75 tot 375 kW, wordt in het algemeen aangeduid als de minimum prestatienorm. Deze maatregel zal naar verwachting leiden tot een stijging van de energie-efficiëntie van 20% tot 30%.

Richtlijn 2009/28/EC van 23 april 2009 inzake hernieuwbare energie, bespreekt het energieverbruik en het toegenomen gebruik van energie uit hernieuwbare bronnen, samen met energiebesparing en grotere energie-efficiëntie.

Beide wetgevingen vragen om een hogere efficiëntie en energiebesparing in elektrische aandrijvingen, zelfs onder de meest veeleisende omstandigheden.

Onder de elektrische motortechnologie, heeft de permanentemagneetbekerachtigde machine met axiale flux veel voordelen. Permanentemagneetbekerachtigde machines met axiale flux zijn bijzonder geschikt voor toepassingen waarbij de axiale lengte beperkt is (ingebouwde toepassingen). Ze kunnen worden ingezet voor verschillende rotatiesnelheden, enerzijds laag toerental en hoog koppel, anderzijds hoog toerental en laag koppel. Dit gaat samen met een hoge efficiëntie en vermogensdichtheid. Hoewel er een aantal varianten van de permanentemagneetbekerachtigde machine met axiale flux bestaan, is dit werk



gericht op de variant met dubbele rotor en enkele stator, die in de literatuur vaak aangeduid wordt als de “Yokeless and Segmented Armature” (YASA) variant. Deze topologie vereist geen statorjuk, waardoor de compactheid en de vermogensdichtheid van de machine verhoogt. De stator in de YASA machine is opgebouwd uit individuele statorkern-elementen, elk voorzien van een geconcentreerde wikkeling. Deze statorkern-elementen kunnen afzonderlijk worden vervaardigd en nadien worden gerangschikt in een stator. Dit betekent dat het wikkelproces buiten de machine plaats vindt. Dit vergemakkelijkt het wikkelproces en maakt het mogelijk een goede vulfactor van de statorgleuven te bereiken. Al deze voordelen van de YASA machine maken het mogelijk om de economische eisen met betrekking tot fabricagekosten en energiebesparingen tegemoet te komen.

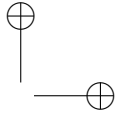
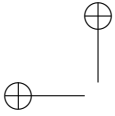
De goede energie efficiëntie is het belangrijkste voordeel van de permanente-magneetbekerachtigde machine met axiale flux in het algemeen en in het bijzonder van de YASA variant. Desalniettemin is het doel van dit onderzoek om de efficiëntie verder te verhogen, door gericht onderzoek te doen naar ten eerste het bestaan van specifieke ijzerverliezen in de machine en ten tweede naar hoe deze specifieke ijzerverliezen kunnen gereduceerd worden.

Hoofdstuk 1 toont het werkingsprincipe van permanentemagneetbekerachtigde machines met axiale flux, met name de YASA variant. Er wordt uitgelegd waarom deze variant de interessantste variant is voor verder onderzoek. Er wordt een vergelijking gemaakt met andere concurrerende topologieën. De globale constructie van de machine wordt uitgelegd.

Hoofdstuk 2 verklaart het gedrag van wervelstromen in lamellen en de invloed van verschillende elektromagnetische parameters. Skin-effect en indringdiepte worden bestudeerd in een stapel lamellen. De numerieke veldmodellen die gebruikt worden in dit onderzoek komen aan bod, alsook de vereisten waar ze moeten aan voldoen: 2D eindige-elementenmethode, 2D multislice techniek, 3D eindige-integratietechniek en 3D eindige-elementenmethode.

Hoofdstuk 3 begint met een onderzoek naar de magnetische eigenschappen van de materialen en de verliezen in deze materialen: gelamelleerd siliciumstaal (georiënteerd en niet-georiënteerd), “soft magnetic composite” (SMC) en ferromagnetische draad. Daarna worden verschillende homogenisatietechnieken vergeleken om het gelamelleerde materiaal in de eindige-elementenmethode te modelleren.

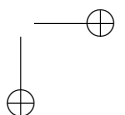
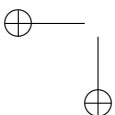
Hoofdstuk 4 presenteert een gedetailleerde studie van de verliezen veroorzaakt door randspreidingsflux, afkomstig van spoelen op een stilstaande vereenvoudigde testopstelling. Deze testopstelling bestaat uit twee tanden voorzien van spoelen en een sluitjuk. Randspreidingsflux of franjes van het veld, wordt in het Engels fringing flux genoemd en veder spreidingsflux genoemd. De gevalideerde simulaties van het magnetisch veld geven een goed beeld van de oorzaken en het gedrag van de spreidingsfluxverliezen afkomstig van de spoelen. Het laatste deel van dit hoofdstuk bespreekt drie methodes voor het verminderen van deze verliezen. De eerste methode beperkt de wervelstromen rechtstreeks door het segmenteren van

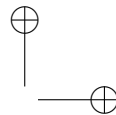
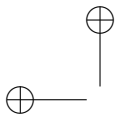


het oppervlak van de lamellen. De tweede methode buigt de spreidingsflux af met behulp van “soft magnetic composite”. De derde methode sluit de spreidingsflux kort door gebruik te maken van ferromagnetische draad. De magnetische karakteristieken van deze materialen uit hoofdstuk drie werden opgenomen bij het modelleren.

Hoofdstuk 5 beschrijft de studie van de verliezen veroorzaakt door spreidingsflux afkomstig van de spoelen en de permanente magneten van de volledige machine. De studie wordt uitgevoerd als een functie van verschillende parameters, zoals rotatiesnelheid en luchtspleet grootte. Bovendien, in tegenstelling tot enkele geciteerde artikels die alleen nullast beschouwen, wordt de invloed van de statorstroom onderzocht. In de laatste delen van het hoofdstuk beschouwen we eerst de onbelaste situatie. Hier worden de verliezen door spreidingsflux alleen veroorzaakt door de roterende permanente magneten. Vervolgens wordt vollast beschouwd. Bij volledige belasting zorgt de statorstroom voor extra spreidingsflux. Tenslotte wordt het effect van de snelheid en de luchtspleetdikte toegelicht.

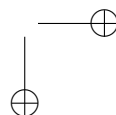
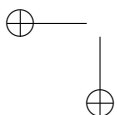
Hoofdstuk 6 geeft de algemene conclusie van dit onderzoek.





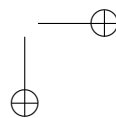
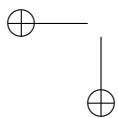
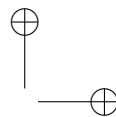
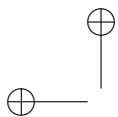
xx

Samenvatting



List of Abbreviations

AC	Alternating Current
AF	Axial Flux
CLS	Conventional Lamination Stacking
CST	Computer Simulation Technology
DoFs	Degrees of Freedom
EMF	Electromotive force
EU	European Union
FEM	Finite Element Method
FE	Finite Element
FIT	Finite Integration Technique
GO	Grain Oriented
IEC	International Electrotechnical Commission
LSSS	Laminated Silicon Steel Sheets
MEPS	Minimum Energy Performance Standard
PM	Permanent Magnet
PMSM	Permanent Magnet Synchronous Machine
PWM	Pulse Width Modulation
SMC	Soft Magnetic Composite
YASA	Yokeless And Segmented Armature
2D	Two dimensional space
3D	Three dimensional space



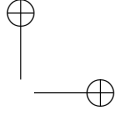
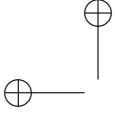
List of Symbols

a_j	Degrees of freedom
A_γ	Magnetic vector potential in γ direction [A/m]
A	Line current density [A/m]
\vec{A}	Magnetic vector potential [Vs/m]
A_{ic}	Surface with applied interface condition [m ²]
A_{2D}	2D cross-section [m ²]
A_p	Incident primary-grid faces to M_ν
$\hat{\mathbf{a}}$	Discretised counterpart of \vec{A}
\vec{B}_{coat}	Magnetic flux density in the coating [Wb/m ²]
\vec{B}_{Fe}	Magnetic flux density in iron [Wb/m ²]
B	Magnetic flux density [Wb/m ²]
B_{peak}	Peak value of the magnetic flux density [Wb/m ²]
B_n	Normal component of \vec{B} [Wb/m ²]
B_{mg}	Maximum value of the flux density in the airgap [Wb/m ²]
b_0	Slot opening [m]
$\hat{\mathbf{b}}$	Discretised counterpart of \vec{B}
\mathbf{C}	Discrete curl operator at the primary grid
$\tilde{\mathbf{C}}$	Discrete curl operator at the dual grid
d	Lamination thickness [m]
D_{av}	Average diameter [m]
D_{ext}	Outer diameter [m]
D_{in}	Inner diameter [m]
E_f	EMF per phase [V]
$e_{fr,meas}$	Measured emf in fringing flux search coil [V]
$e_{fr,sim}$	Simulated emf in fringing flux search coil [V]
η	Energy efficiency
\vec{e}_z	Unit vector in the z -direction
f	Frequency [Hz]
f_{crit}	Critical frequency [Hz]
H	Magnetic field [A/m]
H_α	Main magnetic field in LSSS [A/m]
H_i	Magnetic field intensity at node i [A/m]

H_{boundary}	Magnetic field intensity at the boundary [A/m]
H_{α}	Magnetic field intensity in α direction [A/m]
\vec{H}_s	Coercivity of permanent magnets [A/m]
H_{t1}	Tangential component of \vec{H} [A/m]
H_{middle}	Magnetic field intensity at the middle [A/m]
\hat{h}	Discretised counterpart of \vec{H}
I_{ex}	RMS excitation current [A]
I_a	Armature current [A]
$\underline{\mathbf{J}}$	RMS complex phasor current density [A/m ²]
$\underline{\mathbf{J}}^*$	Complex conjugate of $\underline{\mathbf{J}}$ [A/m ²]
\mathbf{j}_s	Discrete counterpart of \vec{J}_s [A/m ²]
\vec{J}_s	Source current density [A/m ²]
$\hat{\mathbf{j}}$	Discretised counterpart of \vec{J}
$\hat{\mathbf{j}}_s$	Discretised counterpart of \vec{J}_s
$\hat{\mathbf{j}}_{\text{pm}}$	Discretised counterpart of $\nabla \times \vec{H}_s$
$\hat{\mathbf{j}}_e$	Discretised counterpart of \vec{J}_e
\vec{F}_x	Tangential force [N]
J	Current density [A/m ²]
\vec{J}	Current density vector [A/m ²]
$J_{\beta\gamma}, \vec{J}_{\text{res}}$	Resistance limited eddy current density [A/m ²]
$J_{\alpha\beta}, \vec{J}_{\text{ind}}$	Inductance limited eddy current density [A/m ²]
J_{mir}	Virtual current density mirrored with respect to the $\gamma = 0$ plane [A/m ²]
\mathbf{K}_{ν}	Stiffness matrix of reluctivities [m/H]
k_{w1}	The primary winding factor
k_{d1}	The distribution factor
k_{p1}	The pitch factor
l	Length of the conduction path [m]
l_z	Active length [m]
L_i	Armature stack effective length [m]
ℓ_z	Length of the 2D model [m]
\mathbf{M}_{σ}	Matrix of conductivities
M_{sat}	Maximum value of the magnetisation vector \vec{M} [A/m]
M	magnetisation [A/m]
m_1	Number of phases
N_j	First order nodal finite elements (FEs)
\mathbf{n}	Unit vector normal to the interface
n_{mech}	Mechanical speed [RPM]
n_s	Synchronous speed [RPS]
N_1	Number of turns per phase
n_{lam}	Number of laminations
P_{loss}	Joule loss [W]
p_i	Time interval [s]
P_{sim}	Simulated total iron losses [W]
$P_{\text{cl,fr}}$	Eddy-current losses due to fringing flux [W]

P_{meas}	Measured total iron losses [W]
p	Number of pole pairs
P_e	Excess power loss [W/kg]
P_h	Hysteresis power loss [W/kg]
P_{cl}	Classical power loss [W/kg]
\vec{P}_m	The magnetic dipole moments [Am^2]
R	Electrical resistance [Ω]
\vec{r}	Radius vector [m]
S_q	Intersection of laminate q with S_{2D} [m^2]
s	Tangential coordinate
S	Cross-section of the conductor [m^2]
t	Time [s]
\vec{T}	Current vector potential [A/m]
\vec{T}_i	Impressed current vector potential [A/m]
T	Electromagnetic torque [Nm]
t_j	Line integrals of \vec{T} along the edges
V	Volume [m^3]
V_{stack}	Volume of a lamination stack [m^3]
V_{lam}	Volume of laminations [m^3]
W_{em}	Magnetic energy [J]
W_{Fe}	Iron loss density [J/m^3]
W_{hys}	Hysteresis loss density [J/m^3]
W_{dyn}	Dynamical loss density [J/m^3]
W_{cl}	Classical losses density [J/m^3]
W_{exc}	Excess losses density [J/m^3]
w_1	Height of a lamination[m]
w_2	Width of a lamination[m]
α_{Cu}	Temperature coefficient of copper [1/K]
α_i	Average to maximum value of the normal component of \vec{B} in the air gap
δ	Skin depth [m]
δ_{sheet}	Skin depth of individual lamination sheet [m]
$\delta_{\alpha\beta}$	Skin depth of the eddy currents due to perpendicular flux[m]
δ_γ	Penetration depth [m]
δ_{crit}	Critical skin depth [m]
μ	Permeability [H/m]
$\mu_{\text{r,Fe,max}}$	Maximum relative permeability of iron
$\mu_{\text{r,Fe}}$	Relative permeability of iron
μ_{coat}	Permeability of the coating (insulation material) [H/m]
μ_{Fe}	Permeability of Iron [H/m]
μ_γ	Permeability in the out of plane direction of the lamination [H/m]
μ_0	Vacuum permeability [H/m]
$\bar{\mu}$	Permeability tensor

ν	Reluctivity [m/H]
ν_0	Vacuum reluctivity [m/H]
$\vec{\nabla}$	del operator
σ	Electric conductivity [S/m]
σ_{Fe}	Electrical conductivity of iron [S/m]
$\sigma_{\alpha\beta}$	Laminar electric conductivity [S/m]
$\bar{\sigma}$	Conductivity tensor
τ	Pole pitch [m]
χ	Stacking factor
φ	Electric scalar potential [V]
ϕ_j	Nodal values of ϕ
ϕ	Magnetic scalar potential [A]
$\phi_{\text{th,meas}}$	Measured flux through the tooth search coil [Wb]
$\phi_{\text{fr,meas}}$	Measured flux through the fringing flux search coil [Wb]
$\phi_{\text{fr,sim}}$	Simulated flux through the fringing flux search coil [Wb]
ϕ_f	Magnetic flux through one tooth [Wb]
ω	Rotational speed (electric) [rad/s]
Ω_c	Eddy-current problem region
Ω	Whole problem region



Chapter 1

Introduction to the Axial Flux PM Machine

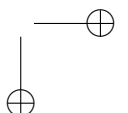
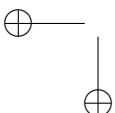
1.1 Introduction

Synchronous machines consist of Permanent Magnet (PM) machines and machines with excitation windings. Three main topologies exist: the radial flux, the axial flux and the transversal flux topology. Assuming a sufficiently large radius, axial flux machines are similar to their radial flux counterpart concerning the electromagnetic aspects. However, the mechanical and thermal design are more complex. Transversal flux machines are very complicated to manufacture because of complex 3D shapes in the stator ferromagnetic path [4]. This work only considers *Axial Flux Permanent Magnet Synchronous Machines* (AFPMSMs).

1.1.1 Features of the axial flux PM synchronous machine

Axial Flux Permanent Magnet Synchronous Machines (AFPMSMs) are mostly selected because of the following main advantages:

- The AFPMSM can be used in all kinds of areas because of the flexible design, whereby the number of PMs together with the diameter of the rotor can be changed easily. By changing the number of PM's on the rotor of the AFPMSM, different rotational speeds together with different torques are obtained. Increasing the diameter and the number of PM's of the rotor makes the machine suitable for low-speed-high-torque applications (electric vehicle propulsion and small/medium ranged direct-drive wind energy systems) [5]. Conversely, decreasing the diameter and the number of PM's of the rotor makes the machine suitable for high-speed-low-torque (pumps, fans, valve control, centrifuges, machine tools, robots and industrial equipment) [6] applications.



- The AFPMSM has a limited axial length, which makes it suitable for built-in applications, like for example in electrical vehicles with in wheel applications. A high power density is reached because of these compact dimensions, which are needed in many applications. The inertia of the large diameter of the rotor can be used as a flywheel.
- The AFPMSM uses permanent magnets for the generation of the magnetic field, and has the same advantages as other types of permanent magnet synchronous machines: no copper losses for magnetization currents and a high efficiency.

Because of these main advantages, AFPMSMs are also used in pumps, fans, valve control, centrifuges, machine tools, robots and industrial equipment.

Besides academic interest, the AFPMSM is also provided by companies like Evo-Electric (UK), Axco-motors (Finland) and YASA Motors Ltd (UK) making custom designed machines.

1.1.2 Basic Axial Flux PM Machine

Construction

The simplest construction of an axial flux machine is schematically shown in figure 1.1. This is a single-sided construction of an axial flux machine and is simpler than the double-sided one, but the torque production is lower. The single-sided construction comprises only one stator and one rotor on which the permanent magnets are placed.

The airgap between the rotating (rotor) and stationary (stator) part has to be as small as possible and is mostly limited by mechanical constraints.

The permanent magnets are magnetised in the axial direction, alternatingly north-south. This causes a magnetic flux, alternatingly magnetized in adjacent stator teeth. In the ideal axial flux machine, the net flux crossing the airgap is zero, which means that the flux in the stator and rotor has to return internally. The magnetic circuit of the single sided axial flux machine is closed by the rotor disk and the stator disk (also called the rotor and the stator yoke). The stator teeth and stator disk of figure 1.1 are one mechanical part.

Operation principle

The operation principle of an axial flux PM machine is equivalent to the one of a radial flux PM machine. The shaft is forced to rotate, either by an external force (e.g. a combustion engine, a wind turbine, a gas turbine, ...) or the machine itself. As the rotor is rotating, the magnetic field from the permanent magnets is rotating. Looking at one stator coil, for every two magnets passing this stator coil, the magnetic field waveform in this stator coil describes one period. If the rotor has for example 16 permanent magnet poles, the magnetic field in a stator coil has eight periods for

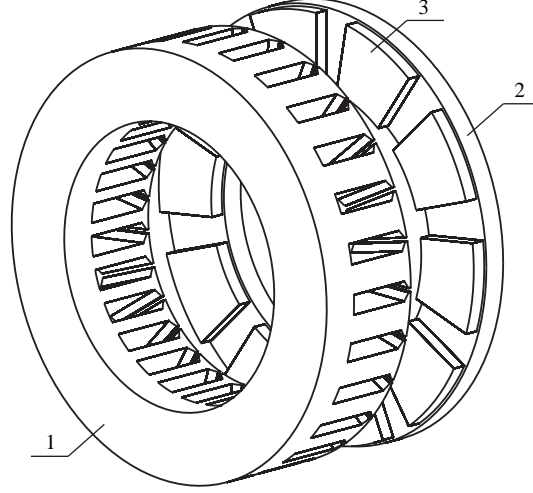


Figure 1.1: Single-sided axial flux permanent magnet machine comprising one stator (1) and one rotor (2) on which the permanent magnets (3) are placed [7].

one mechanical revolution. This time varying magnetic flux induces by Faraday's law a back electromotive force (voltage) in the stator coil. To amplify this induced voltage of one stator coil, several stator coils can be placed in series. The selection of coils to be connected in series can be determined by the star-of-slots theory. The induced voltage (RMS) in the stator phases can be expressed as [8]:

$$E_f = \sqrt{2}\pi n_s p N_1 k_{w1} \phi_f \quad (1.1)$$

with $n_s = \frac{f}{p}$ the synchronous speed of the rotating magnetic field produced by the stator, which equals the mechanical speed in rotations per second, f the electrical frequency in Hz, p the number of pole pairs, N_1 the number of turns per phase, $k_{w1} = k_{d1} k_{p1}$ the primary winding factor which is the product of the distribution factor k_{d1} with the pitch factor k_{p1} , ϕ_f the magnetic flux through one tooth which can be approximated by: $\phi_f \approx \frac{\pi D_{av}}{2p} L_i B_{mg}$ with $D_{av} = \frac{D_{ext} + D_{in}}{2}$ the average diameter, D_{ext} the outer diameter and D_{in} the inner diameter of the lamination stack, $L_i = \frac{D_{ext} - D_{in}}{2}$ the effective length of the stator core in the radial direction and B_{mg} the maximum value of the flux density in the airgap.

The tangential force acting on the rotor disk can be calculated by use of Lorentz law:

$$d\vec{F}_x = I_a (d\vec{r} \times \vec{B}_{mg}) \quad (1.2)$$

where I_a is the armature current, $d\vec{r}$ the radius element, \vec{B}_{mg} the vector of the normal component (perpendicular to the disk surface) of the maximum magnetic

flux density in the airgap at a given radius. Assuming that the magnetic flux density in the airgap B_{mg} is independent of the radius r , this electromagnetic torque is given by [8]

$$dT_d = r dF_x = 2\pi\alpha_i k_{w1} A B_{\text{mg}} r^2 dr \quad (1.3)$$

with $\alpha_i = B_{\text{avg}}/B_{\text{mg}}$ the average to maximum value of the normal component of the magnetic flux density in the airgap and $A = \frac{m_1 N_1 I_a}{p\tau}$ the armature line current density in which m_1 is the number of phases, and τ the pole pitch. Note that the total torque of the machine, found by integrating (1.3) over L_i – scales with the third power of the radius of the machine. For radial flux machines, the scaling law for torque is the square of the radius times the active axial length. Formula 1.3 supposes a non-saturated machine and sinusoidal operation, which are no necessary conditions for axial flux PM machines. In the general case, the torque per square meter and per meter in radial direction can be approximated by:

$$T_{d,sw} = \left(\frac{B_{l,sw} + B_{r,sw}}{2} \right) \mathcal{F}_{m,sw} \quad (1.4)$$

with $B_{l,sw}$ and $B_{r,sw}$, the magnetic flux density, respectively at the left and right side of the slot width and $\mathcal{F}_{m,sw}$ the magneto motive force of the slot width.

When the machine is driven by a mechanical source and connected to an electrical load, power is transferred from the mechanical power on the shaft to electrical power in the load. On the other hand, when the machine is driven by an electrical source and connected to a mechanical load, power is transferred from electrical power to mechanical power on the shaft. The rotor experiences mainly a constant flux over time (flux coming from the permanent magnets) and can for this reason be constructed out of solid steel, because the risk for losses due to induced eddy currents is limited. In contrast, the stator experiences a time varying magnetic field, forming a high risk for losses due to induced eddy currents. In order to limit this risk, laminated silicon steel or Soft Magnetic Composite material (SMC) is used. The mechanical properties of the material and the construction should be chosen in order to withstand the very high axial attraction force between the rotor and stator. Also proper bearings need to be chosen, because the bearings should be able to carry radial as well as axial forces.

1.1.3 Topologies

Besides the single sided construction of the axial flux PM machine, many other topologies are found [9].

First of all there is the single stator double rotor machine (Fig. 1.2), in which the stator is placed between the two rotor discs.

Secondly there is the double stator single rotor topology presented in Fig. 1.3, in which the rotor is placed between the two stators. Possibly, the ferromagnetic part of the rotor can be omitted. Stators with slotted windings and coreless stators

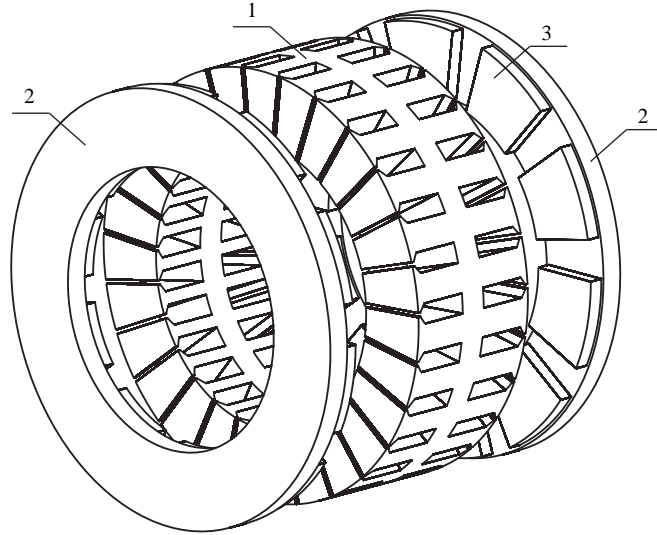


Figure 1.2: Schematic representation of the single stator double rotor axial flux PM machine topology. Stator (1), rotor (2), permanent magnet (3) [7].

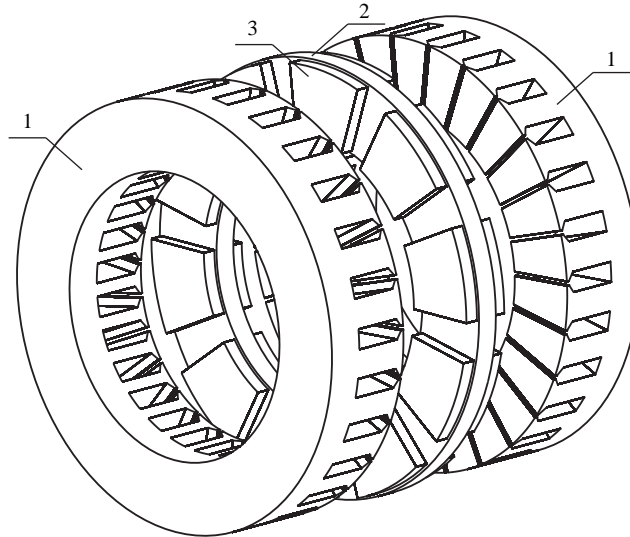


Figure 1.3: Schematic representation of the double stator single rotor axial flux PM machine topology. Stator (1), rotor (2), permanent magnet (3) [7].

are the two main classes in stator construction [10–12].

Stators with slotted windings, whereby the winding is placed in the stator slots, are made of materials with a high magnetic permeability (such as laminated silicon steel or amorphous iron). Unfortunately cogging torque is introduced coming from the stator slot openings near the airgap (local change in permeance). Because of the interaction of the permanent magnets and the stator slot openings, the torque is position dependent. Several applications require a low cogging torque in order to reduce the startup torque. For these applications, coreless (air cored) windings can be used. In axial flux PM machines with coreless windings, the winding is mostly embedded in an epoxy resin having unit permeability. By doing so, the cogging torque together with the core losses vanish and the mass of the machine lowers. The main disadvantage of coreless axial flux PM machines is the high equivalent airgap thickness, which requires a relatively high volume of permanent magnets in order to reach sufficiently high flux densities in the machine. The permanent magnets on the rotor are very often magnets made of rare earth materials such as neodymium (NdFeB) and are therefore costly with respect to silicon steel and copper. The reduction of cogging torque in axial flux slotted PM machines is a topic of recent scientific research.

1.2 Yokeless And Segmented Armature (YASA) Topology

Special attention needs be given to the slotted torus axial flux PM machine with one stator and two rotors. In [13] the north south (NS) torus (Fig. 1.4) and north north (NN) torus (Fig. 1.5) are indicated as the best performing axial flux PM machine topologies.

The torus machine is explained by use of the linear representation of an axial flux PM machine, introduced in Fig. 1.6. A magnetic flux is present in the stator of the NN torus topology because both rotors are magnetised in the opposite direction. This in contrast with the NS torus where the magnets on both rotors are magnetised in equal direction.

The shorter stator yoke in the NS torus topology, increases the power density and lowers the stator core loss in comparison with the NN torus topology. Notwithstanding the winding configuration in the stator slots in the NS torus topology is more complicated compared with the NN torus topology. The latter gives mostly a lower filling factor of the conductors in the stator slots. In the NN torus topology, the winding is toroidally wound around the stator yoke, resulting in an easy winding arrangement, a good filling factor, together with a lower end winding length. In [14] a rectangular conductor is used for the NN torus topology, which results in a high filling factor.

In [14], the efficiency and power density of the NS topology were slightly higher than the NN torus topology.

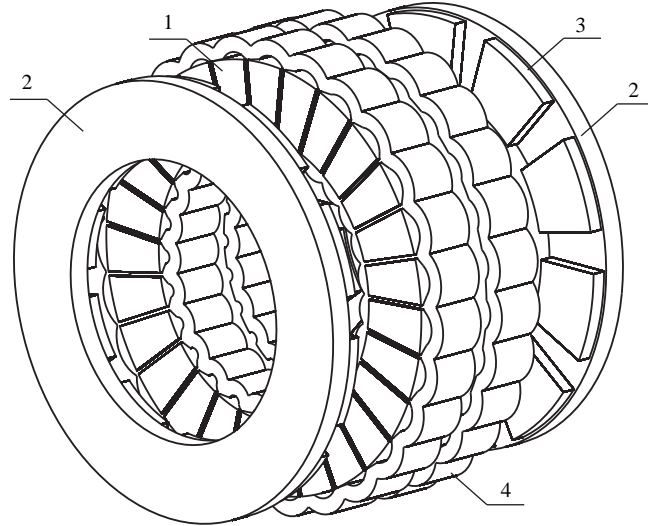


Figure 1.4: Schematic representation of the NS axial flux PM machine topology. Stator (1), rotor (2), permanent magnet (3), winding (4) [7].

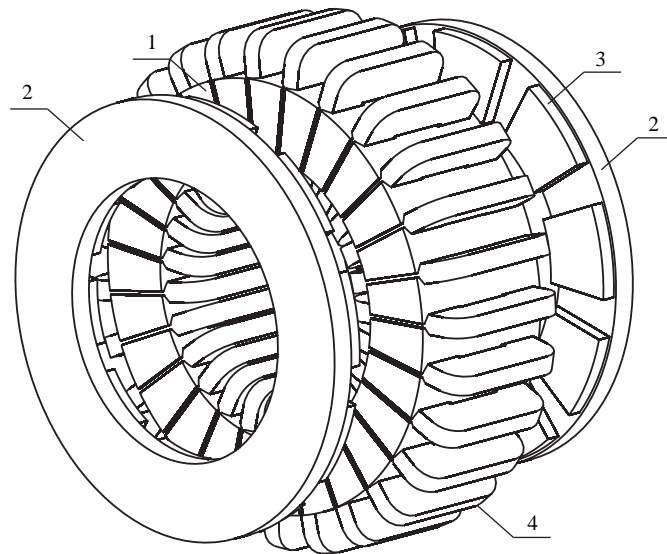


Figure 1.5: Schematic representation of the NN axial flux PM machine topology. Stator (1), rotor (2), permanent magnet (3), winding (4) [7].

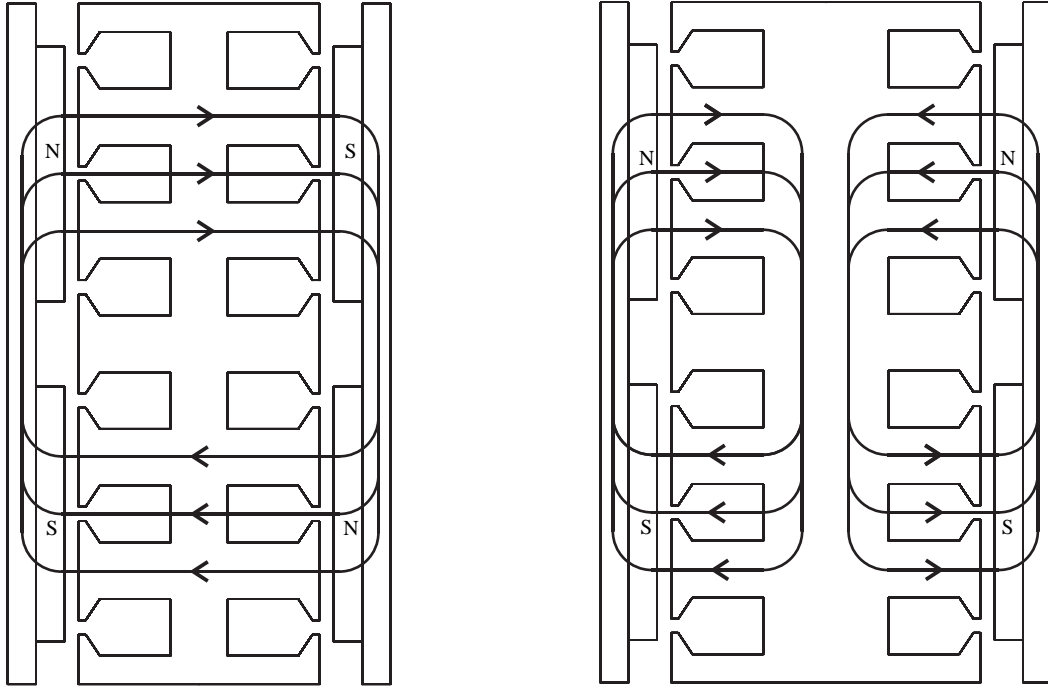


Figure 1.6: Planar versions of the NS (left figure) and NN (right figure) torus machine topologies. The paths of the magnetic flux are indicated [7].

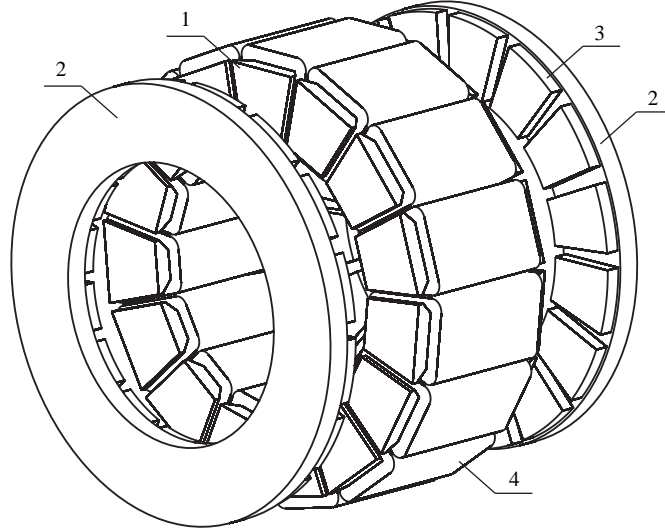


Figure 1.7: The yokeless and segmented armature axial flux machine topology. Stator consisting of multiple stator core elements (1) around which a tooth coil winding (4) is wound, rotor (2), permanent magnet (3).

1.2.1 From Torus to YASA

In [14], the yokeless and segmented armature flux machine topology (Fig. 1.7) is introduced. This machine benefits from a short stator yoke as well as from an easy winding arrangement. Starting from the original NS torus topology, the following adjustments are performed:

- Because of the magnetic symmetry in the machine, there is no magnetic field closing over the stator yoke. This means that the stator yoke has no magnetic function and can be removed entirely. Replacing the stator yoke by individually segmented armature elements, removes the magnetic and mechanical link between the different stator teeth as well.
- By using a concentrated (fractional pitch) winding instead of a distributed winding, it becomes possible to reduce the number of slots per pole and per phase, until the slot pitch approximates the pole pitch.
- The winding arrangement can be improved by using a double layer concentrated fractional pitch winding. A modular construction is obtained, because a winding (also called a tooth coil) is wound around each individually segmented armature (Fig. 1.7), which results in an advanced modular construction.

The yokeless and segmented armature torus machine topology is an excellent energy efficient machine, because of the absence of the stator yoke and stator core loss, the higher power density and the easy winding arrangement.

1.2.2 Geometry and construction of the YASA machine

The active parts of the YASA machine – i.e. the parts that create the magnetic field and torque – are shown in previous figures 1.4-1.7. The stator consists of separate modules: laminated stacks with concentrated windings around it. These are mechanically connected by an epoxy resin and an outer aluminium ring structure, also taking care of the cooling. The rotors are solid discs in steel with magnets glued on it. It is clear that the YASA machine is a challenge, not only on electromagnetic but also on the thermal and mechanical domain. The mechanical and thermal challenge in building such a machine is in making sure that the high axial forces between stator and rotor do not cause deformation in the machine, or that thermal gradients do not cause damage. To give a better overview on such a stator module, an exploded view is presented in Fig. 1.8.

Among the different constructed YASA-prototype machines in recent literature, three variants are found. In [15], two endshields at both sides of the stator keep the different elements together. These endshields are made of high-strength synthetic material, as electrically conductive or magnetically permeable materials would deteriorate the electromagnetic properties of the machine. A drawback of this method is the increase of the airgaps.

A second solution is proposed in [16] where 2 holes are made into the core elements near the core tips (one at each side). The mechanical fixation is provided by bolts, connecting the individual elements with an inner stator structure. Disadvantages are found in the induced eddy currents in the electrically conductive material of the bolts and a major influence on the flux density pattern and possible local saturation in the core elements near the stator tips.

A third construction method is introduced in [17], where the shafts of the individual stator core elements are inserted into two slotted supporting structures near the tooth tips. The axial movement is prevented by internal clamping of the tooth tips between the two slotted supporting structures. This has the major disadvantage that the slot area near the tooth tips remains unwound, which increases the leakage flux. Moreover, there is the risk of induced eddy currents in the electrically conductive slotted supporting structures as they are situated very close to the airgap.

In this PhD, another mechanical construction is proposed, taking care of accurate positioning and rigid fixation of the modular stator teeth by use of an epoxy resin. The stator housing consists of an aluminium ring with radially inward fins. The fins reach between adjacent stator teeth modules. In this solution, the heat evacuation from the windings and the iron towards housing is optimized. The main function of the aluminium ring is to evacuate the heat produced by the windings

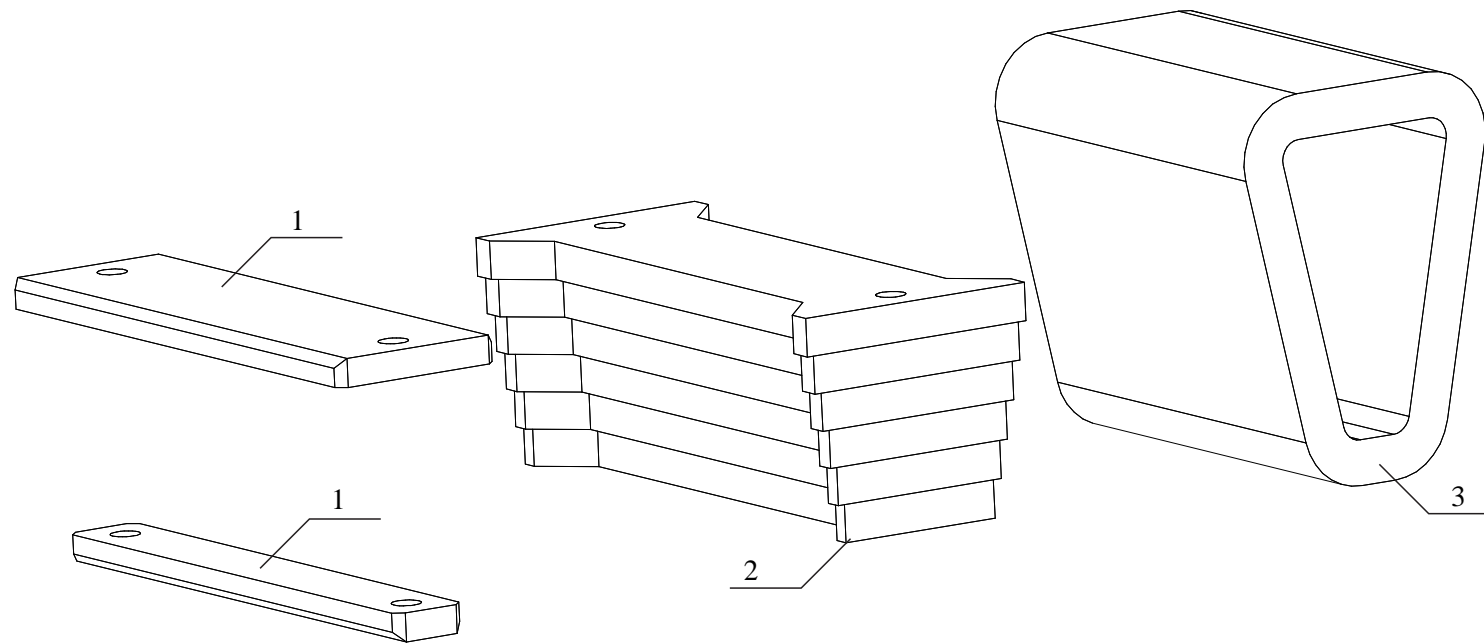


Figure 1.8: Exploded view of a preassembled stator core element. Mechanical bracket (1), stator core element (2), tooth coil winding (3).

to the outside of the machine (cooling of the machine). The main function of the epoxy is increasing the strength of the stator. The details about the construction are given in Chapter 5.

1.3 Research on the YASA machine

Although the yokeless and segmented armature torus machine has inherently a high efficiency and power density, these quantities can be further improved.

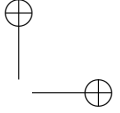
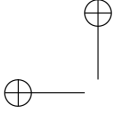
In the PhD of Dr. H. Vansompel [7] of Ghent University, several aspects of the machine have been studied and improved. First of all, the magnetic materials were studied. Grain oriented magnetic material was used instead of conventional non-oriented material. The influence of eddy currents in the magnets was a second research topic. By segmenting the magnets, these losses could be significantly reduced. Thirdly, the winding layout was investigated, proving that the Electro Motive Force (EMF) could be increased by a few percent by using a combined star-delta winding layout [18]. Finally, the effect of several geometry parameters was investigated: the slot openings, the shape of the magnets and the shape of the stator teeth. As the results of the PhD are also relevant for the work about fringing flux losses, a summary of some of the results of dr. Vansompel is given in Chapter 5.

A new YASA AFPMSM was presented in the work of Dr. Woolmer of the University of Oxford [14]. This new YASA AFPMSM is having a higher torque density than other axial flux machines, typically by 20%. This is due to the absence of the stator yoke, which gives a reduction of 50% of iron. Finite Element (FE) analysis has been used to accurately calculate the machine losses. The machine was shown to have a peak efficiency of 96% and a wide range of operating conditions, where the efficiency was above the 94%.

In [19] a 1.6kW AFPMSM generator was designed to operate in small-scale wind power applications. The obtained phase voltage and current were pure sinusoidal and the torque ripple was low. The mechanical structure of the proposed machine was simplest and cheaper than other axial flux machine configurations with laminated stator cores.

A new segmented armature torus AFPMSM as a strong candidate for in-wheel direct drive motors was presented in [16]. The key feature of the motor is the new configuration for the laminated stator cores of an axial flux machine, resulting in low manufacturer cost while maintaining power and torque densities similar to that of the mainstream radial flux machines, which are less suitable for an in-wheel configuration.

An experimental study is done on reducing the cogging torque and the no-load losses in axial flux permanent magnet machines with slotted windings in [20]. It was seen that magnetic wedges used for closing the slot openings were likely to be used for reducing the cogging torque and no-load losses of the machine. Also skewing of the permanent magnets and the selection of an appropriate magnet



width is important in order to reduce the cogging torque. Shortening the magnet pitch was found to be the most effective measure for reducing the cogging torque to a few percent of the machine rated torque.

Antisymmetry effects in AFPMSMs were studied in [21]. A quasi-analytical method for the evaluation of the airgap field in an axial flux PM machine has been developed. Based on this method, several operation quantities are obtained, such as flux linkages, EMFs, parallel loop circulating currents among winding parallel paths, axial forces and bending torques, all taking into account dissymmetry manufacturing defects.

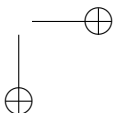
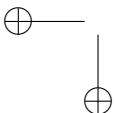
In [22] a comparison is made between Soft Magnetic (SMC) AFPMSM stator cores. Two machines with fractional slot windings, with the same rotor and geometry whose magnetic cores were made of SMC were experimentally compared by use of two machines. The goal of the paper was verifying the degradation of performance of the machine when made of a cheap charged resin core or a commercial SMC. It was found that the iron losses of the charged resin composite were lower than the commercial SMC because of the internal structure of ironcarbonyl. Besides this, it was found that the torque density of the cheaper machine was 60% lower than the machine with commercial SMC stator cores.

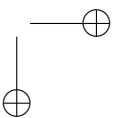
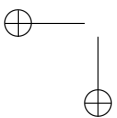
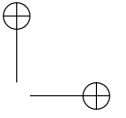
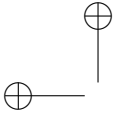
1.4 Problem statement

The state-of-the-art literature did not focus on losses due to fringing flux, nor on special techniques to reduce them. Also mechanical construction, thermal behaviour and production issues are less elaborated in literature. This PhD has studied these missing parts in literature. The fringing flux losses are in detail examined in the following chapters of this PhD. In addition, the mechanical construction is studied in chapter 5 of this PhD.

1.5 Conclusion

The working principle of axial flux permanent magnet machines was presented, in particular the YASA topology. The reasons to further investigate the YASA topology are its compactness (high power density) and inherently high efficiency. The global construction of the YASA-machine is explained. In further chapters, the construction and production of a prototype is shown, and also detailed studies on the fringing flux losses in this machine. However, before studying the complete machine, a lot of research is done on a simplified, non-rotating setup.





Chapter 2

Field models for lamination eddy currents

2.1 Introduction

The stator of a Yokeless And Segmented Armature (YASA) Axial Flux Permanent Magnet Synchronous Machine (AFPMSM) is built of individual ferromagnetic core elements with concentrated windings. These core elements are often constructed as either solid structure in soft magnetic composite [23] or as a stack of Laminated Silicon Steel Sheets (LSSS), in order to prevent excessive eddy currents. Nevertheless, two types of significant eddy-current effects remain in laminated media when excited by an alternating magnetic field [24].

The first type is due to laminar magnetic fields parallel to the laminations (main field, H_α in figure 2.1). The corresponding eddy currents, which are present in every lamination of the lamination stack ($J_{\beta\gamma}$ in figure 2.1) follow rather long paths in proportion to a rather small enclosed surface area and are called *resistance limited eddy currents* [25]. This means that no skin effect is observed, and that the

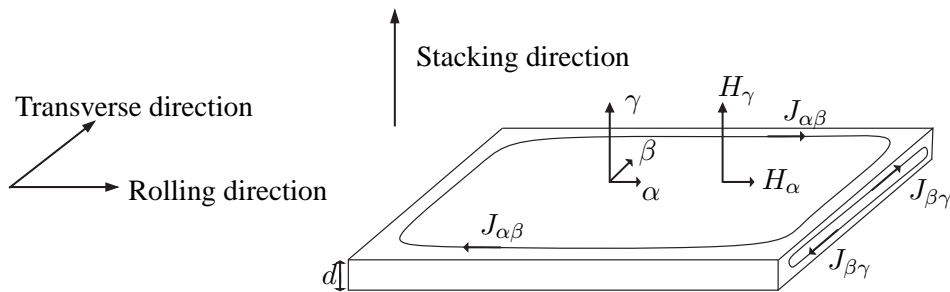


Figure 2.1: Individual lamination sheet; local coordinate system

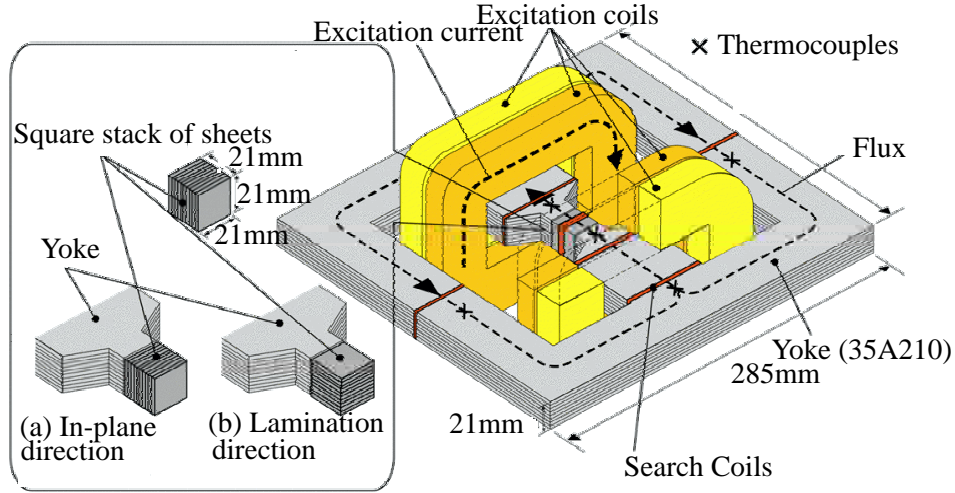


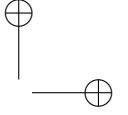
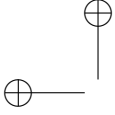
Figure 2.2: Measurement tester for in-plane eddy currents in lamination sheets [26].

currents are too weak to influence the magnetic field that causes them. Of course, these induced currents $J_{\beta\gamma}$ are not guaranteed to be resistance limited, because skin effect will occur in case of high excitation frequency or rather high lamination thickness d . Nevertheless, we use the term *resistance limited eddy currents* for the currents which are mainly restricted by lack of space. In most electric machines, the lamination thickness is sufficiently thin for the given excitation frequency, so that the eddy currents caused by the main flux are indeed of this type.

The second type comes from magnetic fringing fields that are perpendicular to the lamination (fringing fields, H_γ in figure 2.1). The corresponding eddy-current loops parallel to the laminations, which are only present in the end parts of the lamination stack ($J_{\alpha\beta}$ in figure 2.1) follow rather short paths in proportion to the rather large enclosed areas. They thereby experience a large inductance and are called *inductance limited eddy currents*. We use the term *inductance limited eddy currents* for the currents which are mainly restricted by the influence of their own magnetic field [25].

Many authors have investigated the two types of induced currents:

In [26], the second type of eddy currents is measured by use of a tester. The tester, shown in figure 2.2, consists of a square stack of sheets placed in a closed magnetic circuit which is excited by two coils and provided of search coils. First, the square stack of sheets is placed in the in-plane direction (the flux from the excitation winding is perpendicular to the plane of the lamination sheet, (a) in figure 2.2). The total iron losses are measured. Second, the square stack of sheets



is placed in the lamination direction (flux from the excitation winding is parallel to the plane of the lamination sheet, (b) in figure 2.2), and again the total iron losses are measured. The in-plane eddy-current losses are calculated by the subtraction of the first and second measurement. From this analysis, it is found that the eddy currents of the second type have nearly resistance limited characteristics and are penetrating the stack much deeper than the theoretical penetration depth.

In the non-linear case (BH-characteristic as described in section 3.1.1), both eddy current types cannot be strictly separated [27]. They influence each other due to saturation effects, in other words superposition is no longer valid because local saturation causes a local change of permeability which locally changes the skin and penetration depth. In [27] When flux enters the lamination perpendicularly (fringing flux), the surface for the eddy currents is no longer small. This will cause serious eddy-current losses, which will reduce the efficiency of the application. In [28], eddy currents due to perpendicular flux were analysed in an interior permanent magnet motor, by a 3D FEM model, using the parallel computing method on a vector-type parallel supercomputer. Each lamination sheet (with a thickness of 0.5mm) is modelled explicitly by use of gap elements (representing the magnetic resistance between the adjacent sheets) and the perpendicular electrical conductivity of the sheets is set to zero. The eddy-current losses due to perpendicular flux are directly calculated from the eddy current density of the FEM results. The analysed region is 1/12 of the entire region because of symmetry. The analysis, consist of 15 million unknowns, and was completed in 7.3 min/step on 64CPUs of the supercomputer. It is shown that eddy currents related to the perpendicular flux are responsible for an increase of 47% of the total iron losses.

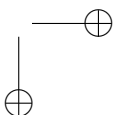
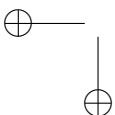
2.2 Eddy currents in laminations

As the magnetic field in the AFPMSM is predominantly in the axial direction, this type of machine is built with laminations in GO (Grain Oriented) silicon steel. In chapter 3, the magnetic behaviour of this material as well as other materials used in this PhD are further explained.

2.2.1 Causes of eddy currents in laminations

In this type of permanent magnet synchronous machines, fringing flux occurs because of three reasons, explained in the next paragraphs:

1. Fringing flux from the excitation coil positioned around the laminated stack (fields closing through the air and entering the lamination perpendicularly, as can be seen in figure 2.8).
2. A part of the flux from the permanent magnets on the rotor, as can be seen in figure 5.27.



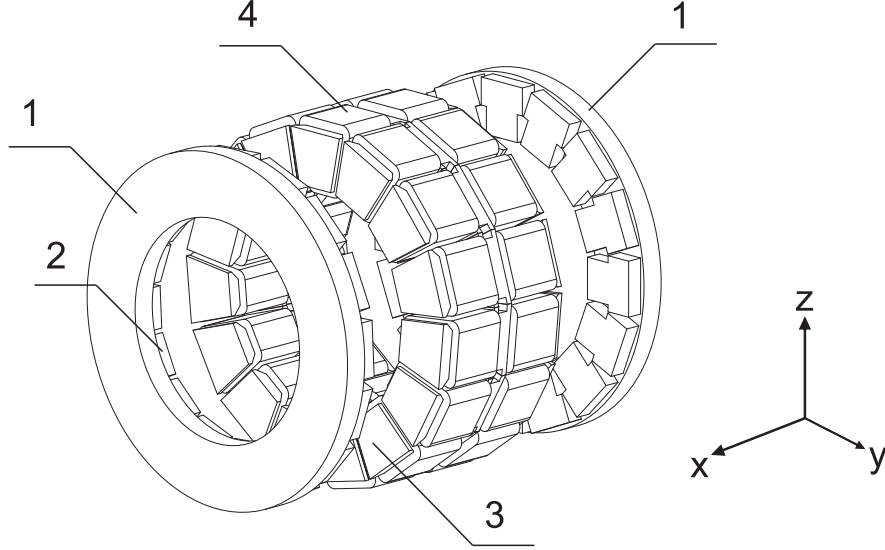


Figure 2.3: Double-rotor, single-stator, yoke-less, and segmented-armature axial flux PM machine. (1) Rotor disk, (2) permanent magnet, (3) laminated stack, and (4) winding [29].

3. Redistribution of magnetic flux due to magnetic saturation of individual sheets, as can be seen in figure 4.12.

The first cause of eddy currents, fringing flux of the excitation coils, can be tackled by increasing the axial length of the coils for a given axial length of the laminations. The eddy-current losses reduce as the coil is stretched over a longer axial portion of the lamination sheets, at most if they are as long as the lamination stack itself. The latter means that the windings reach the airgap. Then there is no space left for additional tooth tips at the end of the stacks. The lack of tooth tips increases the higher harmonic content of the airgap field. This may lead to a higher cogging torque [30] and unacceptably large eddy currents in the iron and the permanent magnets at the rotor side. Moreover the proximity effect between neighbouring conductors will become dominant in a coil with a longer axial length [7]. Evidently, it is also possible to reduce the axial length of both laminations and windings, leading to a lower inductance and by consequence higher peak torque of the electrical machine. A quantitative overview of the influence of several geometric parameters on the individual loss terms and performance of the machine is done in chapter 5.

The second cause is related to flux of the permanent magnets on the rotor. The axial component of this flux is parallel to the laminations. This component is responsible for the torque generation, but also leads to eddy currents ($J_{\beta\gamma}$ in

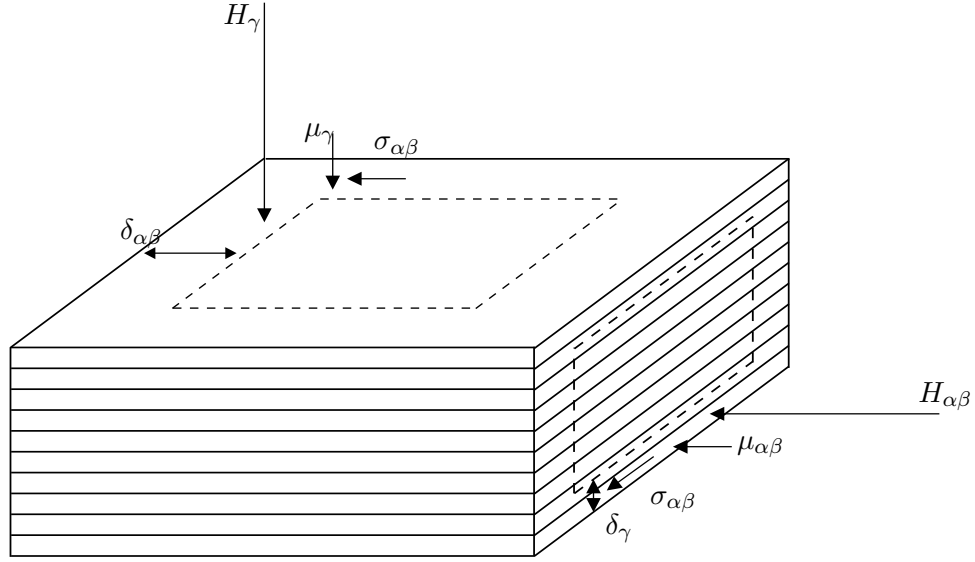


Figure 2.4: Skin depths for longitudinal and perpendicular magnetic flux components.

figure 2.1). The radial component of the permanent magnet flux (fringing flux in the airgap) is perpendicular to the laminations, which will lead to eddy currents $J_{\alpha\beta}$ in the $\alpha\beta$ -plane in figure 2.1).

The third cause is related to magnetic saturation. Magnetic saturation causes migration of magnetic flux between the individual lamination sheets. This comes together with perpendicular field components that also generate eddy currents. This phenomenon is also encountered in transformer lamination stacks [31]. The third effect will result in flux travelling from one sheet to another, causing flux perpendicular to the plane of the sheet. The flux will follow a path as in transformer cores, where sheets overlap each other in order to have a parallel way with low reluctance (not only the airgap, but also a way between adjacent sheets).

2.2.2 Skin and penetration depths

A local coordinate system (α, β, γ) is attached to a lamination sheet, as shown in figure 2.1. The coordinates α and β are aligned with the lamination sheet whereas γ is perpendicular to the sheet. The skin depth is

$$\delta_{\text{sheet}} = \sqrt{\frac{2}{\omega \mu_{\text{Fe}} \sigma_{\text{Fe}}}} \quad (2.1)$$

with $\omega = 2\pi f$ the angular frequency, f the frequency and μ_{Fe} and σ_{Fe} the permeability and conductivity of the silicon steel. This formula for the skin depth is derived from the half-plane model [25, 32] and is only valid as long as a homogeneous magnetic flux density is exerted on the lamination sheet.

It makes sense to think about the lamination stack as a solid block of material with homogenised material parameters [24] as described in section 3.5. The skin depths of the homogenised lamination stack are

$$\delta_{\alpha\beta} = \sqrt{\frac{2}{\omega\sigma_{\alpha\beta}\mu_{\gamma}}} \quad (2.2)$$

$$\delta_{\gamma} = \sqrt{\frac{2}{\omega\sigma_{\alpha\beta}\mu_{\alpha\beta}}} \quad (2.3)$$

Here, $\delta_{\alpha\beta}$ is the skin depth of the eddy currents due to the magnetic flux component perpendicular to the laminates. These eddy currents hamper the penetration of the perpendicular magnetic flux component into the lamination stack. This phenomenon can be characterised by the penetration depth δ_{γ} experienced by the magnetic flux components along the laminates (figure 2.4). Because μ_{γ} is considerably smaller (series connection of the highly permeable lamination part and the coating) than $\mu_{\alpha\beta}$, the skin depth $\delta_{\alpha\beta}$ related to the perpendicular flux is much larger than the penetration depth δ_{γ} corresponding to the main (longitudinal) flux components. The eddy-current paths according to δ_{γ} are, however, restricted by the small lamination thickness. On the contrary, the eddy-current paths according to $\delta_{\alpha\beta}$ and the perpendicular flux component spread out along the lamination and may cause significant eddy-current effects, especially for laminations with a large surface.

2.2.3 Quantifying inductance and resistance limited eddy currents

By exploiting symmetry

We again consider figure 2.1 with a local coordinate system (α, β, γ) attached to a lamination sheet. In figure 2.1, as already explained, resistance limited eddy currents caused by the main flux mainly in α -direction flow in $\beta\gamma$ -planes, and are denoted by $J_{\beta\gamma}$, whereas inductance limited eddy currents caused by fringing flux are denoted by $J_{\alpha\beta}$ and mainly flow in $\alpha\beta$ -planes.

Figure 2.5 shows the cross-section of figure 2.1. In order to get more insight in the behaviour of resistance limited and inductance limited currents, the total current density vector \vec{J} is written as a sum of two contributions: $\vec{J} = \vec{J}_{\text{ind}} + \vec{J}_{\text{res}}$. In the cross-section of figure 2.5, the inductance limited eddy currents \vec{J}_{ind} flow in β direction and have the same sense at the top and bottom of the sheets. This is in contrast with the resistance limited eddy currents \vec{J}_{res} , which also flow in the β -direction but have an opposite sense at the top and bottom of the sheets.

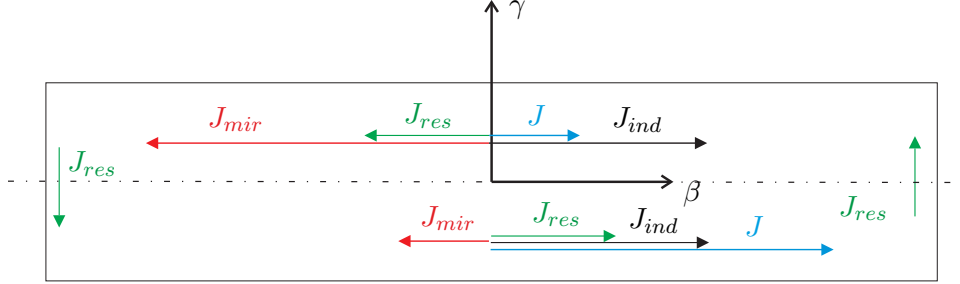


Figure 2.5: Cross-section of the individual lamination of figure 2.1, indicating the separation of resistance limited and inductance limited eddy currents.

We assume that the amplitude of \vec{J}_{ind} is constant in γ -direction, i.e. along the (small) thickness of the thin lamination sheet. This means that the fringing flux is homogeneous along the thickness of the lamination sheet. Although not exactly true – see the finite element results in chapter 4 – this assumption is useful for the splitting of the two loss contributions and for understanding the different loss mechanisms. The $\gamma = 0$ plane – the dash-dot line in the figure – is taken as a symmetry plane. It can be seen that both eddy current types counteract each other above the $\gamma = 0$ plane and reinforce each other below the $\gamma = 0$ plane. This makes it possible to separate and quantify both types of eddy currents by use of the following mirrored current densities with respect to this plane:

$$\vec{J}(\alpha, \beta, \gamma) = (J_\alpha(\alpha, \beta, \gamma), J_\beta(\alpha, \beta, \gamma), J_\gamma(\alpha, \beta, \gamma)) \quad (2.4)$$

$$\vec{J}_{\text{mir}}(\alpha, \beta, \gamma) = (-J_\alpha(\alpha, \beta, -\gamma), -J_\beta(\alpha, \beta, -\gamma), J_\gamma(\alpha, \beta, -\gamma)) \quad (2.5)$$

With \vec{J} the local current density and \vec{J}_{mir} a virtual current density mirrored with respect to the $\gamma = 0$ plane. To ensure the continuity law to hold for \vec{J}_{mir} as well, there is no minus sign for the mirrored γ component. Using this mirrored current density, both eddy current types can be distinguished:

$$\vec{J}_{\text{ind}} = \frac{\vec{J} - \vec{J}_{\text{mir}}}{2} \quad (2.6)$$

$$\vec{J}_{\text{res}} = \frac{\vec{J} + \vec{J}_{\text{mir}}}{2} \quad (2.7)$$

\vec{J}_{ind} and \vec{J}_{res} flow in the same and opposite senses respectively at the top and bottom of the sheet, as can be seen in figure 2.1. The following properties hold,

with V the volume of the sheet:

$$\vec{J}_{\text{res}} \cdot \vec{J}_{\text{ind}} \neq 0 \text{ for } \alpha, \beta, \gamma > 0 \quad (2.8)$$

$$\int_V \vec{J}_{\text{res}} \cdot \vec{J}_{\text{ind}} dV = 0 \quad (2.9)$$

$$\int_V \frac{\vec{J} \cdot \vec{J}}{\sigma} dV = \int_V \frac{(\vec{J}_{\text{res}} + \vec{J}_{\text{ind}}) \cdot (\vec{J}_{\text{res}} + \vec{J}_{\text{ind}})}{\sigma} dV \quad (2.10)$$

$$= P_{\text{res}} + P_{\text{ind}} \quad (2.11)$$

The last property (2.11) indicates that the power losses due to fringing flux and due to main flux can be separated. In other words, that superposition can be done. This allows to clearly distinguish between losses due to the main flux and losses due to the fringing flux. As already mentioned, the above quantification is only valid for a homogeneous flux distribution over the cross-section of the lamination. In [27] it was stated that in the non-linear case, both eddy current types cannot be strictly separated. However, this property (2.11) is valid in the linear and non-linear case, because the magnetic state is determined first on the basis of the total eddy current.

By subtracting classical eddy-current losses from total eddy-current losses

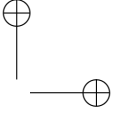
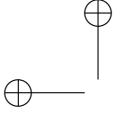
The previous separation technique of both eddy current types is only valid for a homogeneous flux distribution over the cross-section of the lamination. A separation which is valid for a non homogeneous flux distribution over the cross-section of the lamination exists by calculating the eddy-current losses due to both eddy current types in FEM and subtracting the losses due to the resistance limited eddy currents. The latter are calculated by use of the low frequency approximation of Bertotti or at high frequencies by use of the 1D diffusion model as described in 3.3.2. In later chapters, this method is used for calculating fringing flux losses.

2.3 Finite-element modelling

2.3.1 The challenge of modelling fringing flux in laminations

This work focuses on all three causes of fringing flux described in paragraph 2.2. In order to attain a sufficient modelling accuracy, all details of the laminated media are taken into account. In [33], analytical expressions are given for the eddy-current losses for low and very high frequencies in a rectangular geometry. An analytical approach would require too many simplifications and would become too difficult for the geometry under consideration. For this reason, a finite-element (FE) model is constructed. Considering the individual laminations and insulation layers explicitly is a challenge for the numerical model for three reasons:

1. The geometric scaling problem.



2. A high number of unknowns.
3. Limited computational accuracy.

The first reason is related to the large geometrical disproportion between the lamination and insulation thicknesses and the device size. The meshes of the laminations must be finely divided along the perpendicular direction of the sheets [28]. Creating a mesh for the insulation layers is challenging because of mesh growth problems.

The second reason relates to the maximal mesh size, which is limited for taking into account the skin effect. For this reason, the mesh size must be sufficiently smaller than the skin depth in each individual lamination.

The third reason relates to eddy currents due to stray fields being a secondary effect and are for this reason small compared to the excitation currents. As a consequence, the solution for the eddy currents may be inaccurate, even when the magnetic field converged [34], [35].

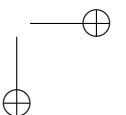
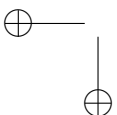
The corresponding large memory consumption and calculation times hamper the application of such models in many practical situations. For that reason, many papers in literature introduce homogenization techniques [36] and embedded lower dimensional models [37] [27] [38].

The suggested homogenization techniques fail to accurately describe the eddy-current effect corresponding to perpendicular magnetic flux components, especially in the case when these components originate from non-trivial geometric configurations. This work studies such eddy currents by 2D and 3D field models where all relevant geometrical details, even the thin insulation layers, are explicitly modelled. The calculation results are compared to each other and to the measurement results obtained from a dedicated experimental setup. Eddy currents due to perpendicular flux will hamper the flux causing these eddy currents by Lenz's law. This shielding effect for the perpendicular flux is not perfectly taken into account by any homogenization technique. In 2D, it is possible to implement all details of the insulated media for a simple geometry. In 3D, it is almost impossible.

Therefore, this work will first show a 2D pseudo anisotropic linear FEM model including all details of the laminated media. Secondly a 3D pseudo anisotropic linear FEM model is presented, where a combination of individual sheets and a homogenized bulk area is adopted. After this a comparison of the 2D and 3D model is made. Finally a 3D pseudo anisotropic non-linear model is presented, for the simple non-rotating geometry that will be presented in chapter 4.

2.3.2 Model geometry

The considered geometry – a non-rotating, simplified geometry of an axial flux PMSM – consists of a lamination stack, a coil carrying a magnetising current, an airgap and a yoke closing the magnetic circuit (Figure 2.6). Symmetries allow to only model one fourth of the geometry in 2D and one eighth of the geometry in 3D,



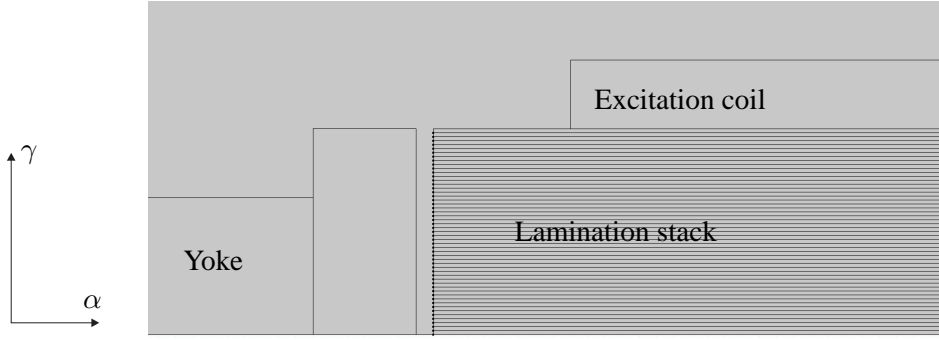


Figure 2.6: A section of a laminated stack in the XZ-plane is taken from the axial flux permanent magnet synchronous motor of figure 2.3. On the left side a yoke is provided as a conducting path for the magnetic flux. The insulation layers between adjacent sheets are modelled explicitly.

accompanied by appropriate boundary conditions. In contrast to many approaches where the lamination stack is considered as a bulk material with homogenised material parameters, here, the individual lamination sheets are considered. Furthermore, the thin insulating coating between the sheets is either modelled explicitly or embedded in the model by thin low-permeability interface conditions.

2.3.3 2D Finite Element model

The magnetic flux density $\vec{B} = \vec{\nabla} \times \vec{A}$ is expressed in terms of the magnetic vector potential \vec{A} . By the Faraday-Lenz law, the electric field strength is $\vec{E} = -\frac{\partial \vec{A}}{\partial t} - \vec{\nabla} \varphi$ with φ the electric scalar potential. In the frequency domain, Ampère's law, $\vec{\nabla} \times \vec{H} = \vec{J}$ with \vec{H} the magnetic field strength and \vec{J} the electric current density, leads to

$$\vec{\nabla} \times (\nu \vec{\nabla} \times \vec{A}) + j\omega \sigma \vec{A} = \vec{J}_s - \vec{\nabla} \times \vec{H}_s, \quad (2.12)$$

with $\nu = 1/\mu$ the reluctivity, μ the permeability, σ the conductivity, $\omega = 2\pi f$ and f the (angular) frequency, $\vec{J}_s = -\sigma \vec{\nabla} \varphi$ the source current density and \vec{H}_s the coercivity of the permanent magnets. In case of anisotropic material behaviour, ν and σ need to be replaced by the tensors $\bar{\nu}$ and $\bar{\sigma}$ respectively. The magnetic vector potential is discretised by first order edge elements

$$\vec{w}_j(x, y, z) = \frac{N_j(x, y)}{\ell_z} \vec{e}_z \quad (2.13)$$

where $N_j(x, y)$ are standard first order nodal finite elements (FEs), ℓ_z is the length of the 2D model and \vec{e}_z is a unit vector in the z -direction [39]. The magnetic vector potential reads:

$$\vec{A} = \sum_j a_j \vec{w}_j \quad (2.14)$$

where a_j are the degrees of freedom (DoFs). The discrete counterpart of (2.12) reads

$$\mathbf{K}_\nu \mathbf{a} + j\omega \mathbf{M}_\sigma \mathbf{a} = \mathbf{j}_s + \mathbf{j}_{\text{mg}} \quad (2.15)$$

where \mathbf{K}_ν is the stiffness matrix of reluctivities, \mathbf{M}_σ the matrix of conductivities, \mathbf{j}_s the discrete counterpart of \vec{J}_s and \mathbf{j}_{mg} the discrete counterpart of $\vec{\nabla} \times \vec{H}_s$, which all follow from the discretization procedure and where \mathbf{a} gathers the DoFs.

The magnetic fluxes are aligned with the considered 2D cross-section A_{2D} , whereas the excitation current and the eddy currents are perpendicular to A_{2D} . All lamination sheets are considered explicitly. However, the insulation layers are only present as line segments in the geometry and the mesh. Their relatively high reluctances are modelled by the thin low-permeability interface condition, as described in the next paragraph. The current through each individual laminate (perpendicular to the 2D cross-section) should be zero. This is enforced in the model by an integral constraint of the form

$$\int_{S_q} \vec{J} \cdot d\vec{S} = 0 \quad (2.16)$$

where S_q is the intersection of laminate q with S_{2D} . Such integral constraint possibility is offered by the COMSOL Multiphysics® software.

Thin low-permeability interface condition

Considering individual lamination sheets already leads to huge numbers of DoFs in the field models. When, moreover, the insulation layers between them need to be drawn and meshed, the model may become prohibitively large. A way around is offered by a thin low-permeability model [40, 41]. The thickness of the insulation layer is not resolved by the computational grid but is present in the grid as a surface A_{ic} at which a specific interface condition is applied.

The application of Ampère's law to the rectangle with infinitesimal cross-section in Figure 2.7 relates the tangential components H_{t1} and H_{t2} of the magnetic field strength at both sides of the insulation layer to the normal component of the magnetic flux density B_n by

$$H_{t1} - H_{t2} = \nu_0 h \frac{\partial B_n}{\partial s} \quad (2.17)$$

where ν_0 is the reluctivity of the insulation layer, h is the insulation thickness and s is a tangential coordinate. In general,

$$\vec{n} \times (\vec{H}_1 - \vec{H}_2) = \vec{\nabla}_t \times (\nu_0 h \vec{\nabla}_t \times \vec{A}) \quad (2.18)$$

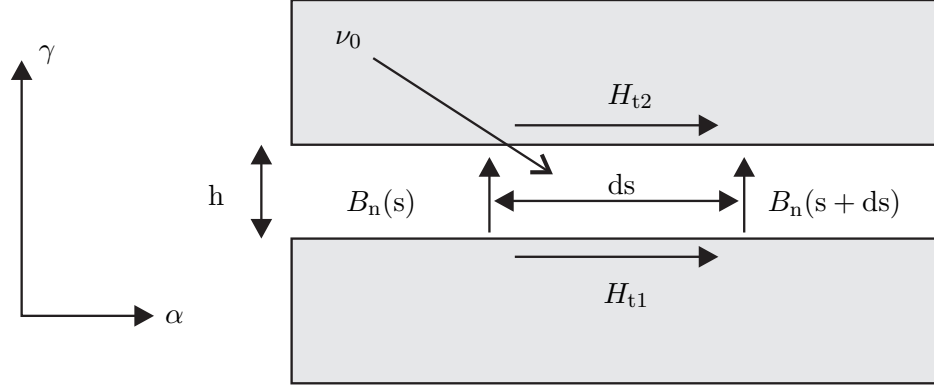


Figure 2.7: Ampère path around a thin insulating layer relating the tangential components H_{t1} and H_{t2} of the magnetic field strength to the normal component B_n of the magnetic flux density.

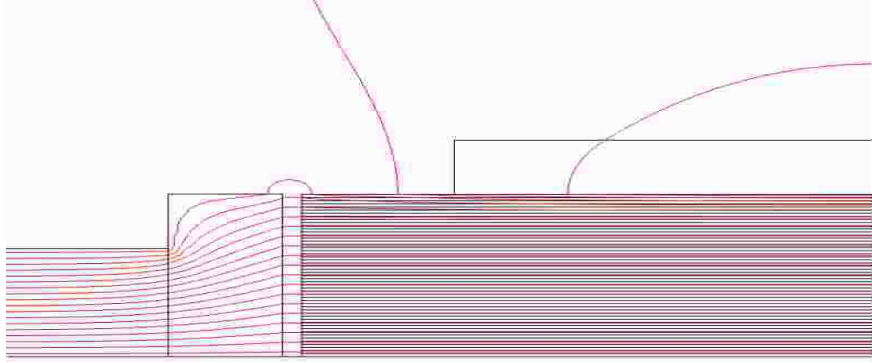


Figure 2.8: Contour of the magnetic vector potential, for an airgap of 1mm, computed by the 2D FEM with “thin permeability gap” boundary condition between adjacent laminations.

Where \mathbf{n} is the unit vector normal to the interface and $\vec{\nabla}_t$ denotes the curl operator at the interface.

The discretisation of (2.18) leads to a term $\mathbf{K}_h \mathbf{a}$ to be added in (2.15). The matrix coefficients are given by

$$\mathbf{K}_{h,ij} = \int_{A_{ic}} \nu_0 h \vec{\nabla}_t \times \mathbf{w}_i \cdot \vec{\nabla}_t \times \mathbf{w}_j dA_{ic} \quad (2.19)$$

Figure 2.8 shows the contour of the magnetic vector potential, for an excitation of 300Aturns at a frequency of 50Hz and an airgap of 1mm. The magnetic material

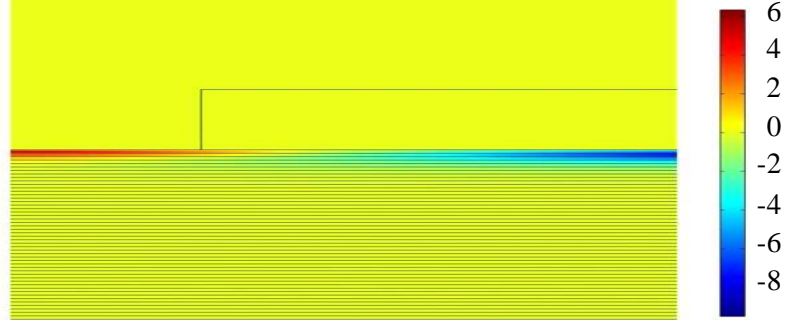


Figure 2.9: Surface plot of the magnitude of the eddy current density ranging from -8×10^4 to 6×10^4 A/m².

is a Grain Oriented (GO) magnetic material, with properties explained in chapter 3. It can be seen that fringing field lines are closing through the air, entering the sheets perpendicularly. The corresponding eddy current density is shown in a surface plot of the magnitude of the induced eddy currents in figure 2.9. It can be seen that the eddy currents due to fringing flux are the largest in the laminations closest to the excitation coil.

2.3.4 Multilayer 2D finite element model

A 2D FE multilayer model consists of several 2D FE models calculated at different radii. In such a 2D FEM, the whole circumference of the machine is modelled for example 15 teeth and 16 magnets. When the magnets are in NS-topology [11], only half of the machine needs to be modelled in axial direction when a Neumann boundary condition is applied at the centre part of the teeth. In circumferential direction, the use of periodic boundary conditions may also reduce the geometry to be modelled, depending on the number of slots and poles of the machine.

2.3.5 3D finite integration technique model

In the Finite Integration Technique (FIT), Maxwell's equations are discretised at a primary-dual hexahedral tensor-product grid, yielding $\widehat{\mathbf{b}} = \mathbf{C}\widehat{\mathbf{a}}$, $\widehat{\mathbf{h}} = \mathbf{M}_\nu\widehat{\mathbf{b}}$, $\widehat{\mathbf{j}} = \mathbf{M}_\sigma\widehat{\mathbf{e}} = -\mathbf{M}_\sigma\mathbf{j}\omega\widehat{\mathbf{a}} + \widehat{\mathbf{j}}_s + \widehat{\mathbf{j}}_{pm}$, $\widetilde{\mathbf{C}}\widehat{\mathbf{h}} = \widehat{\mathbf{j}}$, which gives the discrete counterpart of equation 2.12:

$$\widetilde{\mathbf{C}}\mathbf{M}_\nu\mathbf{C}\widehat{\mathbf{a}} + \mathbf{j}\omega\mathbf{M}_\sigma\widehat{\mathbf{a}} = \widehat{\mathbf{j}}_s + \widehat{\mathbf{j}}_{pm} , \quad (2.20)$$

where $\widehat{\mathbf{a}}$, $\widehat{\mathbf{b}}$, $\widehat{\mathbf{h}}$, $\widehat{\mathbf{j}}$, $\widehat{\mathbf{j}}_s$ and $\widehat{\mathbf{j}}_{pm}$ are vectors collecting the degrees of freedom (DoFs) of \vec{A} , \vec{B} , \vec{H} , \vec{J} , \vec{J}_s and $\vec{\nabla} \times \vec{H}_s$ respectively. \mathbf{C} and $\widetilde{\mathbf{C}}$ are discrete curl operators at

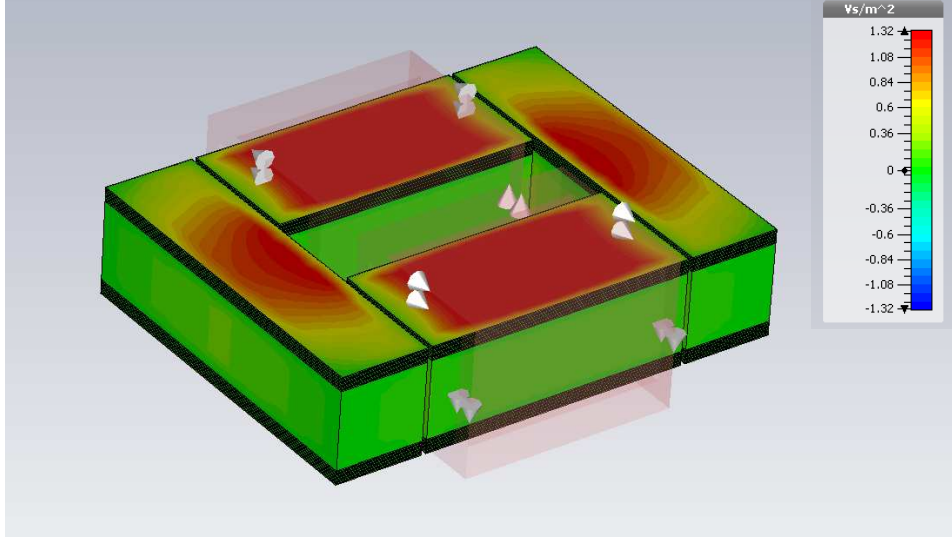


Figure 2.10: Magnetic flux density plot on the surface of the 3D FIT model (with parameters of table 4.1) at a frequency of 50Hz and 200Aturns.

the primary and dual grid pair respectively. \mathbf{M}_ν and \mathbf{M}_σ are the grid reluctance and conductance matrices and represent the constitutive relations $\vec{H} = \nu \vec{B}$ and $\vec{J} = \sigma \vec{E}$ on the computational grid [42]. Also standard finite-element (FE) methods can be expressed in the FIT notation [43]. The Joule loss is post-processed from the field solution $\hat{\mathbf{a}}$ by $P_{\text{loss}} = \omega^2 \hat{\mathbf{a}}^H \mathbf{M}_\sigma \hat{\mathbf{a}}$.

The eddy-current effect is described by the second term in (2.12), which is typically quite small compared to the first term of (2.12). As a consequence, the results for the eddy-current losses may be inaccurate, even when the results for the magnetic field converged [34]. A low solver tolerance may lead to unacceptably large calculation times. In an alternative procedure, $\hat{\mathbf{a}}$ is computed from (2.20) with a feasible tolerance. The accuracy of the eddy currents $\hat{\mathbf{j}}_e = -j\omega \mathbf{M}_\sigma \hat{\mathbf{a}}$ is improved by solving the divergence-correction equation $\tilde{\mathbf{S}} \mathbf{M}_\sigma \tilde{\mathbf{S}}^T \phi = -\tilde{\mathbf{S}} \hat{\mathbf{j}}_e$ and substituting $\hat{\mathbf{j}}_e \leftarrow \hat{\mathbf{j}}_e + \mathbf{M}_\sigma \tilde{\mathbf{S}}^T \phi$, with $\tilde{\mathbf{S}}$ the discrete divergence matrix of the dual facets.

The fringing field lines closing through the air and entering the lamination perpendicularly cause saturation of the first few sheets closest to the excitation coil, this is shown in figure 2.10.

2.3.6 3D finite element method model

The field model is based on a 3D non-linear time dependent magnetoquasistatic field formulation. Second order tetrahedral finite elements are used together with

the $T - \phi$ formulation [44] which uses an additional current vector potential \vec{T} in the eddy current region Ω_c and a reduced magnetic scalar potential ϕ in the whole problem region Ω . The current density \vec{J} , and the magnetic field \vec{H} are calculated from the potentials as:

$$\vec{J} = \vec{\nabla} \times \vec{T}; \vec{H} = \vec{T}_1 + \vec{T} - \vec{\nabla} \phi \text{ in } \Omega_c \quad (2.21)$$

$$\vec{J} = \vec{\nabla} \times \vec{T}_1; \vec{H} = \vec{T}_1 - \vec{\nabla} \phi \text{ in } \Omega - \Omega_c \quad (2.22)$$

with \vec{T}_1 the impressed current vector potential representing the given current density of the coils made of stranded conductors.

In the frequency domain, Faraday-Lenz's law leads to:

$$\vec{\nabla} \times (\rho \vec{\nabla} \times \vec{T}) + j\omega\mu\vec{T} - j\omega\mu\vec{\nabla} \phi = -j\omega\mu\vec{T}_1 \quad (2.23)$$

$$-\vec{\nabla} \cdot (\mu \vec{\nabla} \phi) + \vec{\nabla} \cdot (\mu \vec{T}) = -\vec{\nabla} \cdot (\mu \vec{T}_1) \text{ in } \Omega_c \quad (2.24)$$

$$-\vec{\nabla} \cdot (\mu \vec{\nabla} \phi) = -\vec{\nabla} \cdot (\mu \vec{T}_1) \text{ in } \Omega - \Omega_c \quad (2.25)$$

The current vector potential is approximated by edge basis functions as:

$$\vec{T} = \sum_j t_j \vec{w}_j \quad (2.26)$$

where t_j are the line integrals of \vec{T} along the edges. The magnetic scalar potential is approximated by use of nodal basis functions as:

$$\phi = \sum_j \phi_j \vec{w}_j \quad (2.27)$$

where ϕ_j are the nodal values of ϕ and \vec{w}_j the nodal basis functions.

2.3.7 Mesh generation

The generation of the mesh is a challenge for two reasons. The first reason is that the maximal mesh size must be sufficiently smaller than the skin depth in each individual lamination. The second reason is the large geometrical disproportion between the lamination and insulation thicknesses and the device size. A 3D geometry with thin sheets is particularly challenging for a tetrahedral meshing routine. The standard tetrahedral mesh generator of COMSOL Multiphysics® did not work. Even mesh extrusion techniques resulting in a hexahedral mesh fail because of the large disproportion between the lamination thickness and the device size. The 3D model is constructed and solved in CST EM STUDIO® and post-processed in MATLAB®, both capable of treating 3D hexahedral meshes. In CST, a tensor-product hexahedral mesh easily copes with all geometrical details and is easily constructed. In order to incorporate the large reluctance of the insulation

layers and to prevent current migrating between adjacent laminates, the insulation layers need to be considered explicitly. It is, however, cumbersome to do this for the entire lamination stack. Therefore, only the top and bottom parts of the lamination stack are modelled in full detail (figure 3.25). The number of explicitly modelled lamination sheets is decided upon according to the penetration depth δ_γ . The centre part of the lamination stack is considered as a bulk material with the homogenised material parameters of Eq. (3.25). The tetrahedral mesh generator of Ansys Maxwell® succeeded in generating a mesh of the individual laminations. In order to achieve the optimal level of accuracy, the mesh is first generated in static mode with adaptive mesh refinement. The mesh is refined automatically by use of a highly robust volumetric meshing technique with multithreading capability. The refinement is based on the reported energy error in a static simulation. This adaptively refined mesh is then fixed and further used in the transient solver.

2.4 Conclusion

In this chapter first three causes and the behaviour of eddy currents in laminations is studied and a separation is made between inductance and resistance limited eddy currents. Then, different numerical models were described: 2D FE-model, 3D FIT model and a 3D FE model. The first and third cause of eddy currents in laminations will be studied in chapter 4 on a simplified non-rotating setup. In this chapter, all models will be compared, evaluated and discussed. The second cause of eddy currents in laminations will be studied using the 3D FE model on a complete rotating axial flux machine in chapter 5. The second separation technique will be used for calculating inductance limited eddy currents in the next chapters.



Chapter 3

Magnetic material characterisation

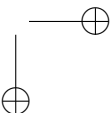
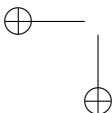
3.1 Introduction about characteristics and losses of magnetic materials

When calculating the magnetic behaviour and iron losses in high energy efficiency machines, like the axial flux permanent magnet machine, accurate modelling of the behaviour and losses of the magnetic material is needed. It is well known that the core losses can be described as a summation of the quasi-static losses, the classical and excess dynamic losses [45, 46], explained further in this chapter. However, these loss components are caused only by the flux in the plane of the laminations. The losses have to be augmented with the loss component due to fringing flux, an extra eddy-current loss caused by flux entering the lamination plane perpendicularly. This loss depends on both the magnetic material behaviour and geometric details. For laminated materials, the thin coatings on the sheets create a big challenge from numerical point of view. Therefore, also homogenisation is studied in order to describe the materials by bulk material having appropriate electromagnetic properties.

In this chapter, we first study the magnetic characteristics of the materials and the losses in these materials. After that, several homogenisation techniques are compared in order to model the laminated materials in finite element models.

3.1.1 Isotropic materials

The flux density vector \vec{B} is written as a function of the magnetic field \vec{H} and the magnetization vector $\vec{M} = \frac{\sum \vec{P}_m}{V}$, with \vec{P}_m the magnetic dipole moments and V the volume:



$$\vec{B} = \mu_0(\vec{H} + \vec{M}) \quad (3.1)$$

with μ_0 the permeability of vacuum. Although the magnetic quantities are vectors, in many cases, the constitutive law can be a scalar characteristic, the BH -characteristic. Moreover, if the hysteretic behaviour is neglected, the materials are characterised by a single-valued BH -curve passing through the origin of the BH -plane. Then, the characteristic can be written using the relative magnetic permeability μ_r : $B = \mu_0\mu_r H$. In this characteristic, three main regions can be distinguished. The first region is for low H and B values and is called the *Rayleigh region*. In the Rayleigh region, the flux density is approximately quadratic with the magnetic field H . The second region is the *linear region*. In this region, the permeability is more or less constant and the flux density is linear with the magnetic field. The last area, the *saturation region* is the region where H is very high. In this region, the magnetisation M becomes constant for $H \rightarrow \infty$ and is equal to the saturation magnetisation (M_{sat}). Here, the differential permeability ($\mu^{\partial} = dB/dH$) is equal to μ_0 .

For non-linear FE calculations with the magnetic vector potential formulation, the reluctivity $\nu = 1/\mu$ needs to be calculated for each element as a function of the magnetic flux density. The BH -curves are measured with an Epstein frame, as shown in paragraph 3.1.3. The measurements provide the measurement points (H_i, B_i) , $i = 0, \dots, n$, with $B_0 = H_0 = 0$. $\nu(B)$ is usually approximated by an analytical formula, or by interpolation of a table of measured values.

3.1.2 Anisotropic materials

For anisotropic materials, the reluctivity tensor $\bar{\bar{\nu}}(\vec{B})$ is used :

$$\begin{bmatrix} H_x \\ H_y \end{bmatrix} = \begin{bmatrix} \nu_{xx} & \nu_{xy} \\ \nu_{yx} & \nu_{yy} \end{bmatrix} \begin{bmatrix} B_x \\ B_y \end{bmatrix} \quad (3.2)$$

The magnetic energy density $w = \frac{1}{2} \vec{B} \cdot \bar{\bar{\nu}} \cdot \vec{B}$ is a quadratic form of \vec{B} [47]. The latter means that $\bar{\bar{\nu}}(\vec{B})$ is a symmetrical positive definite tensor, whereby $\nu_{xy} = \nu_{yx}$. For non-linear materials, the reluctivity components in the tensor are function of the magnetic flux density. Also, $\bar{\bar{\nu}}$ is not uniquely determined because there are two equations and three unknowns (ν_{xx} , ν_{yy} and $\nu_{xy} = \nu_{yx}$) for each known (measured) H and B value. This indeterminacy can also be seen as follows [48]. The tensors $\bar{\bar{\nu}}(\vec{B})$ and $\bar{\bar{\nu}}'(\vec{B})$ are representing the same material if a number $c(\vec{B})$ exists so that:

$$\bar{\bar{\nu}}'(\vec{B}) = \bar{\bar{\nu}}(\vec{B}) + c \begin{bmatrix} B_y^2 & -B_x B_y \\ -B_x B_y & B_x^2 \end{bmatrix} \quad (3.3)$$

However, this uncertainty vanishes by use of the magnetic energy function [7]:

$$W_{\text{em}}(\vec{B}) = \int_0^B \vec{H} \cdot d\vec{B} \quad (3.4)$$

This numerical magnetic energy function $W_{\text{em}}(\vec{B})$ can be constructed by use of single-valued BH -characteristics measured in a finite number of directions with respect to the rolling direction. The single-valued BH -characteristics in each considered direction can be constructed using the peak values of the measured hysteresis loops. As the energy is only calculated in the considered directions with respect to the rolling direction, interpolation is used to get an energy map in an equidistant rectangular grid of points in the (B_x, B_y) -plane. The magnetic field strength \vec{H} corresponding with a magnetic flux density \vec{B} can be calculated by taking the gradient of the magnetic energy function:

$$\vec{H}(\vec{B}) = \nabla_{\vec{B}} W_{\text{em}}(\vec{B}) \quad (3.5a)$$

where $\nabla_{\vec{B}}$ denotes the gradient operator in \vec{B} -space,

$$\nabla_{\vec{B}} = \vec{e}_x \frac{\partial}{\partial B_x} + \vec{e}_y \frac{\partial}{\partial B_y}. \quad (3.5b)$$

Equation (3.5a) can be rewritten as

$$\vec{H}(\vec{B}) = \vec{e}_x \frac{\partial W_{\text{em}}(\vec{B})}{\partial B_x} + \vec{e}_y \frac{\partial W_{\text{em}}(\vec{B})}{\partial B_y} \quad (3.5c)$$

and hence the components of the magnetic field in the x - and y -direction can be expressed as

$$H_x(\vec{B}) = \frac{\partial W_{\text{em}}(\vec{B})}{\partial B_x} \quad (3.5d)$$

and

$$H_y(\vec{B}) = \frac{\partial W_{\text{em}}(\vec{B})}{\partial B_y} \quad (3.5e)$$

respectively. Taking into account that $\nu_{xx} = \partial H_x / \partial B_x$, $\nu_{xy} = \nu_{yx} = \partial H_x / \partial B_y$, $\nu_{yy} = \partial H_y / \partial B_y$, equation (3.2) can be rewritten in function of the magnetic energy function:

$$\begin{bmatrix} H_x \\ H_y \end{bmatrix} = \begin{bmatrix} \frac{\partial}{\partial B_x} \frac{\partial W_{\text{em}}}{\partial B_x} & \frac{\partial}{\partial B_y} \frac{\partial W_{\text{em}}}{\partial B_x} \\ \frac{\partial}{\partial B_x} \frac{\partial W_{\text{em}}}{\partial B_y} & \frac{\partial}{\partial B_y} \frac{\partial W_{\text{em}}}{\partial B_y} \end{bmatrix} \begin{bmatrix} B_x \\ B_y \end{bmatrix} \quad (3.6)$$

3.1.3 Magnetic measurements with the Epstein Frame

Using an Epstein frame, with a magnetic circuit as schematically shown in figure 3.1, it is possible to perform standardized (IEC 60404-2:2008) magnetic measurements on electrical steel sheets for sinusoidal alternating magnetic flux densities.

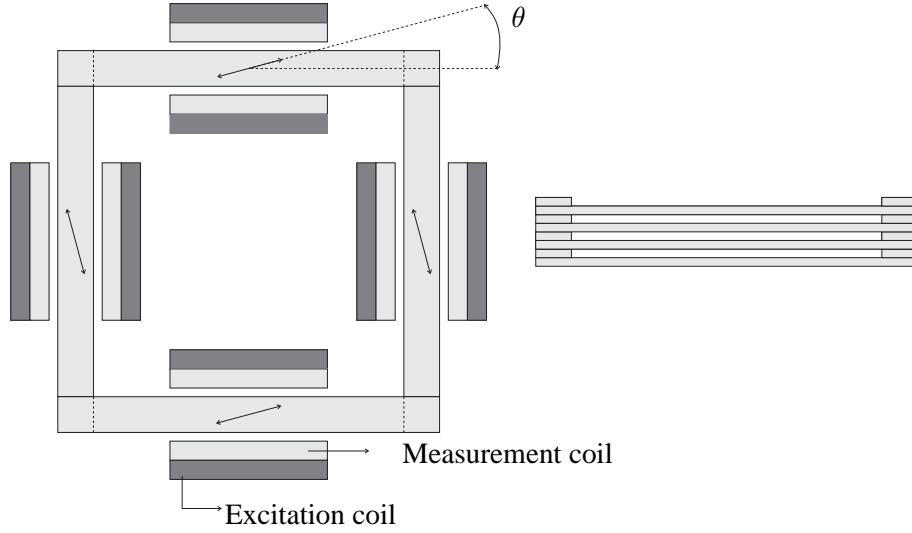


Figure 3.1: Schematic presentation of an Epstein frame. Left: horizontal cross section of the Epstein Frame with the measurement and excitation coils, where θ is the angle between the field excitation direction and the rolling direction in case of grain oriented material; right: side view of the Epstein frame [48].

The frame is constructed by alternately stacking strips of 3cm width and at least 28cm length. An excitation coil and a measurement coil are located around each stack of strips. The magnetic field strength \vec{H} is directly derived from the excitation current coming from the power amplifier, the number of coil turns and the standardized length of the magnetic path. According to the norm (IEC 60404-2:2008), the length of the magnetic path is 94cm.

In the measurement setup used for characterisation of the materials in the next section, the voltage and current limits for the excitation winding are 50V and 8A for the used Kepco 50-8M amplifier. The measured signals (excitation current and induced voltage in the search coil) are processed by the data acquisition system. The magnetic flux density \vec{B} is derived from the induced voltage in the measurement search coils. An analog integration is done to obtain the flux density waveform with high accuracy.

3.2 Characteristics of magnetic materials used in this PhD

3.2.1 Magnetic characteristics of grain oriented M100-23P

Several Epstein strips were cut from a MP100-23P laminated silicon steel sheet in seven different directions. The rolling direction is taken as a reference and is referred to the angle 0° . The other directions enclose an angle (θ in figure 3.1) of 15° , 30° , 45° , 60° , 75° and 90° with respect to the rolling direction. The angle 90° is referred to as the transverse direction (TD). For all grain oriented strips, several quasi-static hysteresis loops up to 7200 A/m were measured on the Epstein frame, which results in $B(H)$ characteristics along the seven considered directions as presented in figure 3.2. In [49], Epstein measurements were preferred over single sheet measurements, because the dimensions of the stator core laminations are in good approximation congruent to the shape of the Epstein strips. To estimate the elements of the tensor in (3.2), several dynamic loops were measured up to 1000 Hz. The frequency is limited to 1000 Hz because of the voltage limit of the amplifier. Figure 3.3 shows the relative permeability in function of the magnetic flux density for M100-23P grain oriented material in the rolling direction. As can be seen, the peak value for the relative magnetic permeability μ_r is more than 50000.

3.2.2 Magnetic characteristics of Soft Magnetic Composite

As an alternative to Laminated Silicon Steel Sheets (LSSS), Soft Magnetic Composite (SMC) can carry 3D flux paths and may in some applications increase the torque/weight ratio of the machine. SMC is mainly used in machines with complex 3D magnetic flux paths like transverse flux machines [50] or axial flux machines [23]. On the one hand, the isotropic behaviour of SMC is an advantage for these types of machines. Moreover, SMC does not suffer from induced currents due to fringing field perpendicular to the lamination. On the other hand, SMC has a lower magnetic permeability and higher losses (as described in the next section) in the frequency range that is relevant in electrical machines.

By using the Somaloy® prototyping material from the company Höganäs, it is possible to implement Soft Magnetic Composite material in experimental setups without the need of a dedicated mold for the compaction of the needed SMC components. By machining the SMC component out of a pre-fabricated cylindrical geometry, SMC can be implemented in a cost-efficient way. Normally, this approach has the drawback that the properties will in most cases be different from those obtained by compaction. This drawback vanishes using Somaloy® Prototyping material, because of the enhanced machinability (milling, turning and drilling) in order to minimize these differences.

In order to measure the magnetic characteristics of this Somaloy® prototyping

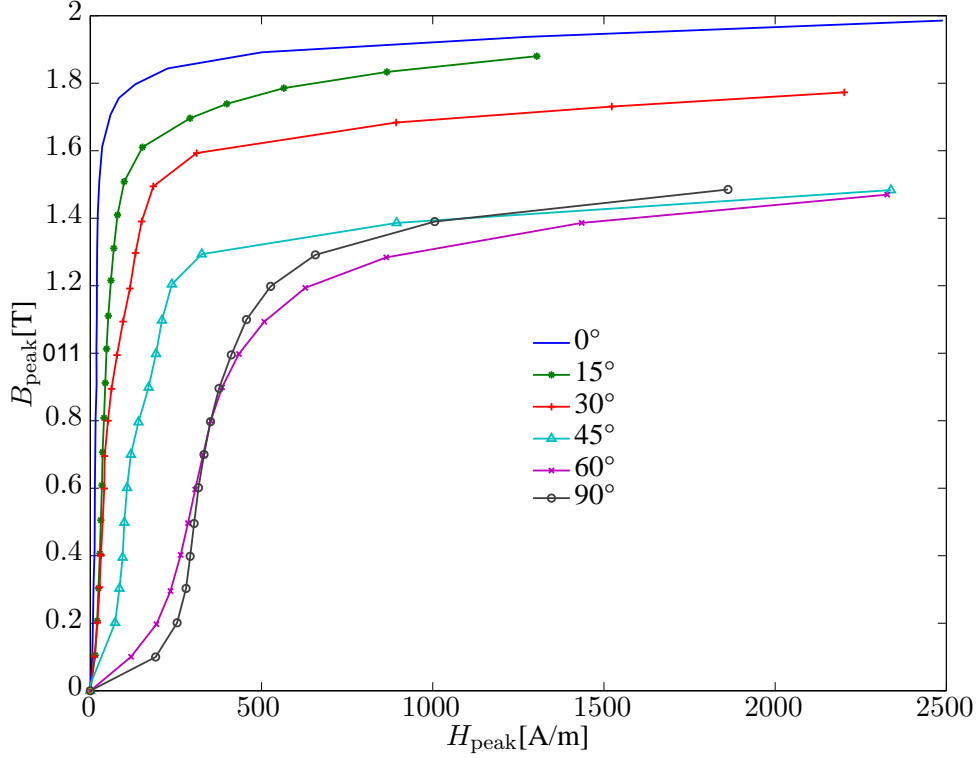


Figure 3.2: Quasistatic BH -characteristics of MP100-23P measured in seven directions with respect to the rolling direction. The mentioned angles are the angle θ in figure 3.1.

material, a dedicated setup is built. The reason for building this dedicated setup is that the company Höganäs does not provide toroidal cores of the Somaloy® prototyping material. For this reason, four SMC blocks with identical dimensions to the stator cores of the experimental setup of chapter 4 were made (by milling) out of four cylinders of Somaloy® prototyping material. A dedicated poly-amid position holder is used to position the four blocks in series, as shown in figure 3.6. The poly-amid position holder ensures that the airgaps between the SMC blocks are as minimal as possible. All blocks are equipped with an excitation coil and a measuring search coil of each 40 turns. Several quasi-static hysteresis loops up to 10000 A/m were measured on this dedicated setup, which results in the BH -characteristic as presented in figure 3.4. Figure 3.5 shows the relative permeability in function of the magnetic flux density for SMC Somaloy® prototyping material. As can be seen, a peak of $\mu_r = 290$ is reached, which is much lower than the peak value of 50000 for M100-23P.

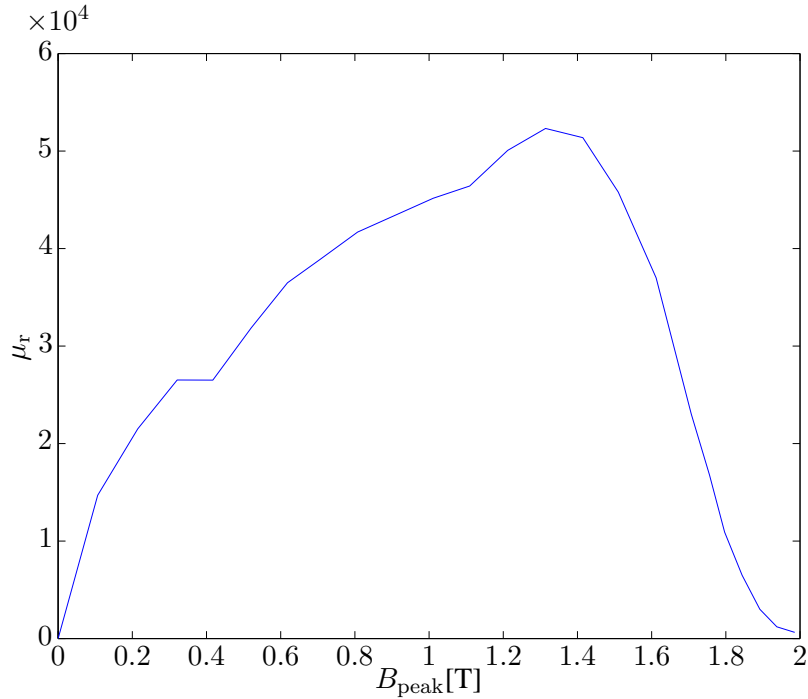


Figure 3.3: Relative magnetic permeability in function of the magnetic flux density for MP100-23P silicon steel in the rolling direction.

3.2.3 Magnetic characteristics of ferromagnetic wire

Ferromagnetic wire used to conduct magnetic flux instead of an electrical current can be used for example as a closing path for fringing fluxes.

To determine the BH -characteristics, a customized setup was made and measurements were done at Ghent University by prof. L. Dupré. The loss measurements are not performed with an Epstein frame because of ease of construction and because the Epstein method is not defined for wires. Also the number of cuts in ferromagnetic wire should be minimal. For this reason, the excitation and measurement windings were cylindrical windings of sufficient axial length and rather small diameters, having the ferromagnetic wire inside. The BH -characteristics are measured for an unannealed ferromagnetic wire with a diameter of 0.35mm, shown in figure 3.7. A maximum relative permeability of 800 is reached, as shown in figure 3.8.

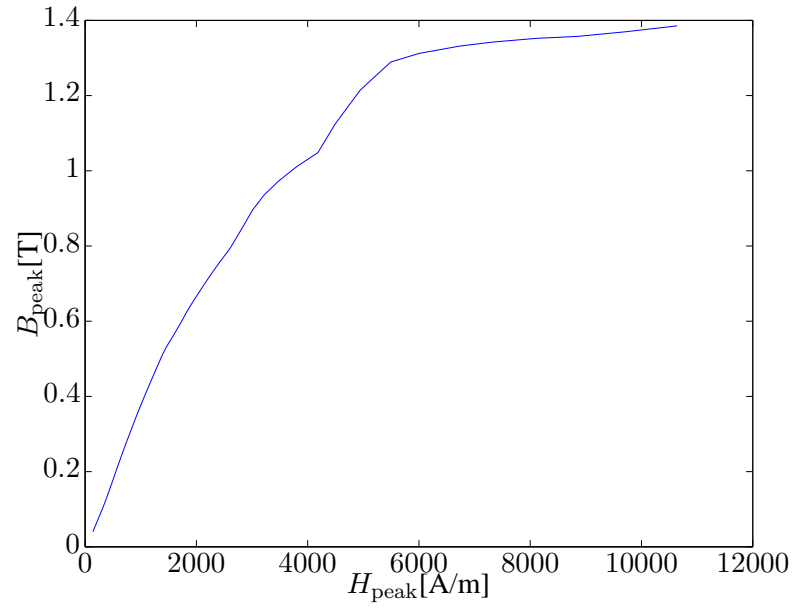


Figure 3.4: Quasistatic BH -characteristic of Somaloy® Prototyping material.

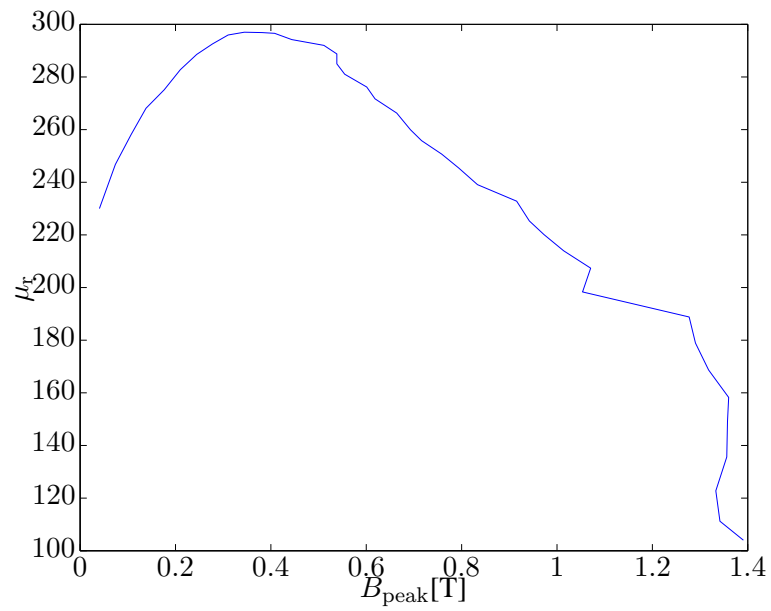


Figure 3.5: Relative magnetic permeability in function of the magnetic flux density of Somaloy® Prototyping material.

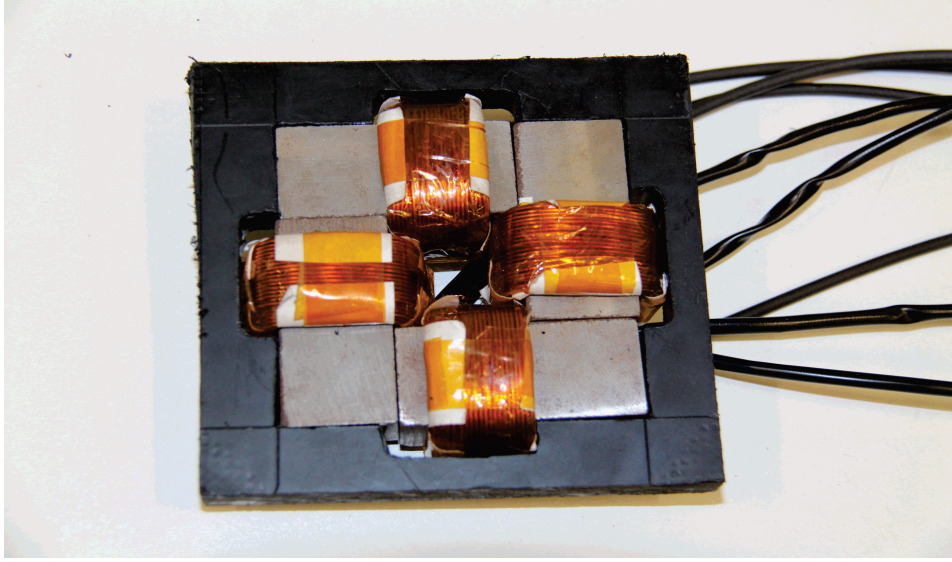


Figure 3.6: Measuring setup for SMC: four SMC blocks (light grey) placed in a custom made poly-amid position holder (black). The measurement and excitation windings consist of four concentrated windings each, like in an Epstein frame.

3.3 Loss modelling in magnetic materials

According to the loss theory of Bertotti [45], the iron losses in laminated steel are divided into the quasi-static hysteresis losses and the dynamic losses. The dynamic losses can be further divided into the classical dynamic losses and the extra dynamic losses (excess losses). For a periodic excitation, the losses per cycle and per volume-unit are as follows:

$$w_{\text{Fe}} = w_{\text{hys}} + w_{\text{dyn}} = w_{\text{hys}} + w_{\text{cl}} + w_{\text{exc}} \quad (3.7)$$

The unit of the above loss density is J/m^3 . Usually, the loss density is given in W/kg . The above loss density w_{Fe} can be converted to that unit by dividing by the mass density (typically 7650 kg/m^3) and multiplying with the frequency f .

3.3.1 Quasi-static loss component

The quasi-static loss component w_{hys} is the surface enclosed by the quasi static ($f \rightarrow 0$) BH -loop with peak value B . If converted to a power in W/kg , it is approximated as follows:

$$P_h = aB^\alpha f \quad (3.8)$$

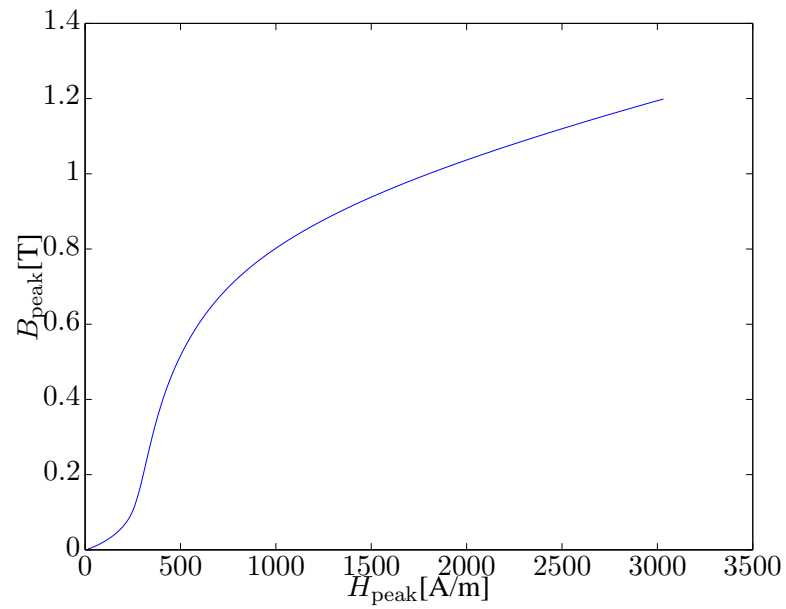


Figure 3.7: BH -characteristics of ferromagnetic wire with a diameter of 0.35mm.

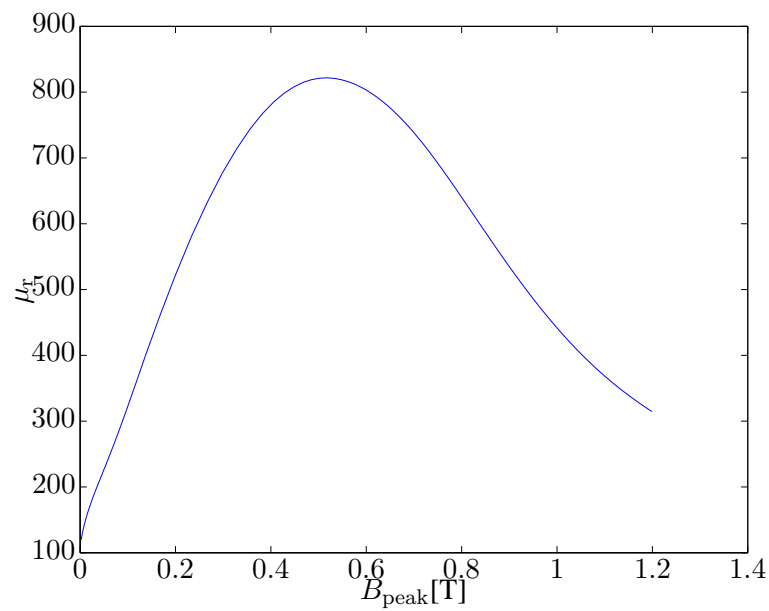


Figure 3.8: Relative magnetic permeability in function of the magnetic flux density for ferromagnetic wire with a diameter of 0.35mm.

with a and α material specific coefficients, fitted on the basis of quasistatic magnetic loss measurements. The above equation is only valid if the waveforms describe a closed hysteresis loop, and if there are no minor loops in the waveform.

3.3.2 Classical loss component: low frequency approximation

The classical losses for a perfect homogeneous lamination (without magnetic domains), neglecting the skin effect can be approximated by Bertotti's low frequency approximation in the frequency domain:

$$P_{cl} = \frac{1}{6} \sigma \pi^2 d^2 f^2 B^2 \quad (3.9)$$

or in the time domain for an arbitrary waveform $B(t)$

$$P_{cl}(t) = \frac{1}{12} \sigma d^2 \left| \frac{dB(t)}{dt} \right|^2 \quad (3.10)$$

with d the lamination thickness.

3.3.3 Classical loss component: 1D diffusion problem

Taking the skin effect into account and calculating the classical losses very accurately and with a high spatial accuracy, Bertotti's low frequency approximation is no longer an option in the considered grain oriented material with very high relative permeability (up to 50000, as can be seen in figure 3.3), because of skin effects, even for frequencies that may be lower than the rated frequency of the electric machine studied in this PhD. Assuming the operating point at maximal permeability and a lamination thickness of 0.23mm – which is thinner than most laminations used in electrical machines – we obtain a critical frequency f_{crit} where the skin depth

$$\delta_{crit} = \sqrt{\frac{1}{\pi f_{crit} \mu_0 \mu_{r,Fe} \sigma_{Fe}}} \quad (3.11)$$

equals half the lamination thickness $d/2$:

$$f_{crit} = \frac{1}{\pi \left(\frac{d}{2}\right)^2 \mu_0 \mu_{r,Fe} \sigma_{Fe}} \quad (3.12)$$

For $d/2 = 0.115\text{mm}$, $\mu_{r,Fe,max} = 50000$ and $\sigma_{Fe} = 1.67 \cdot 10^6 \text{ S/m}$ (explained in section 3.4.1) we obtain a critical frequency of 229 Hz. Above this frequency, the low frequency approximation is not valid any more.

For this reason, a one-dimensional space diffusion problem [51] is solved for half of the lamination thickness. The lamination and reference frame are shown in figure 3.9.

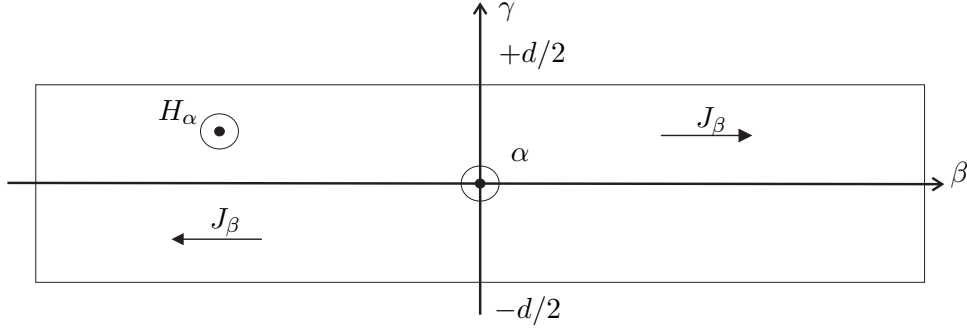


Figure 3.9: Cross-section of the lamination of figure 2.1.

The magnetic field intensity in the out-of-plane direction H_α of figure 3.9 is calculated from:

$$\frac{\partial^2 H_\alpha}{\partial \gamma^2} = \sigma \frac{dB}{dH_\alpha} \frac{\partial H_\alpha}{\partial t} \quad (3.13)$$

where H and B are respectively the magnetic field strength and magnetic flux density component in the out-of-plane direction, σ the electrical conductivity and γ the transverse direction of the lamination. Half the lamination is discretised in space from $i = 1 \dots n_s$ and in time from $k = 1 \dots n_t$. The discrete counterpart in the space-time domain at nodes defined by the time k and space point i reads:

$$\frac{1}{h^2} (H_{i+1,k} - 2H_{i,k} + H_{i-1,k}) = \frac{\beta_d}{p_i} (H_{i,k+1} - H_{i,k}), \quad (3.14)$$

With

$$\beta_d = \sigma \frac{dB}{dH} \quad (3.15)$$

and with p_i the time interval between two successive values of H_i over time at space node i , and h the mesh length representing the length between adjacent nodes in space [25]. This gives the explicit equation:

$$H_{i,k+1} = rH_{i+1,k} + (1 - 2r)H_{i,k} + rH_{i-1,k}, \quad (3.16)$$

Where

$$r = \frac{p_i}{\beta_d h^2}; \quad (3.17)$$

Using the explicit equation for calculating the magnetic field at each node, the following restriction arises to ensure numerical stability:

$$r \leq \frac{1}{2} \quad (3.18)$$

To ensure numerical stability, it becomes advantageous to apply the magnetic field waveform instead of the magnetic flux density in function of time. A sinusoidal excitation gives a non-sinusoidal response in the non-linear case. For this

reason, for obtaining a sinusoidal $B(t)$, a non-sinusoidal $H(t)$ must be used as excitation source in both measurements and simulations. Here, the non-sinusoidal magnetic field waveforms measured with the Epstein frame are used for exciting the 1D diffusion model, to ensure numerical stability. This is the magnetic field at the boundary of the lamination.

As an illustration of the 1D diffusion model, we consider a M100-23P lamination of 0.23mm thickness, where the magnetic field waveform at the boundary is enforced as source term in the model. This magnetic field waveform is shown in figures 3.10 and 3.11 for a frequency of 50Hz and 500Hz respectively. Note that the magnetic flux density waveform is non-sinusoidal because only classical losses were considered; hysteresis and excess contributions are not taken into account, in this model, which focusses on an acceptable prediction of eddy-current losses. The response of the model is the dynamic hysteresis loop of only the classical losses, which is shown in figure 3.12 and 3.13. Measurements around the area for a magnetic field strength of zero are inaccurate because of noise, this causes the discontinuity around the area where the magnetic flux density is zero. Taking the surface integral of these dynamic hysteresis loops, multiplied with the frequency and divided by the density of the material, gives the classical losses. In figure 3.10, it can be seen that there is no skin effect. In figure 3.11, skin effect is present. This can be seen by comparing the magnetic field at the boundary with the magnetic field at the middle of the lamination at a certain time instant.

For the same example, a comparison is made between the low frequency approximation of Bertotti, and the 1D diffusion model.

3.3.4 Excess loss component

The extra dynamic losses are associated with the eddy currents around moving domain walls due to the changing domain wall structure and are approximated by the equation from Barbisio [46] in the frequency domain:

$$P_e = c_f B f (\sqrt{1 + e_f B f} - 1) \quad (3.19)$$

or in the time domain for an arbitrary waveform $B(t)$

$$P_e = c_t \left| \frac{dB}{dt} \right| \left(\sqrt{1 + e_t \left| \frac{dB}{dt} \right|} - 1 \right) \quad (3.20)$$

with c_f , c_t , e_f and e_t material specific coefficients, fitted on the basis of Epstein frame measurements.

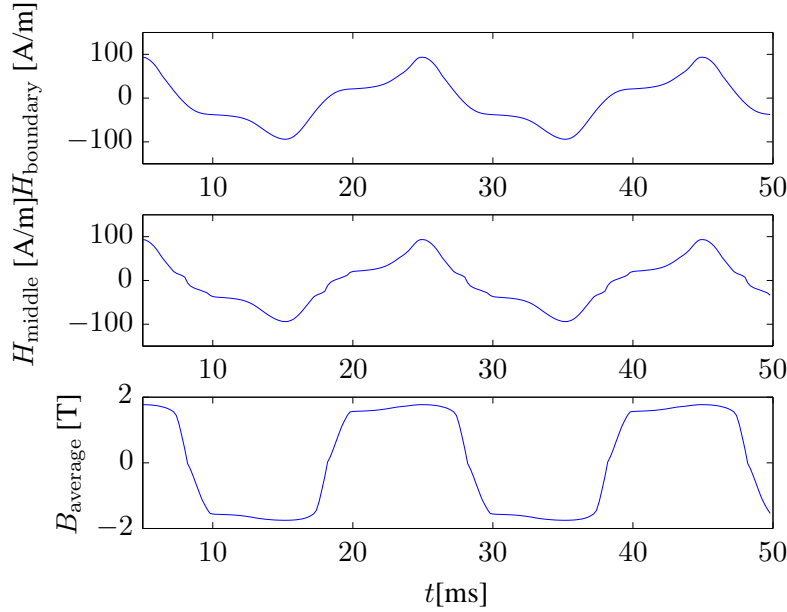


Figure 3.10: Magnetic field strength at the boundary H_{boundary} and in the middle H_{middle} of the M100-23P lamination together with the average magnetic field density B_{average} at a frequency of 50Hz.

3.4 Losses of magnetic materials used in the PhD

3.4.1 Losses of grain oriented M100-23P

For all FE models, the same BH -characteristic for grain oriented silicon steel is used. Figure 3.14 shows the fitted total iron losses for M100-23P grain oriented silicon steel based on Epstein frame measurements, using the low frequency approximation of Bertotti for the classical losses. This fitting is done by firstly fitting the hysteresis losses on the base of a quasi-static BH -loop measurement. Secondly the classical losses together with the excess losses and the calculated hysteresis losses are fitted. Figure 3.15, shows the fitted total iron losses for M100-23P grain oriented silicon steel based on Epstein frame measurements for the hysteresis and excess losses and the 1D diffusion model for the classical losses. This fitting is done by firstly calculating the classical losses by use of the 1D diffusion model. Secondly the hysteresis losses are fitted on the base of a quasi-static BH -loop measurement. At last, the excess losses are fitted on base of the total losses subtracted from the calculated classical losses and hysteresis losses. In both figures 3.14 and 3.15, there are differences at low flux density levels and low frequencies. These differences are related to the fact that standard fitting routines available in MATLAB®, cannot find an optimal fitting for both low and high flux density levels.

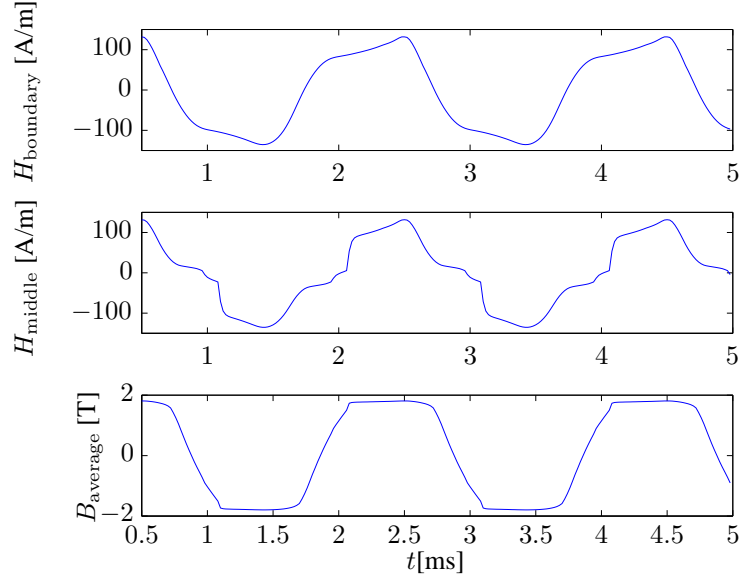


Figure 3.11: Magnetic field strength at the boundary H_{boundary} and in the middle H_{middle} of the M100-23P lamination together with the average magnetic field density B_{average} at a frequency of 500Hz.

Asymptotic behaviour of the BH -curve

The measurement of the BH -curve is restricted by the voltage and current limits of the measurement setup. The point of total saturation is mostly out of the measurement range. For this reason, it is necessary to extend the BH -curve before application in the FE model [52]. The BH -curve is extended starting from the last measurement point as:

$$B(H) = \mu_0 H + M_{\text{sat}} \quad (3.21)$$

Obtaining the conductivity tangential to the plane of the sheets

The conductivity is required for magnetic loss models. It is measured with a four point DC meter and by use of Pouillet's law:

$$R = \frac{l}{\sigma S} \quad (3.22)$$

with R the electrical resistance, S the cross-section of the conductor and l the length of the conduction path. The conductivity depends on the fraction of silicon in the steel, for example, steel with much silicon has a conductivity of about $2 \cdot 10^6$

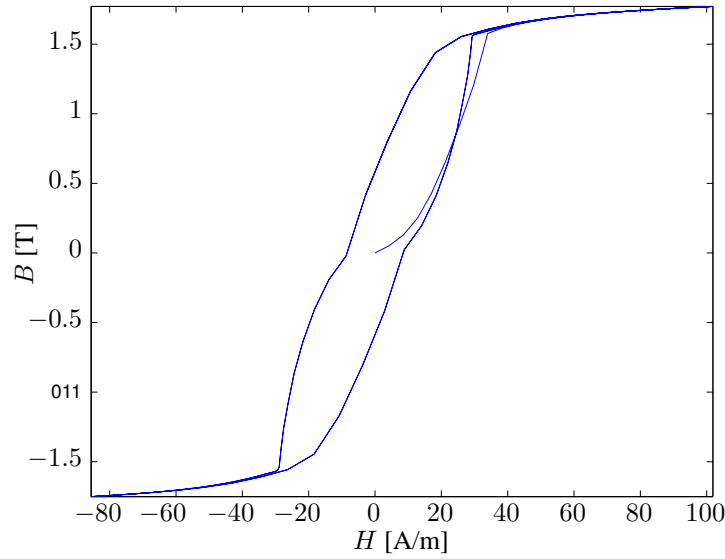


Figure 3.12: Dynamic hysteresis loops as a response of the 1D model at a frequency of 50Hz. The loops are for M100-23P but do not include hysteresis or excess loss components.

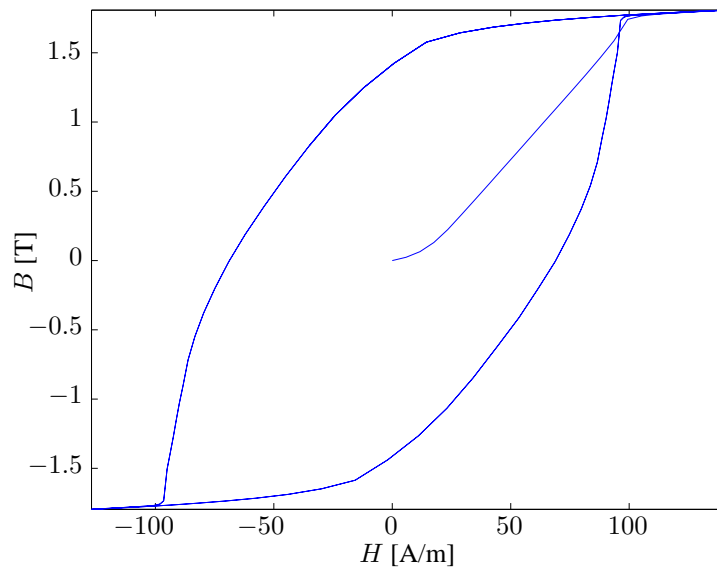


Figure 3.13: Dynamic hysteresis loops as a response of the 1D model at a frequency of 500Hz. The loops are for M100-23P but do not include hysteresis or excess loss components.

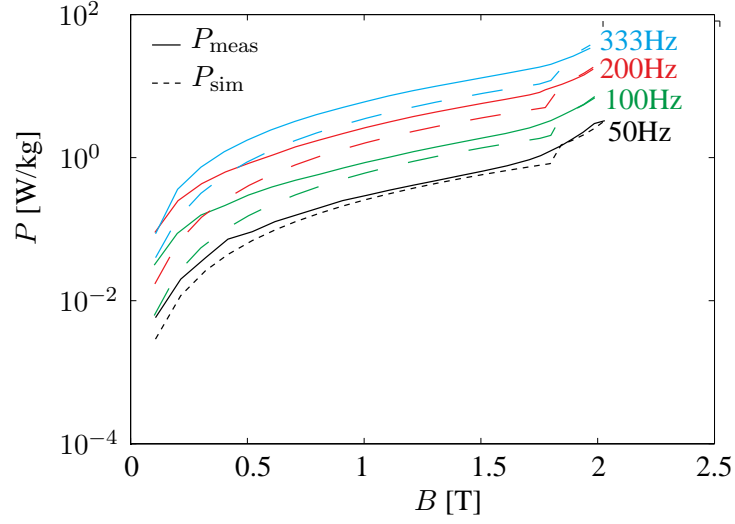


Figure 3.14: Fitted total iron losses P_{sim} in the rolling direction of M100-23P grain oriented silicon steel based on Epstein frame measurements (P_{meas}), using the low frequency approximation of Bertotti for the classical losses.

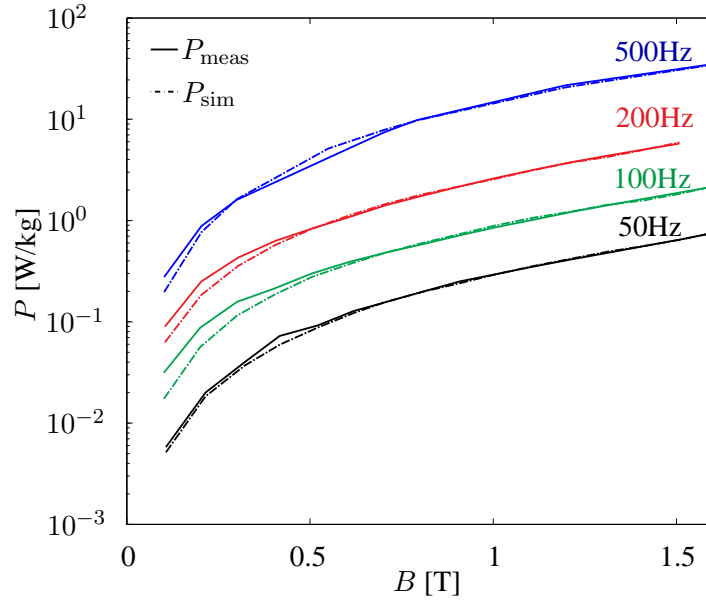


Figure 3.15: Fitted total iron losses (P_{sim} in the rolling direction of M100-23P grain oriented silicon steel based on Epstein frame measurements (P_{meas}), using the 1D diffusion model for the classical losses.

S/m whereas for a lower fraction of silicon, the conductivity is about $3 \cdot 10^6$ S/m. The conductivity of M100-23P silicon steel is $1.67 \cdot 10^6$ S/m.

3.4.2 Losses of Soft Magnetic Composite

For the core elements made of SMC, the classical losses are computed by homogenised material parameters in FEM. The classical losses are directly calculated from the current densities of the 3D non-linear FE model (described in section 2.3.6) by:

$$P = \int_V \frac{\vec{J} \cdot \vec{J}}{\sigma} dV \quad (3.23)$$

With σ provided by the manufacturer or measured as explained in paragraph 3.4.1. The magnetic losses are computed based on measurements on the measuring setup of Figure 3.6, which is described in section 3.2.2. Figure 3.16 shows the total measured iron losses of the SMC Somaloy® prototyping material measured on the SMC measuring setup together with the total iron losses of MP100-23P LSSS measured on an Epstein frame for a magnetic flux density of 0.5T, 1T and 1.5T. As can be seen, are the losses of the SMC Somaloy® prototyping up to 16 times larger than the losses in LSSS for low frequencies. For higher frequencies, the classical loss becomes high in the laminated material so that the difference is reduced to less than a factor 4 at 1000Hz and 1.5T.

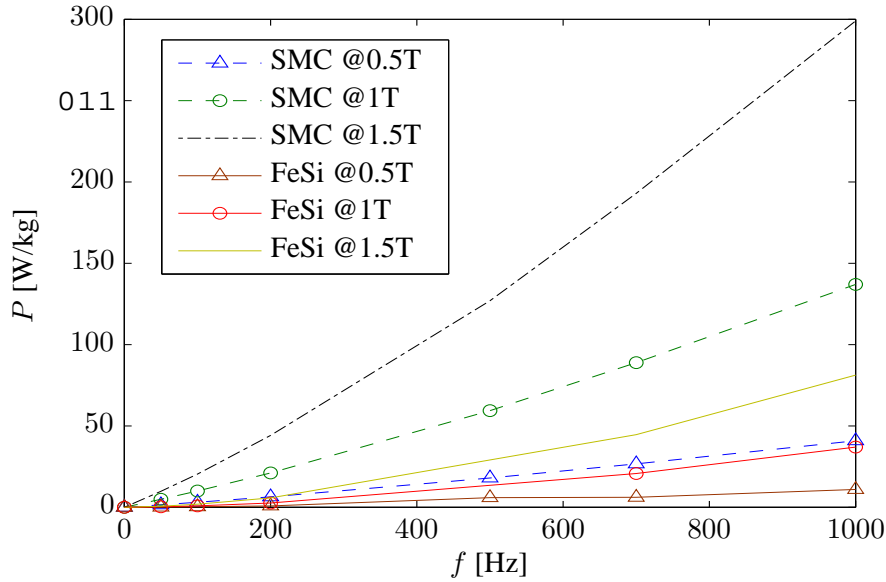


Figure 3.16: Losses for Somaloy® Prototype SMC and FeSi measured on Epstein frame for 0.5T, 1T and 1.5T.

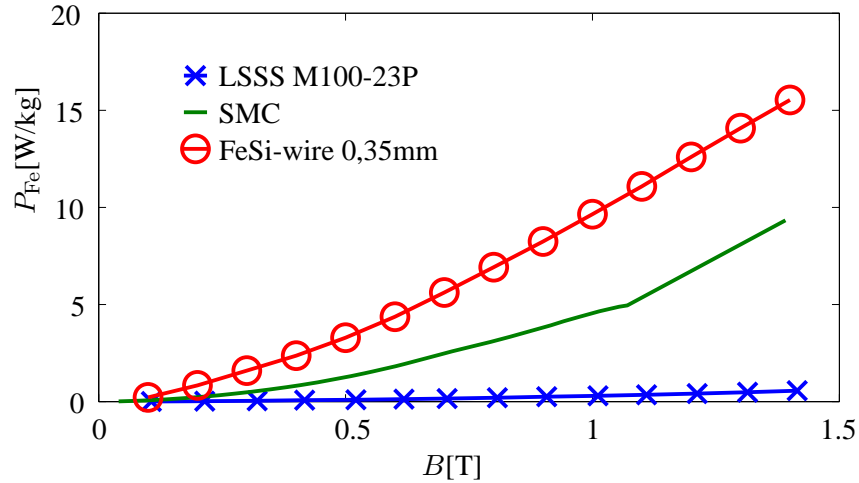


Figure 3.17: Total losses as a function of magnetic flux density for grain oriented M100-23P, SMC and FeSi-wire at a frequency of 50 Hz.

Because of the isotropic behaviour, SMC is mainly used for machines with a complex 3D path like transverse flux machine [50] or axial flux machines [23]. On the one hand, SMC does not suffer from induced currents due to fringing field perpendicular to the laminations. But, on the other hand, SMC has a lower magnetic permeability and higher losses in the frequency range that is relevant in electrical machines: see figures 3.17 and 3.18. By a clever combination of SMC tooth tips with LSSS, the advantageous material properties can be optimally exploited. In chapter 4 SMC tooth tips are combined with a rectangular stack of laminated silicon steel sheets.

3.4.3 Losses of ferromagnetic wire

The losses of the 0.35 mm ferromagnetic wire together with the losses of the Somaloy® Prototype SMC and the losses of M100-23P GO laminated silicon steel are shown in figure 3.17 for 50 Hz and in figure 3.18 for 200 Hz.

3.5 Homogenisation methods for eddy-current losses in steel laminations

A stack of grain oriented laminated steel sheets is both pseudo and crystalline anisotropic. The pseudo anisotropy comes from the heterogeneity caused by the

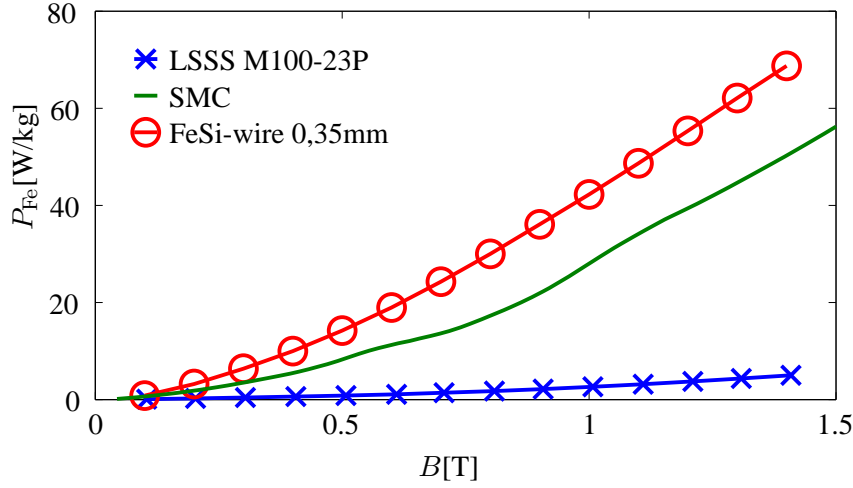


Figure 3.18: Total losses as a function of magnetic flux density for grain oriented M100-23P, SMC and FeSi-wire at a frequency of 200 Hz.

Figure 3.19: Losses for ferromagnetic wire

insulation between adjacent sheets. The crystalline anisotropy is due to the manufacturing (rolling) process of the individual sheets. The straightforward treatment of the lamination stack consists of drawing all lamination sheets and their insulation layers separately, assigning appropriate material data, defining the neighbouring coils, meshing the laminations explicitly and starting a 3D field simulation (Fig. 3.20). Using the straightforward treatment would lead to unmanageably large computational grids. Instead, the lamination stack is typically modelled by bulk material with surrogate material properties, via *homogenisation* [38, 53, 54] or an iteration between the macro-scale model and a number of meso-scale models (*multi-scale* techniques) [24, 44, 55]. A trade-off has to be found between the complexity of the technique and its accuracy.

3.5.1 Methods for homogenising the magnetic behaviour

This section sets up a comparison between a number of existing homogenisation techniques for laminated stacks. In figure 3.21, the lamination stack is shown, consisting of a highly permeable material and a non-magnetic space between the adjacent laminations (isolation and/or air). When the lamination (thickness d) and the isolation (thickness h) are excited by the same mmf (causing a magnetic field strength in the direction parallel to the lamination and isolation), the magnetic flux

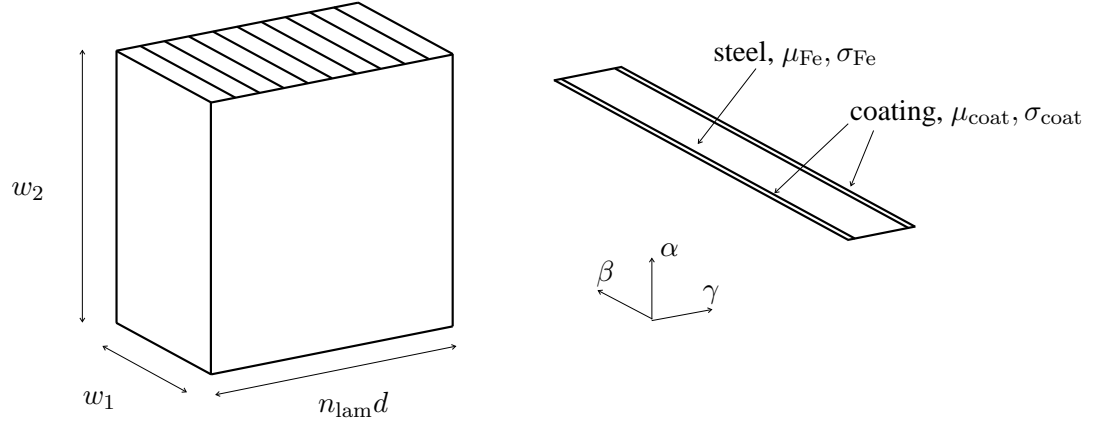


Figure 3.20: Stack of lamination sheet and coating layers.

density \vec{B}_{isol} in the space between the adjacent sheets is much lower than the magnetic flux density in the lamination \vec{B}_{lam} . We define the *stacking factor*, the ratio of steel material volume to total volume:

$$\chi = \frac{d}{d + h} \quad (3.24)$$

Typical values for this factor and the way to obtain it are given in section 3.5.3.

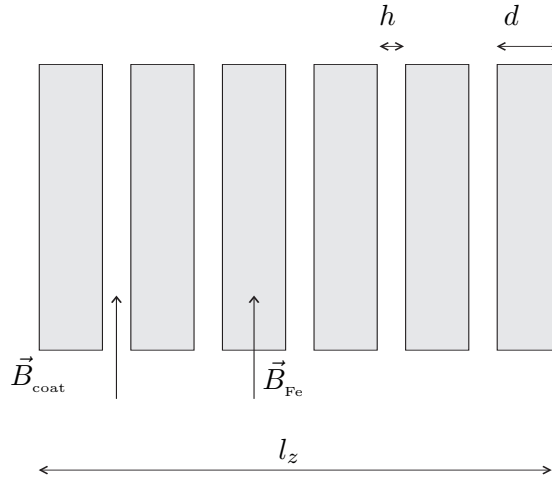


Figure 3.21: Lamination stack.

Method 1: In this method, a lamination is considered with the stacking direction along the γ -direction (Fig. 3.20). The reluctance experienced by the main flux

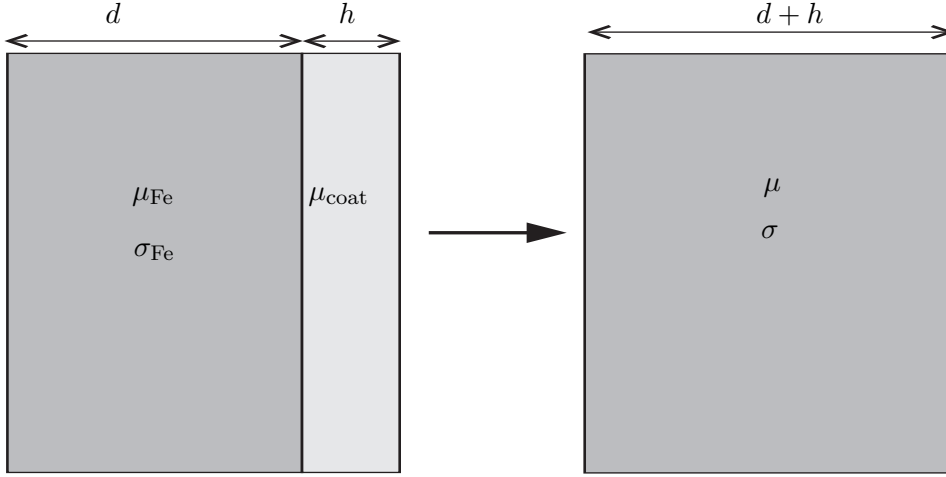


Figure 3.22: Homogenisation of laminated structure.

(flux parallel to the laminations) is found by a parallel connection of the reluctances of the path alongside the lamination itself and alongside the coating. The perpendicular flux component experiences a series connection of the highly permeable lamination part and the coating. The insulating coating between the individual lamination sheets causes a significant change to the permeability and the conductivity in the γ direction, and the allowable current paths. The electrical conductivity is set to zero in the perpendicular direction: $\sigma_\gamma = 0$.

A simple homogenisation leads to diagonal reluctivity $\bar{\bar{\nu}}$ and conductivity $\bar{\bar{\sigma}}$ tensors [24]:

$$\begin{cases} \bar{\bar{\mu}} &= \text{diag}(\mu_{\alpha\beta}, \mu_{\alpha\beta}, \mu_\gamma) \\ \mu_{\alpha\beta} &= \chi\mu_{\text{Fe}} + (1 - \chi)\mu_{\text{coat}} \\ \frac{1}{\mu_\gamma} &= \frac{\chi}{\mu_{\text{Fe}}} + \frac{1-\chi}{\mu_{\text{coat}}} \\ \bar{\bar{\sigma}} &= \text{diag}(\sigma_{\alpha\beta}, \sigma_{\alpha\beta}, 0) \\ \sigma_{\alpha\beta} &= \chi\sigma_{\text{Fe}} \\ \sigma_\gamma &= 0 \end{cases} \quad (3.25)$$

where χ is the *stacking factor* defined in (3.24), μ_{Fe} and σ_{Fe} are the permeability and conductivity of steel and μ_{coat} is the permeability of the coating material [54]. For conciseness, we formulate the theory for an isotropic and linear steel material and a non-conductive coating material. The extension to the non-linear case is derived in [56].

Method 2: In method 1, σ_γ is set to 0, which excludes the eddy currents generated by the magnetic fluxes parallel to the sheets. From an analytical 1D model, one can represent the eddy-current effect as a magnetisation, i.e., $\vec{H} =$

$\nu \vec{B} + \frac{1}{12} \sigma_{\text{Fe}} d_{\text{lam}}^2 \frac{d\vec{B}}{dt}$ [38]. This is easily incorporated, and can be added to Method 1 as an anisotropic, complex-valued reluctivity $\nu_{\alpha\beta} \rightarrow \nu_{\alpha\beta} + j\omega \frac{\sigma_{\text{Fe}} d_{\text{lam}}^2}{12}$ in \mathbf{M}_ν in the frequency domain model of section 2.3.5.

The straightforward method for modelling the lamination stack which consists of drawing all lamination sheets and their insulation layers separately, considers all variations of the electromagnetic fields at the scale of the individual laminations, whereas Method 1 and Method 2 neglect them completely. Nevertheless, Method 1 and Method 2 are assumed to represent the same macroscopic behaviour of the lamination stack as the straightforward method. However, Method 1 and Method 2 may become very inaccurate, especially when the magnetic flux pattern is nontrivial. A compromise is found in Method 3:

Method 3: In this method, the individual laminations are resolved by mesh elements but the coating layers are only related to mesh planes. The magnetic behaviour of the coating layers is considered by a thin low-permeability interface condition [41], as explained in 2.3.3. This amounts to adding reluctances of the form $\frac{h}{\mu_{\text{coat}} |A_p|}$ where A_p are the incident primary-grid faces to \mathbf{M}_ν of equation (2.3.5).

3.5.2 Methods for homogenising the electric behaviour

Resolving the individual sheets in the mesh is not sufficient to correctly model the proper current paths. Several techniques to numerically prevent current migration between the insulated sheets are:

- Currents in the γ -direction are prohibited automatically by the conductivity tensor as in (3.25), used in *Method 1* and *Method 2*.
- Currents are allowed to migrate between the sheets, thereby drifting away from the true current pattern. However, the conductivity tensor is adapted as proposed in [53]. In order to obtain correct results for the eddy-current losses, the following requirements were taken into account: the dissipated powers and the magnetic fields outside the core must be the same for the homogenised and the real model. The latter requires that the total current at the surface must be equal.
- Migration of currents between the laminations is prevented by an integral constraint on the currents, forcing the current through the sheet surfaces to be zero [44].

3.5.3 Stacking factor of a lamination stack

Thin sheets (typically 0.2 – 1.0 mm) have an insulating coating layer of typically 1–15 μm , leading to a stacking factor χ – see (3.24) – of at least 95% for a material of 0.35 mm thickness, or 97% for a material with 0.50 mm thickness [57]. When

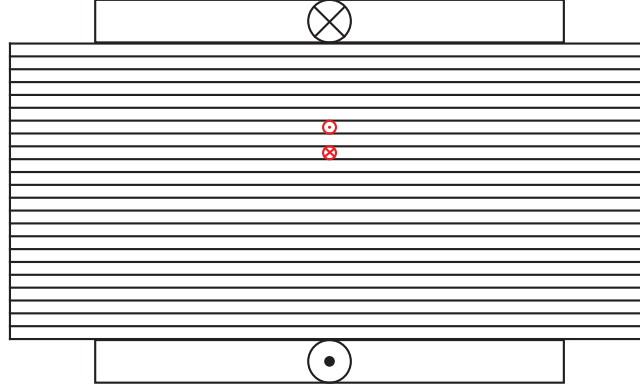


Figure 3.23: Excitation winding around a laminated stack with a measurement winding between the laminations (shown in red).

modelling the lamination stack of figure 3.21 by taking the gross thickness of the lamination stack as the active length l_z , it becomes necessary to recalculate the real material characteristics of the lamination steel (net thickness d) to the gross thickness ($d + h = \frac{d}{\chi}$) in the FE model. For example in 2D FEM, the real flux density in the lamination is then given by:

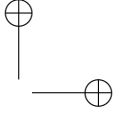
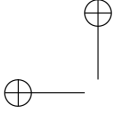
$$\vec{B}_{Fe} = \frac{1}{\chi} \vec{B}_{EE} = \frac{1}{\chi l_z} \left(\frac{\partial A_\gamma}{\partial \beta} \vec{1}_\alpha - \frac{\partial A_\gamma}{\partial \alpha} \vec{1}_\beta \right) \quad (3.26)$$

With \vec{B}_{EE} the 2D FE solution for the magnetic flux density over the gross thickness l_z and A_γ the magnetic vector potential in the γ direction.

Obtaining the isolation thickness

In order to obtain the width of the isolation between adjacent sheets, the following methods can be used:

- Method 1* By measuring the flux density in a single sheet of the lamination stack. This can be done by using a measurement winding placed between the sheets, as illustrated in figure 3.23. When the flux density is measured, the width of the isolation can be estimated by changing the width in a 2D FE model until the same magnetic flux density on the same place is reached, which constitutes an inverse problem.
- Method 2* By measuring the permeability in the transverse direction (circuit in series) and assuming that the permeability of the lamination (silicon steel) is infinite.
- Method 3* By measuring the total volume of a lamination stack V_{stack} , which is the sum of the volumes of the laminations and the coatings between the laminations.



Calculating the volume of the laminations V_{lam} out of the mass density of the material of the laminations (7650 kg/m^3 for silicon steel) and neglecting the mass of the isolation, the isolation thickness is given by:

$$h = \frac{V_{\text{stack}} - V_{\text{lam}}}{n_{\text{lam}} w_1 w_2} \quad (3.27)$$

With n_{lam} the number of laminations, w_1 and w_2 the “in-plane” height and width of one lamination respectively, see figure 3.20.

3.6 Equivalent geometry model for laminated media

Apart from homogenisation, another technique to simplify the meshing of the finite element model is using an equivalent geometry for the laminated structure as shown in figure 3.24 with an enlarged lamination and insulation thickness. This approach reduces the geometrical disproportion between the lamination and insulation thicknesses and the device size. In order to have equivalence between the original model (with parameters σ_{Fe} , μ_{Fe} , w_{Fe} , μ_0 and w_0) and the model with enlarged thickness (with parameters σ_1 , w_1 , μ_2 and w_2), we need to take into account the following conditions:

- The same skin depth:

$$\delta = \sqrt{\frac{2}{\omega \sigma_{\text{Fe}} \mu_{\text{Fe}}}} = \sqrt{\frac{2}{\omega \sigma_1 \mu_1}} \quad (3.28)$$

- The same reluctance for the parallel flux:

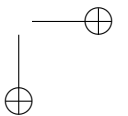
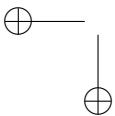
$$\mu_{\text{Fe}} w_{\text{Fe}} + \mu_0 w_0 = \mu_1 w_1 + \mu_2 w_2 \quad (3.29)$$

- The same reluctance for the series flux:

$$\frac{w_{\text{Fe}}}{\mu_{\text{Fe}}} + \frac{w_0}{\mu_0} = \frac{w_1}{\mu_1} + \frac{w_2}{\mu_2} \quad (3.30)$$

3.7 Post processing of finite element results

In the 2D FE model, the lamination stack is modelled by including thin low permeability interface conditions, representing the insulation. In the 3D model, the outer sheets are modelled explicitly. The inner sheets are modelled by a bulk material by homogenising the permeability and conductivity as shown in (3.25).



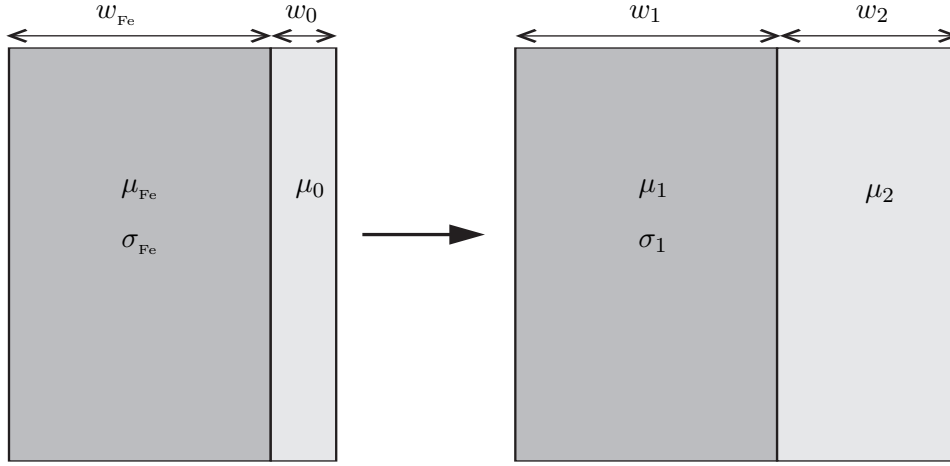


Figure 3.24: Equivalent geometry for a laminated structure.

The losses are determined in a post-processing step. The eddy-current losses due to perpendicular flux are calculated by:

$$P_{cl,fr} = \int_{V_{iron}} \frac{\underline{\mathbf{J}} \cdot \underline{\mathbf{J}}^*}{\sigma} dV \quad (3.31)$$

With $\underline{\mathbf{J}}$ the RMS complex phasor of the current density, $\underline{\mathbf{J}}^*$ the complex conjugate of $\underline{\mathbf{J}}$ and V_{iron} the volume of conducting material.

The material models are applied per triangle (2D model) or per primary-grid cell (3D model). As such, spatially distributed results for the loss densities are available. The total losses are determined by numerical integration.

3.7.1 Lamination stack: individually modelled sheets

For core elements made from LSSS, even for low excitation currents, the outer sheets of a LSSS stack saturate very quickly: see figure 3.25. This is mainly caused by stray fields perpendicular to the lamination. As a consequence, the eddy currents induced by these stray fields will be the highest in the first few sheets close to the excitation winding. To accurately compute the eddy currents caused by stray fields, the first few 0.23 mm thick sheets closest to the excitation winding are explicitly resolved by the FE mesh by defining them in the FE model as individual domains, separated by thin insulating (coating) layers of $15\mu\text{m}$. The two types of eddy currents as described in the introduction, cannot be strictly separated in the non-linear case, because they influence each other. For this reason, both eddy currents are calculated together in the first few sheets closest to the excitation winding. Knowing that the magnetic field is enforced in the rolling direction (stator field) and the

magnetic flux density is predominantly in the rolling direction, it is acceptable to neglect the crystalline anisotropy and to use a scalar magnetic material model.

3.7.2 Lamination stack: homogenisation of the stack

The remaining centre part of the laminated stack is modelled as a homogenised bulk material with anisotropic magnetic and electric properties, as suggested in [58] and shown in figure 3.25. For the centre part of the laminated stack, we use homogenisation method 1 described in section 3.5. The permeability in the direction perpendicular to the stack is determined by the coating thickness and lamination thickness. The pseudo anisotropy is taken into account by using an anisotropic electrical conductivity. The classical losses in this homogenised centre part are calculated separately using a 1D finite difference diffusion model of half the lamination thickness.

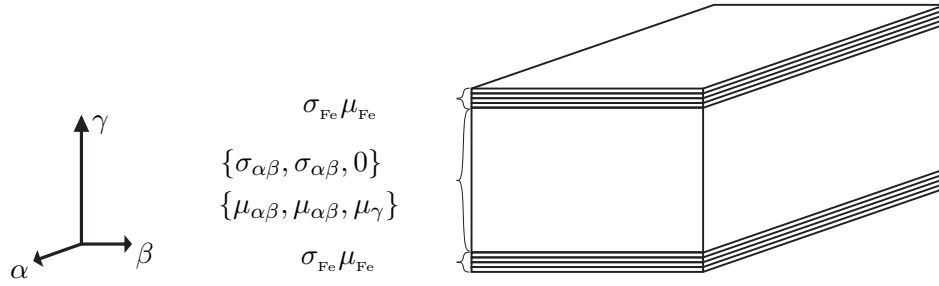
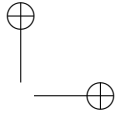
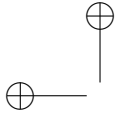


Figure 3.25: 3D stack with in the middle bulk material and at the top and bottom sheets

3.8 Conclusion

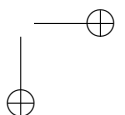
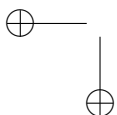
In this chapter, the characterisation of magnetic materials is described: the single-valued magnetic characteristic (the BH -characteristic), and the losses. For the losses, the loss theory of Bertotti is explained, with for the classical loss both the low frequency approximation and the 1D diffusion model in the lamination.

The characterisation is done for 3 magnetic materials that are used in this PhD: grain oriented M100-23P Silicon Iron with 0.23mm sheet thickness, Soft Magnetic Composite (Höganäs) and ferromagnetic wire. The first was measured by a conventional Epstein frame; the second and third were measured on customized setups. In the magnetic characteristic, it is observed that the maximal relative permeability differs a lot for the three materials: 50000 for the M100-23P, 290 for SMC and 800 for the ferromagnetic wire. In the losses, it is seen that the M100-23P has very



low losses at low frequency compared to the others, but at higher frequency, the difference becomes smaller.

In the last part of the chapter, homogenisation techniques are studied in order to model the laminated material in Finite Elements. Several techniques are described. In chapter 4 and 5, the first homogenisation method will be used for the part of the lamination stacks which is modelled as a bulk material. Finally, some details are given about material-related postprocessing in Finite Elements: the computation of eddy-current losses in the laminated stack, both the explicitly laminated stack and the homogenised stack.



Chapter 4

Fringing flux losses due to the armature reaction

4.1 Introduction

It is explained in earlier chapters that fringing flux is caused by on the one hand the (rotating) permanent magnets in the YASA machine, and on the other hand by the stator currents (armature reaction). This chapter focusses on fringing flux losses coming from the armature reaction of the YASA machine.

To avoid the complexity of a rotating machine, all simulations and measurements in this chapter are based on a simplified non-rotating setup. The geometry of the simplified setup is shown in figure 4.1a. This setup consists of two tooth coils (whereas the real machine has 15 such coils), a return yoke, and 2 air gaps with accurately controlled width. This setup is suitable for studying fringing flux losses caused by stator currents in the YASA machine, i.e. by the armature reaction. For this setup, a detailed analysis is given of the eddy currents due to fringing flux. As the setup has no moving magnets, fringing flux caused by the magnets cannot be studied in this chapter: this is studied in the next chapter.

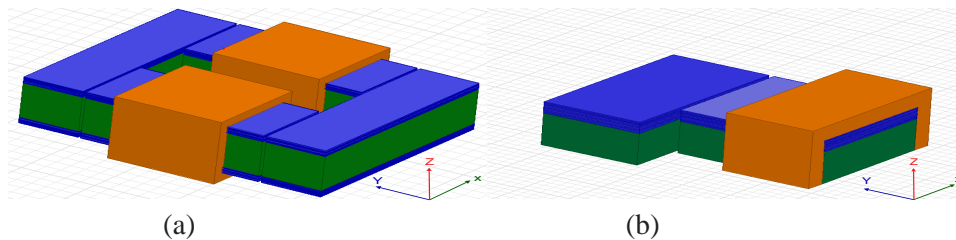


Figure 4.1: (a) Simplified setup (b) 3D FEM geometry exploiting symmetry and showing explicitly modelled laminations (blue) and the homogenized part of the lamination stack (green).

The several FEM models of chapter 2 are used and tested concerning their ca-

pability of modelling eddy currents due to fringing flux. The difference in accuracy between the FEM models is discussed. The simulations are validated by measurements on the simplified setup, and the validated field simulations give a very good idea of the cause and the behaviour of fringing flux losses caused by the armature reaction.

The last part of this chapter discusses three approaches for reducing these losses. The first method directly restricts the eddy-current losses by segmenting the lamination surface. The second method deflects the fringing flux by using Soft Magnetic Composite (SMC). The third method magnetically short-circuits the fringing flux using ferromagnetic wires. Here, the magnetic characterisation of SMC and ferromagnetic wire from chapter 3 is included in the modelling.

4.2 Simplified non-rotating experimental setup

Although the goal is to study iron losses in an axial flux machine, an experimental setup without moving parts is built, as shown in figure 4.2 and figure 4.3. This makes it possible to measure iron losses more accurately than in a setup with a moving rotor. As already mentioned, the focus of this section is on eddy currents due to fringing flux of the coils. For that reason, permanent magnets are not included in the setup. Four stacks of grain oriented material M100-23P with BH -characteristic and losses shown in chapter 3, and parameters collected in Table 4.1, are positioned at a pole width of 50 mm from each other. A laminated yoke of 20 mm thickness is provided. This is much larger than the real back iron of the axial flux machine studied in chapter 5, in order to keep the losses of the back iron low compared to those in the lamination stack. All surrounding material besides the lamination stacks and copper is polyamide. The airgap length can be varied in a very accurate way by moving the back-iron and stacks and inserting sheets of polyamide (of 1 mm thickness) between them. The grain oriented silicon steel sheets are cut by a water jet, in order to have minimal degradation of the magnetic properties in the regions near the cutting boundaries [59].

4.3 Comparison and discussion of different models

4.3.1 The models: 2D FEM, 3D FIT, and 3D FEM

To model the simplified, non-rotating setup, three different numerical models are considered: the 2D Finite Element Model described in section 2.3.3, the 3D Finite Integration Technique model, described in section 2.3.5 and the 3D Finite Element Model described in section 2.3.6. The used post processing is described in section sec:postprocessing. In this simplified setup, symmetries allow to only model one fourth of the geometry in 2D and one eighth of the geometry in 3D, accompanied by appropriate boundary conditions. In this way, the considered geometry consists

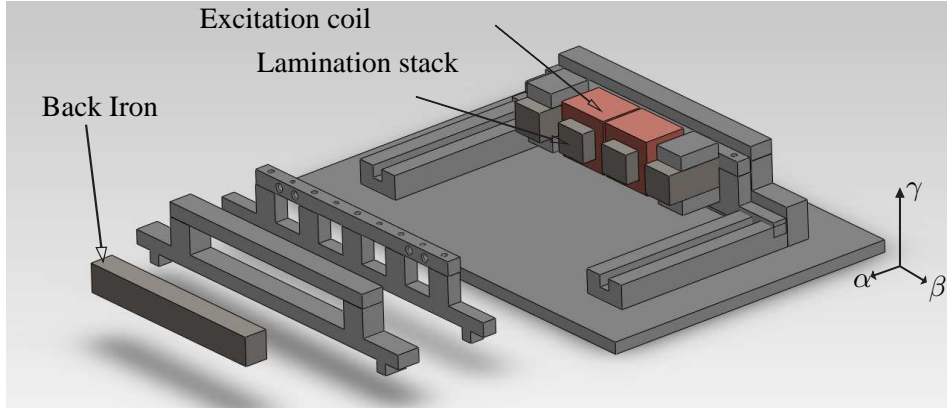


Figure 4.2: Experimental setup in exploded view

Table 4.1: Geometric and electromagnetic parameters for the simplified setup

Parameter	Value
Number of turns of one excitation coil	200
Grain oriented material grade	M100-23P
Lamination thickness (d)	0.23 mm
Insulation between adjacent sheets (h)	15.2 μm
Stacking factor (χ)	0.94
Stack width	28 mm
Stack height	24 mm
Stack depth	60 mm
Airgap width (variable)	0.0 – 5.0 mm
Conductivity (σ)	1.67 MS/m

of a lamination stack, a coil carrying a magnetising current, an air gap and a yoke closing the magnetic circuit. The geometry of the 2D FEM is shown in figure 4.4, the geometry of the 3D FIT and 3D FEM are shown in figure 4.1. In contrast to many approaches where the lamination stack is considered as a bulk material with homogenised material parameters, here, the individual lamination sheets are considered in all three numerical models. The relevant geometric parameters of the lamination stack are listed in Table 4.1. The 2D FEM and 3D FIT models are evaluated with a constant relative permeability of 10000. The 3D FEM model is evaluated in the non-linear case by use of an effective BH -curve, as described in chapter 3.

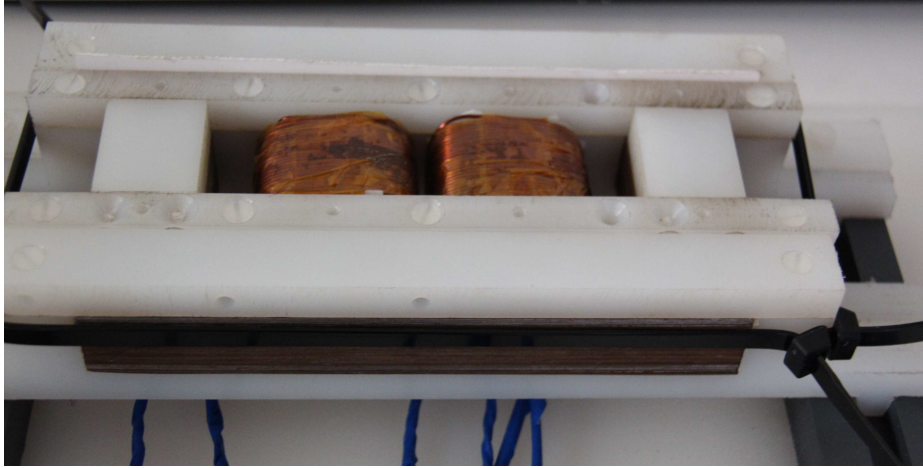


Figure 4.3: The simplified, non-rotating experimental setup

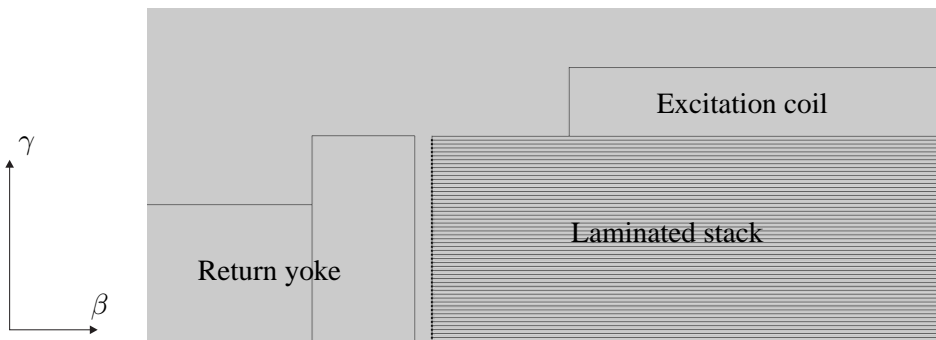


Figure 4.4: A section of a laminated stack in the YZ-plane is taken from the simplified setup of figure 4.1b. On the left side a yoke is provided as a conducting path for the magnetic flux. The insulation layers between adjacent sheets are modelled explicitly

4.3.2 Validation in the linear case

Only low currents are applied, because the top and bottom sheets of the stack saturate easily, even for weak currents. This can be seen in figure 2.10.

The losses due to perpendicular flux are plotted in function of the frequency in figure 4.5. It can be seen that the losses of the 2D model are slightly higher than the losses of the 3D model. This is mainly due to the fact that the returning paths for the eddy currents are not included in a 2D model, as they are inherently replaced by short-circuit connections between the front and back model sides. Further restrictions of the 2D model are:

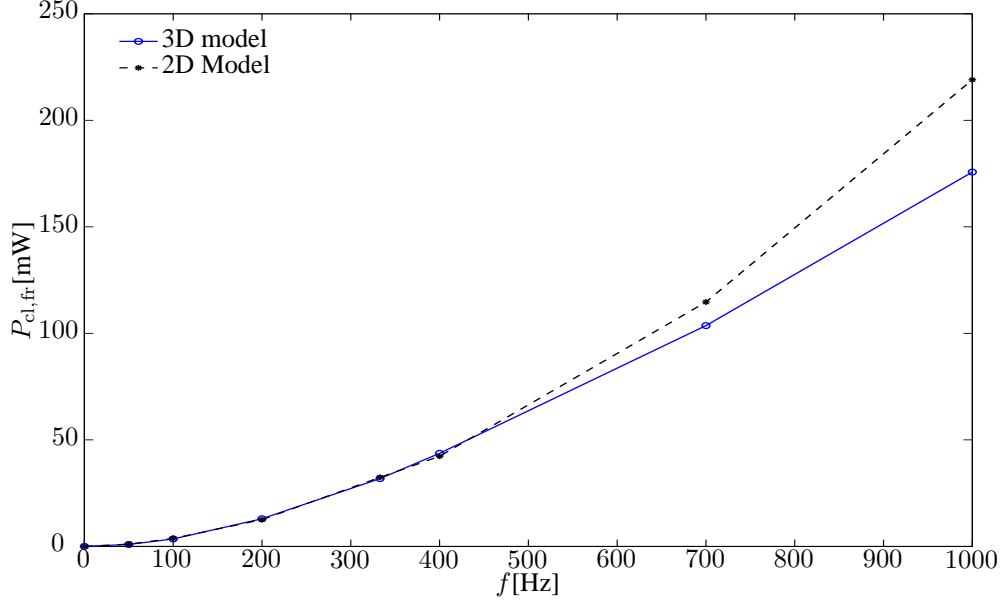


Figure 4.5: Comparison of the losses due to perpendicular flux calculated by the 2D and 3D FIT model for an excitation of 200A turns and an airgap width of 1 mm

- Flux migration between adjacent teeth (in the direction perpendicular to the modelled plane) is not considered.
- Only the losses in the stack are considered (not in the back iron).
- Crystalline anisotropy cannot be included.
- Only simple geometries can be modelled.

These restrictions vanish by using a 3D model, at the expense of a substantially larger number of unknowns and according computation time.

Figure 4.6 shows the total measured and modelled losses by use of the 3D FIT model, for an airgap of 1.0 mm. It can be seen that the results of simulations and measurements are in good agreement. This is easily explained by the main flux following mainly the rolling direction. The slight deviation may be attributed to the non-crystalline behaviour of the used grain oriented material, which is not included in the model.

Table 4.2 shows the individual components of the total losses, for an airgap of 1.0 mm, with f the frequency, I_{ex} the RMS excitation current, P_{meas} the total measured losses, P_{mod} the total modelled losses, $P_{cl,fr}$ the modelled losses due to perpendicular flux, P_h the hysteresis losses, P_{cl} the classical losses, P_{ex} the excess losses and % the increase of total loss due to perpendicular flux. A great part of

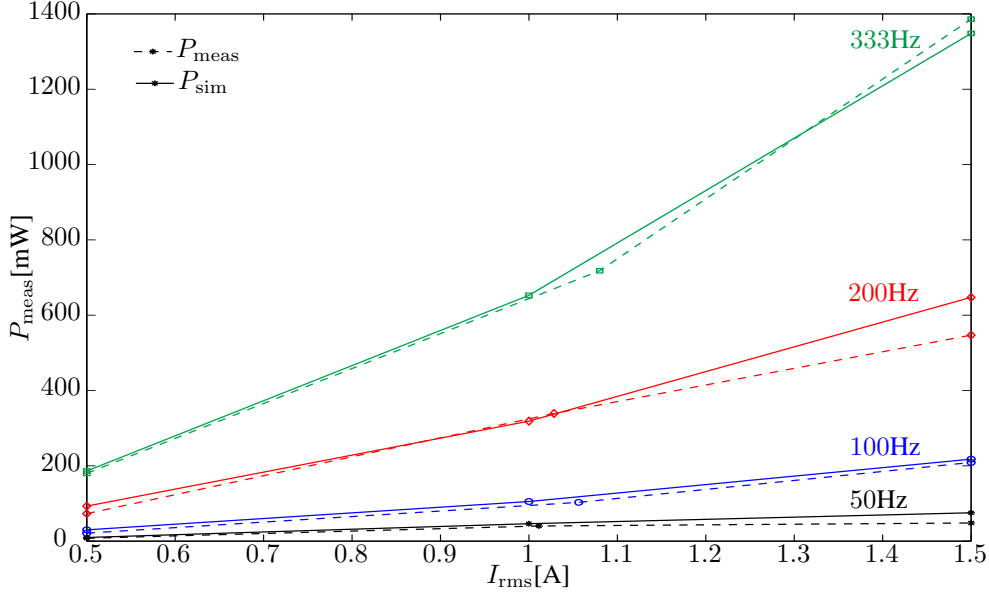


Figure 4.6: Comparison of the measured and simulated total losses P_{meas} and P_{sim} in mW, as a function of the rms current I_{rms} , the corresponding surface plot of the magnetic flux density is shown in figure 2.10 for a frequency of 50 Hz and 1 A rms excitation current.

the total losses consists of excess losses, because the setup is built of grain oriented silicon steel sheets. The highest increase of total loss related to perpendicular flux at this point is 3%.

4.3.3 Validation in the non-linear case

Figure 4.7 shows loss measurements on the AFPMSM setup for SMC and FeSi stator core elements at 0.5T and 1T. The difference between measured losses for the motor teeth made of on the one hand laminated silicon steel and on the other hand SMC is small because of the 3D flux path capability of SMC and the losses in the back iron. With the SMC teeth, the total iron losses increase by a factor of 1.5 on average, while in chapter 3 an increase by a factor 4 to 16 was observed. This fact is explained by the substantial eddy-current losses induced in the LSSS by fringing fluxes perpendicular to the laminates.

The 3D model is evaluated and compared with the measurement data for both materials. Figure 4.8 shows the total measured and total modelled loss of the AFPMSM setup for LSSS at frequencies of 50, 100 and 200 Hz. It can be seen that the loss due to fringing field increases more rapidly than the total loss because the loss due to fringing field increases quadratically with the magnetic flux density.

Table 4.2: Measured and calculated losses on the simplified setup. The last column is the percentage of fringing flux loss $P_{cl,fr}$ in the total iron losses.

f [Hz]	I_{ex} [A]	P_{meas} [mW]	P_{mod} [mW]	$P_{cl,fr}$ [mW]	P_h [mW]	P_{cl} [mW]	P_{ex} [mW]	%
50 Hz	0.5	7.6	5.53	0.12	2.04	0.63	2.53	2.25
	1	40.2	20.7	0.5	8.14	2.52	9.54	2.4
	1.5	48.2	45.5	1.1	18.3	5.66	20.5	2.4
100 Hz	0.5	21.2	16.6	0.5	4.09	2.53	9.57	3.0
	1	103	63.3	1.8	16.4	10.11	35	2.8
	1.5	209	137.03	4.1	36.8	22.74	73.4	3
200 Hz	0.5	73	55.1	1.5	8.25	10.2	35.2	2.7
	1	339	204	6.1	33	40.8	124	3
	1.5	547	434	13.7	74.2	91.8	254	3.2
333 Hz	0.5	180	135	3.43	13.9	28.5	89.6	2.5
	1	718	489	13.7	55.4	114	306	2.8
	1.5	1386	1030	30.8	125	257	618	3

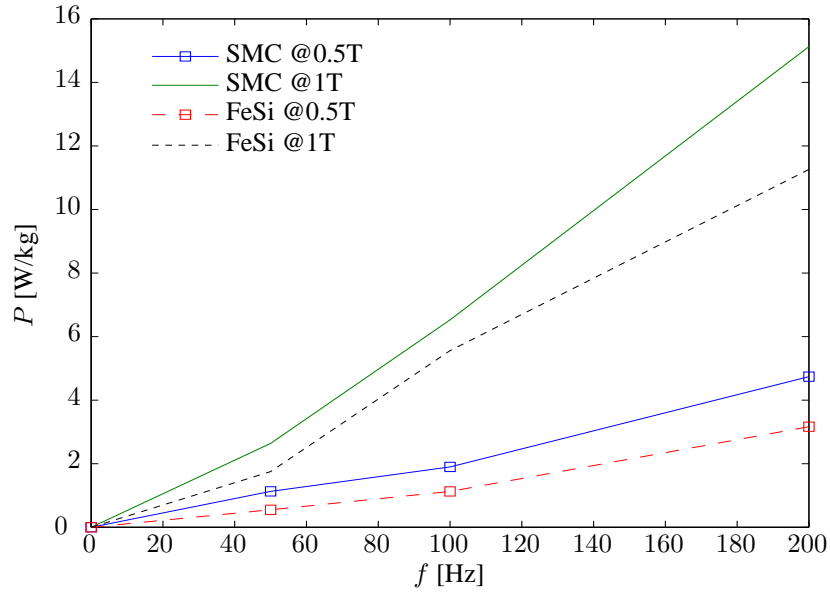


Figure 4.7: Losses for Somaloy Prototyp SMC and GO silicon steel on the AFPMSM setup at 0.5 T and 1 T.

The highest increase of total loss due to fringing flux is about 34%. This value is approximately 10 times higher than in section 4.3.2, because in section 4.3.2 only low excitation currents were applied to the excitation tooth coil in order to prevent saturation of the first few sheets closest to the excitation winding.

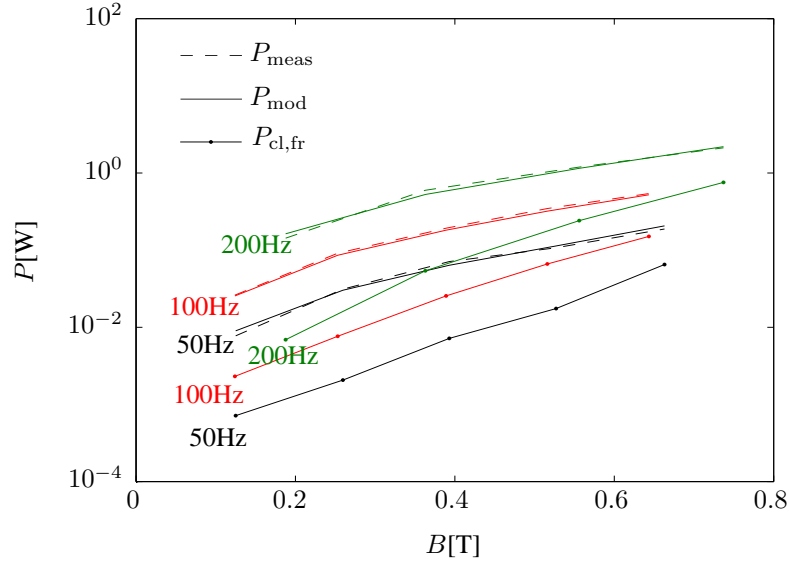


Figure 4.8: Total measured losses (P_{meas}), total modelled losses (P_{mod}) and losses due to fringing field ($P_{\text{cl,fr}}$) of the AFPMSM setup for LSSS at frequencies of 50, 100 and 200 Hz.

4.4 Detailed analysis of eddy currents in Laminated Silicon Steel Sheets

The first type of eddy currents – eddy currents due to the main flux – are resistance limited. The second type of eddy currents – the eddy currents caused by stray fields – are mostly limited by their own field and are said to be inductance limited. Knowing the latter effect, a phase shift in time between the two types of eddy currents is expected. For the calculation at a frequency of 333 Hz, it can be seen in figure 4.9 that at 1.57 ms, when the change in main flux is maximum, the classical eddy currents are dominant. It can be seen in figure 4.10 that later in time, at 1.72 ms, when the change in stray flux is maximum, that the eddy currents due to stray fields are dominant.

The fringing field causes a flux redistribution in the individual sheets due to saturation, which is shown in figure 4.11. This redistribution causes even more perpendicular flux falling in to the adjacent sheets, as shown in figure 4.12.

Figure 4.13 shows the simulated instantaneous eddy-current losses due to fringing flux in function of time in the individual top laminations for a calculation at a frequency of 200 Hz, with the sheet numbering starting from the top of the LSSS stack of figure 4.1-b. It can be seen in Figure 4.13 that there is a time shift between the peak values of the losses in the individual laminations, due to the shielding

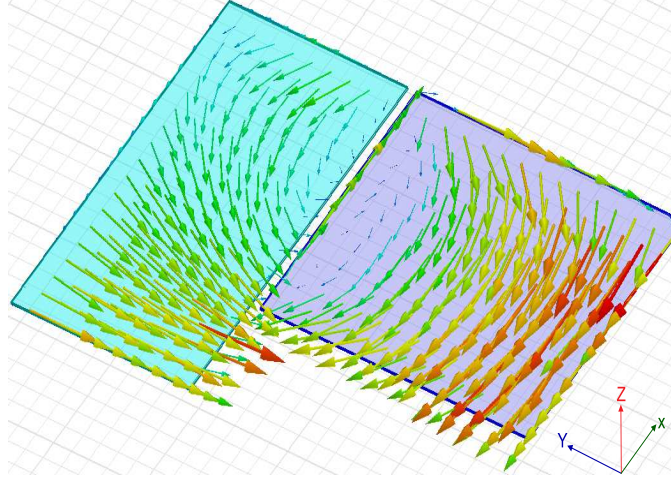


Figure 4.9: Induced eddy current field in top sheet of LSSS stack (see figure 4.1-b), at point 1.57 ms where the eddy currents due to the main flux are dominant.

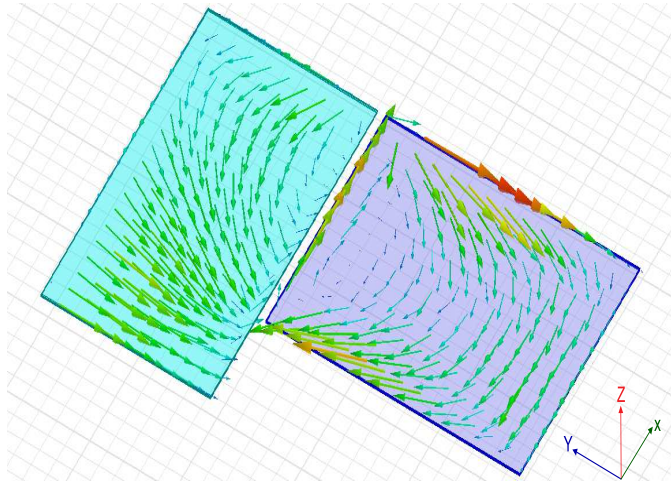


Figure 4.10: Induced eddy current field in top sheet of LSSS stack (see figure 4.1-b), at point 1.72 ms where the eddy currents due to stray fields are dominant.

effect of the individual sheets, which delays the penetrating fringing field in time. This shielding effect comes from the inductive behaviour of the laminations in the perpendicular direction. The decreasing edge of the instantaneous losses of the top lamination (lamination number 1 in figure 4.13) occurs earlier in time than the decreasing edge of the losses in the other laminations. This is due to magnetic saturation of the first lamination, causing a decrease of the inductance which causes

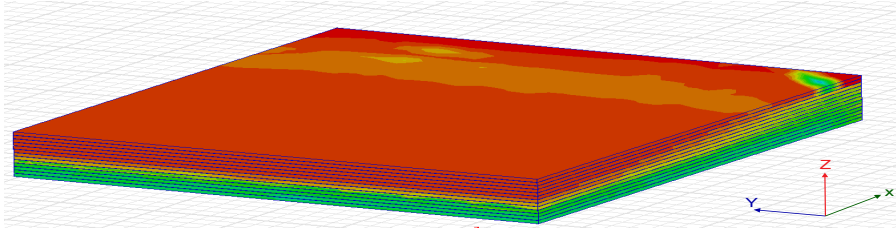


Figure 4.11: Magnetic flux density in the top sheets of figure 4.1-b, ranging from light green 0.7 T till red 2 T.

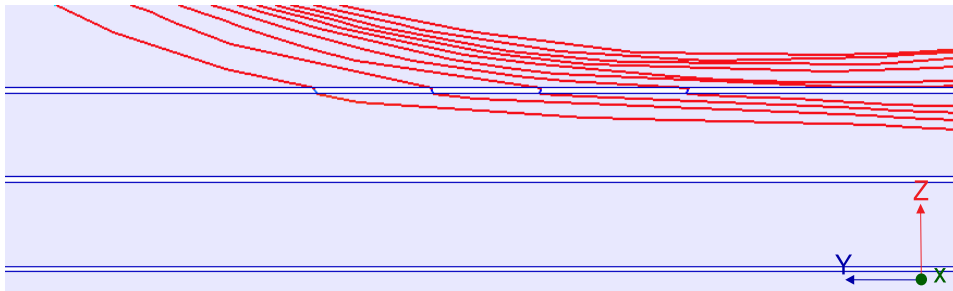


Figure 4.12: Fringing field lines in the outer sheets of figure 4.1-b.

the resistance of the first lamination to become dominant. Because of the saturation, the top lamination reaches its maximum of loss before the excitation current reaches its maximum: at 5.35 ms compared to 6.25 ms for the maximum of the current. The losses in the second lamination are higher, because of flux migration from the first lamination to the second lamination (as shown in figure 4.12), as a consequence of the saturation of the first lamination.

4.5 Fringing flux losses as function of flux density

Figure 4.14 shows the simulated eddy-current losses due to fringing flux in function of the averaged magnetic flux density level in the stator tooth, simulated by the field solver described in section 2.3.6. In a purely linear problem with imposed sinusoidal flux density at constant frequency, the losses caused by induced currents are expected to be quadratic with the flux density level. However, the figure shows that for the considered non-linear problem, the losses increase less than quadratically, even for low flux densities. Looking at the losses per individual sheet in 4.13, it is clear that – in spite of the simple geometry of this setup – complex nonlinear

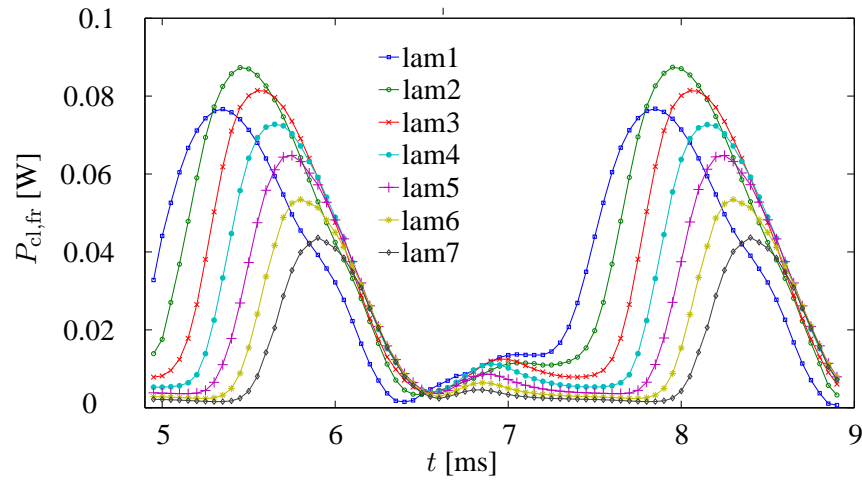


Figure 4.13: Instantaneous simulated losses due to stray fields in function of time in the individual top sheets. The sheet numbering starts from the top of the LSSS stack. The frequency is 200 Hz and the excitation is 1000 At. The average magnetic flux density level in the LSSS stack is 0.33 T.

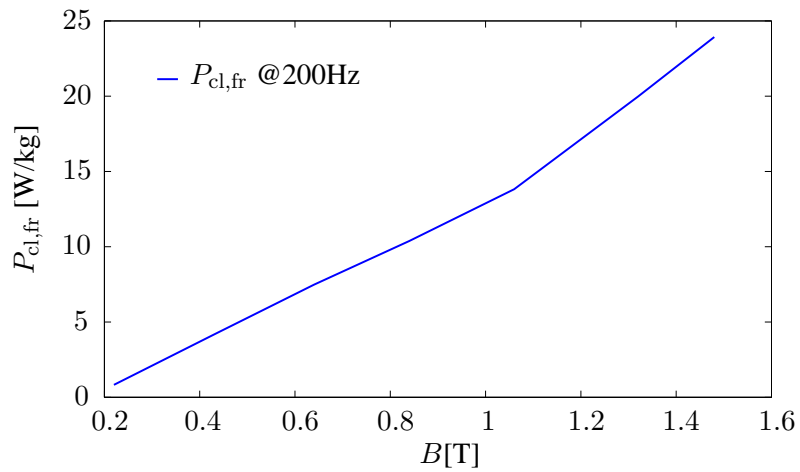


Figure 4.14: Simulated additional in plane eddy-current losses caused by fringing flux in function of the magnetic flux density level at a frequency of 200 Hz.

field patterns and loss distributions occur. Even for low average flux densities in the stack, the top laminations saturate (figure 4.11), so that the problem does not become linear even for rather low flux density values.

In order to validate the FEM simulations, the induced voltages due to fringing

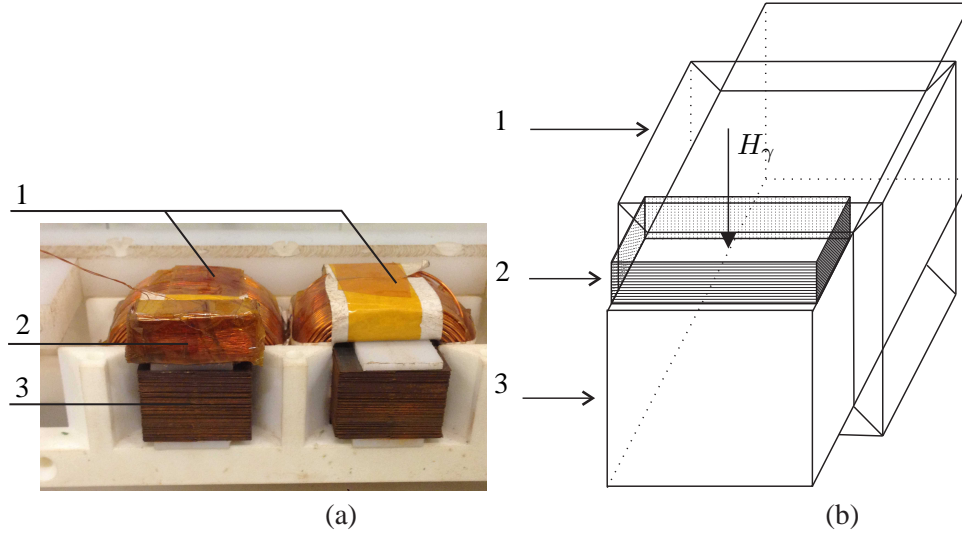


Figure 4.15: (a) Dedicated setup and (b) Detailed representation of the setup with 1) Excitations coils, 2) search coil, 3) LSSS stack.

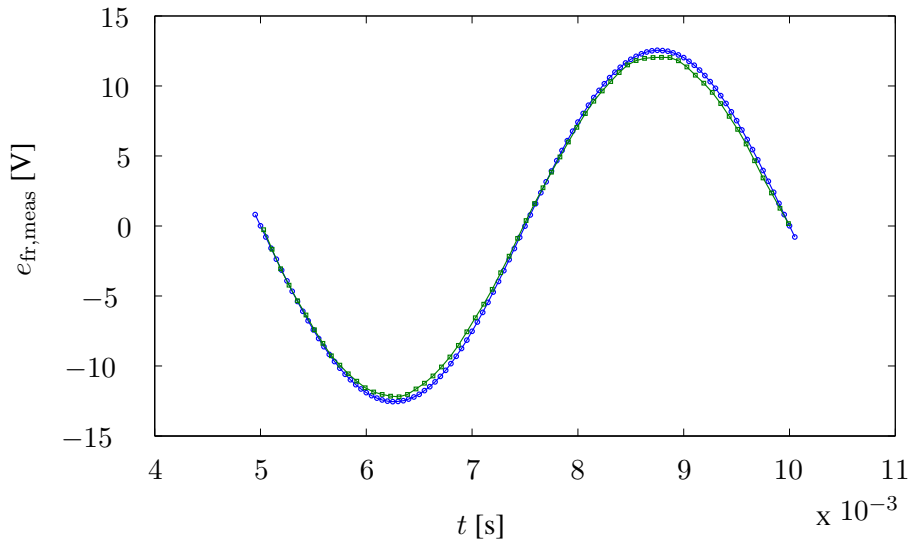
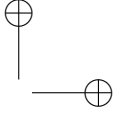
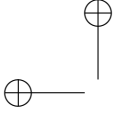


Figure 4.16: Measured and simulated induced voltage due to fringing flux in the search coil of figure 4.15 at a frequency of 200 Hz and an excitation of 1000 At.

flux are measured with a search coil of 100 turns, positioned as shown in figure 4.15. The search coil is constructed by revolving wires around a polyamide block with parameters of table 4.3. These dimensions fit perfectly between the back iron

**Table 4.3:** Parameters of the fringing flux search coil

Parameter	Value
Wire diameter	0.2 mm
Length	27.9 mm
Height	10.6 mm
Width	11.8 mm

and the excitation winding. This makes an easy positioning on top of the LSSS stack possible, as can be seen in figure 4.15.

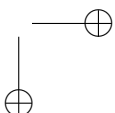
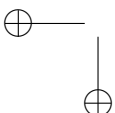
Figure 4.16 shows the measured and simulated induced voltage due to fringing flux in the search coil in function of time. Thanks to the accurate positioning and the accurate geometry of the search coil, it is seen that the measured and simulated waveforms correspond well. In chapter 5, where the complete and rotating axial flux machine is considered, also measurements and simulations are done for the induced voltage in a search coil for fringing flux. Because of much more uncertainty on the exact airgap size and the exact dimensions of the search coil, the correspondence of the waveforms is less good. This illustrates the usefulness of the simplified setup studied here in chapter 4.

4.6 Techniques for reducing fringing flux loss from armature reaction

Three novel methods are discussed and experimentally evaluated. The first method restricts the eddy currents directly by decreasing the enclosed surface area by segmentation. The second method deflects the fringing flux by adding SMC tooth tips. The third method short-circuits the fringing flux by adding ferromagnetic wires. The three approaches are studied theoretically and are compared in a new experimental setup. Figure 4.17 illustrates the three techniques graphically. The loss properties of the LSSS, SMC and ferromagnetic silicon-steel (FeSi) used for the wires are given in chapter 3

4.6.1 Top & bottom laminations segmented along axial direction

The largest eddy-current losses due to fringing fields take place in the first few sheets close to the excitation winding. Therefore, it is advantageous to limit the in-plane eddy currents in these first few sheets. A simple method, without destroying the material properties for the main magnetic field, is cutting the top and bottom sheets along the axial direction, as shown in figure 4.17-(a). In this way, the surface for the eddy currents due to fringing flux is significantly reduced. The number of



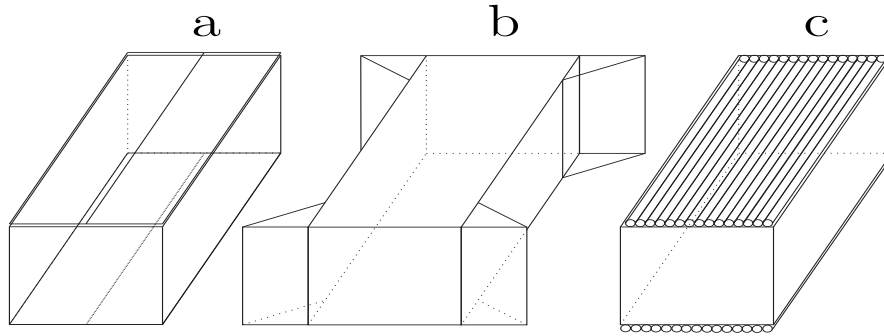


Figure 4.17: (a) Segmented top and bottom lamination (b) SMC tooth tips (c) top and bottom layer of adjacent ferromagnetic wires along the axial direction.

segmented top and bottom sheets and the number of divisions are two parameters to be determined. The number of split top sheets depends on the penetration depth of the fringing field. The number of divisions of the split laminations is restricted by construction constraints. Too many divisions will eventually destroy the material properties for the main magnetic field and will be too difficult to assemble. For this reason only a feasible number of divisions is applied. First only the top and bottom lamination were divided in two divisions each for a simulation of 200 Hz, because the penetration depth (according to equation 2.3) for M100-23P with an electrical conductivity of 1.67 S/m at a frequency of 200 Hz and calculated with a relative permeability of 10000 in the rolling direction for a flux density level of 1.8 T (as shown in figure 3.3) is only 0.275 mm. This penetration depth is the penetration depth for a half-plane model and is only valid as long as a homogeneous magnetic flux density is exerted to the lamination sheet. As will be seen is the penetration depth of the fringing field larger. Besides this, it will be seen that splitting the top and bottom lamination, causes an increasing penetration depth of the fringing field perpendicularly into the laminated stack. For this reason, three top and bottom laminations were divided into two divisions each.

4.6.2 SMC tooth tips for capturing fringing flux

Tooth tips are mainly used to reduce the higher-harmonic content of the airgap magnetic field in order to reduce torque ripple and cogging torque [60]. Because SMC blocks do not exhibit large eddy currents regardless of the direction of the flux density vector, it is advantageous to deviate the fringing flux by SMC tooth tips, as shown in figure 4.17-(b). The captured fringing flux will flow further in the laminations in the in-plane direction, without introducing extra eddy currents due to fringing flux.

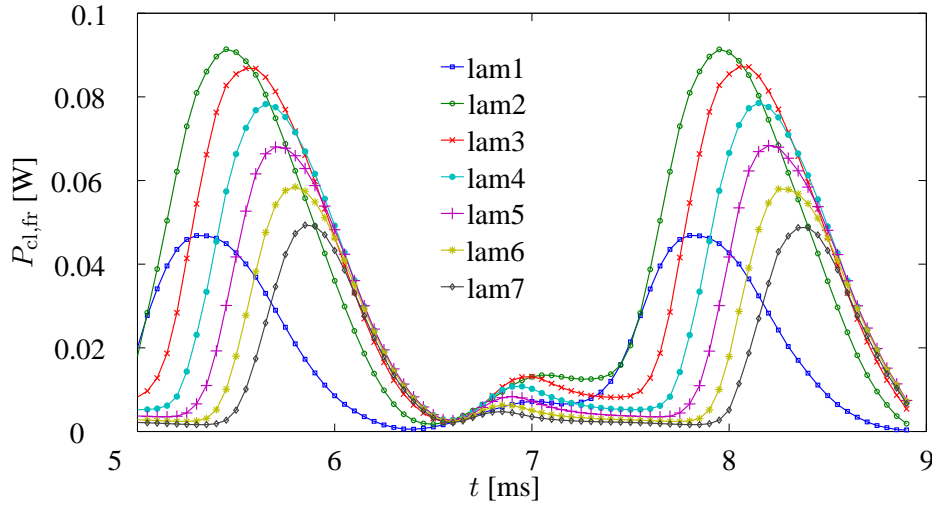


Figure 4.18: Instantaneous simulated losses due to stray fields in function of time in the individual top sheets, with *one segmented top sheet*. The sheet numbering starts from the top of the LSSS stack. The frequency is 200 Hz and the excitation is 1000 At.

Using SMC tooth tips may also be beneficial from constructional point of view, for the cutting of the laminations: all sheets remain rectangular and can be cut easily on a plate shear. However, the assembly of the laminated stack and the SMC tooth tips may be a disadvantage from constructional point of view.

4.6.3 Ferromagnetic wires as closing path for the fringing flux

Adding a layer of ferromagnetic wires, all oriented in the axial direction adjacent to the top and bottom of a LSSS stack, will short-circuit the fringing flux, as shown in figure 4.17-(c). In this way, the fringing flux is no longer perpendicular to the laminations.

4.7 Performance of the three proposed loss reduction techniques

The performance of the three proposed loss prevention measures is studied on the basis of the finite-element model and on the basis of the experimental setup. The major tendencies are described in the following three subsections.

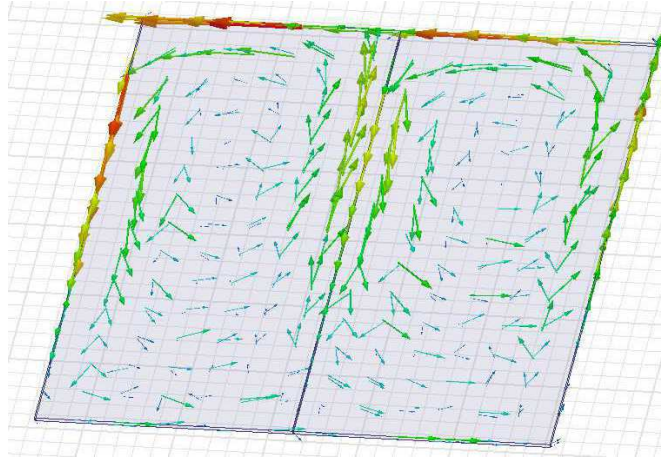


Figure 4.19: Eddy current density distribution in the top segmented lamination at a frequency of 200 Hz and an excitation of 1000 At.

4.7.1 Top & bottom laminations segmented along axial direction

To explain the effect of segmented laminations, we compare the simulated instantaneous losses in the laminations for the unsegmented case (figure 4.13) with the case with the first lamination segmented (figure 4.18) (the other laminations remain unsegmented). For the segmented case, it can be seen that the simulated eddy currents are lower in the segmented top lamination (lamination number 1 in figure 4.18): the peak value is about 45mW compared to 78mW in the unsegmented case (figure 4.13). However, the loss is higher in the other laminations, for example in laminations 2 and 3, we observe 92mW and 85mW versus 87mW and 81mW in the unsegmented case. For this reason, the eddy-current losses are higher in total compared with the standard case (without segmented top and bottom lamination). This is caused by the shielding effect of the first lamination in the unsegmented situation. By segmenting the first lamination, the reaction field of the eddy currents due to fringing flux in this segmented lamination will be lower.

Figure 4.19 shows the eddy current distribution in the segmented top lamination of figure 4.18 (lamination number 1). It is seen that the segmentation causes two eddy current loops, instead of one in the unsegmented case: see figure 4.10.

Figure 4.20 shows the instantaneous iron losses for three segmented top laminations. The losses evidently decrease in the first three laminations. In this case, the total fringing flux losses decrease with 17%. Knowing that the amount of fringing flux losses is 34% of the total iron losses, this gives a reduction of almost 6% in total iron losses.

The measurement results of figure 4.21 confirm this reduction of 6%, predicted by 3D FEM simulations, in case of three segmented laminations. Also the slight

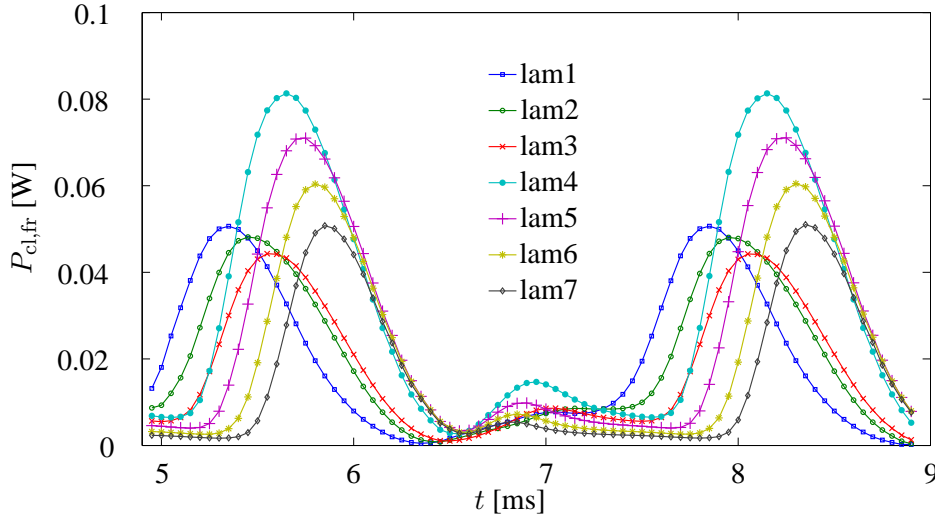


Figure 4.20: Instantaneous simulated losses due to stray fields in function of time in the individual top sheets, with *three segmented top sheets*. The sheet numbering starts from the top of the LSSS stack. The frequency is 200 Hz and the excitation is 1000 At.

increase of losses in case of only one segmented lamination can be seen in the measurement results.

For the technique of segmenting top and bottom laminations, we obtain the important conclusion that the total iron losses are reduced by about 6%.

4.7.2 SMC tooth tips for capturing fringing flux

Figure 4.22 shows the SMC tooth tips positioned using a polyamide holder. Figure 4.23 shows the total measured losses for the standard setup and the setup with SMC tooth tips. As the tooth tips change the inductance of the circuit, it is important to know that at a given abscis value in the figure, the total flux through the teeth is the same in the case with and the case without tooth tips. It can be seen that the losses are higher for low frequencies and low magnetic flux density values and lower for high frequencies and high magnetic flux density values when using SMC tooth tips. This is expected because for low magnetic flux density and low frequencies, hysteresis losses are dominant, and these are quite high in SMC. For high frequencies and high magnetic flux density values, the classical losses are dominant, but for SMC these latter losses are quite small.

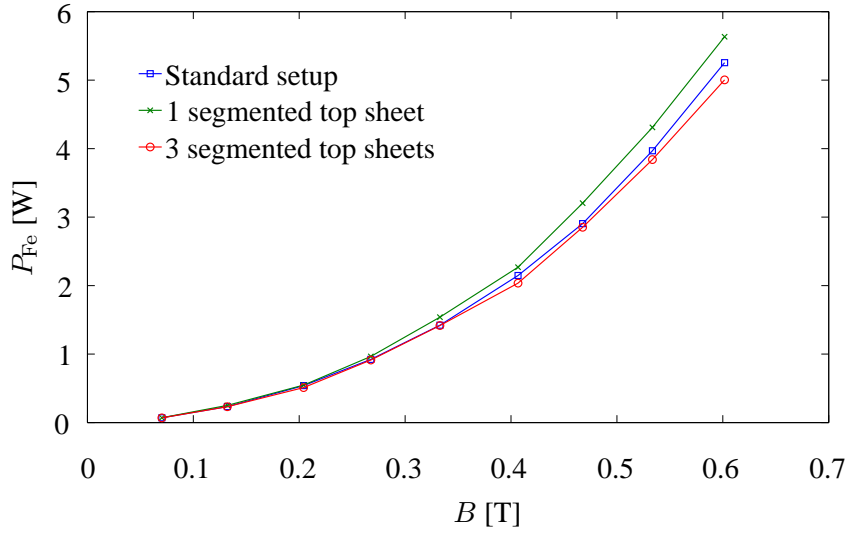


Figure 4.21: Total measured iron losses P_{Fe} for the standard stack, for the stack with one segmented sheet and for the stack with three segmented sheets. The frequency is 200 Hz.

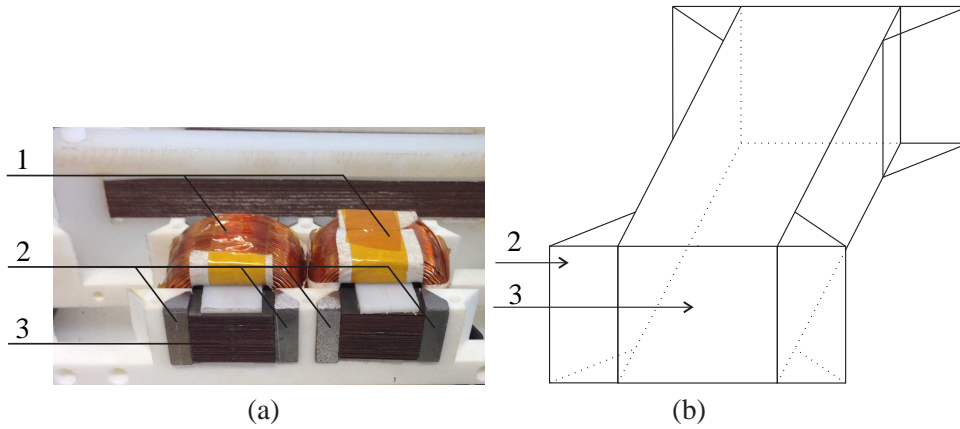


Figure 4.22: (a) Dedicated setup with tooth tips and (b) Detailed representation of the setup with 1) excitation coils, 2) SMC tooth tips and 3) laminated stack.

4.7.3 Ferromagnetic wires as a closing path for the fringing flux

One layer of eighty adjacent axially oriented ferromagnetic wires of 0.35 mm are placed at the top and bottom of the LSSS stack, as shown in figure 4.24. This layer is constructed by making a coil around a mold followed by removing the endings of the constructed coil. Figure 4.25 shows the total measured losses by use of this

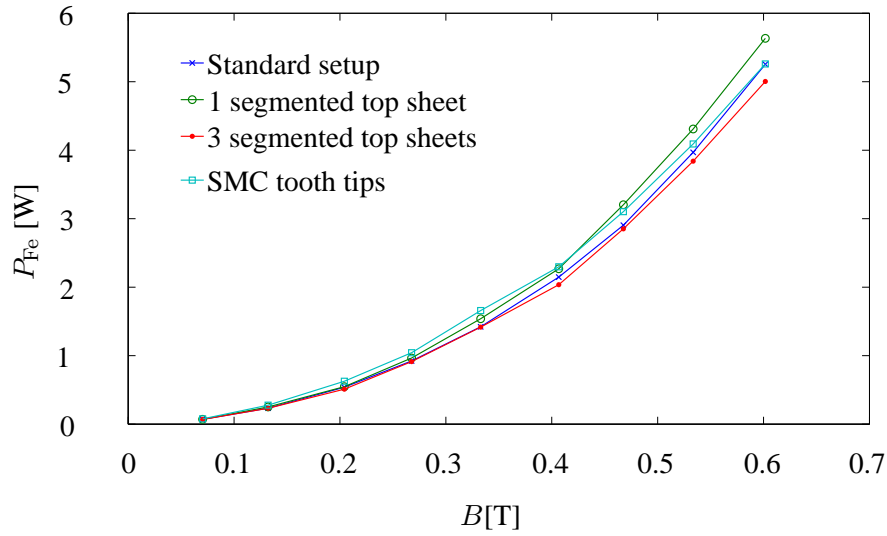


Figure 4.23: Total measured iron losses for the standard LSSS, a LSSS with one segmented top and bottom sheet, a LSSS with three segmented top and bottom sheets and a LSSS with SMC tooth tips. The frequency is 200 Hz.

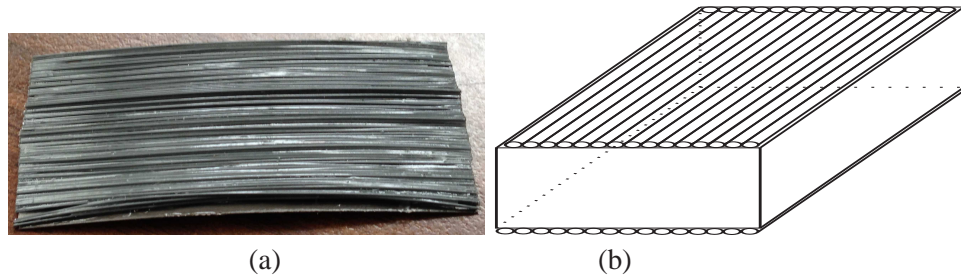


Figure 4.24: (a) One layer of adjacent FeSi wires (b) One layer placed at the top and bottom of the LSSS

layer. It can be seen that the losses are always higher when using a ferromagnetic layer. This is due to the large difference in permeability between the ferromagnetic wire and the LSSS and also because the losses of the wire in W/kg are much higher than the losses of the grain oriented silicon steel sheets: see figures 3.17 and 3.18. Fringing flux migration takes place and these flux lines are perpendicularly to the plane of the sheet.

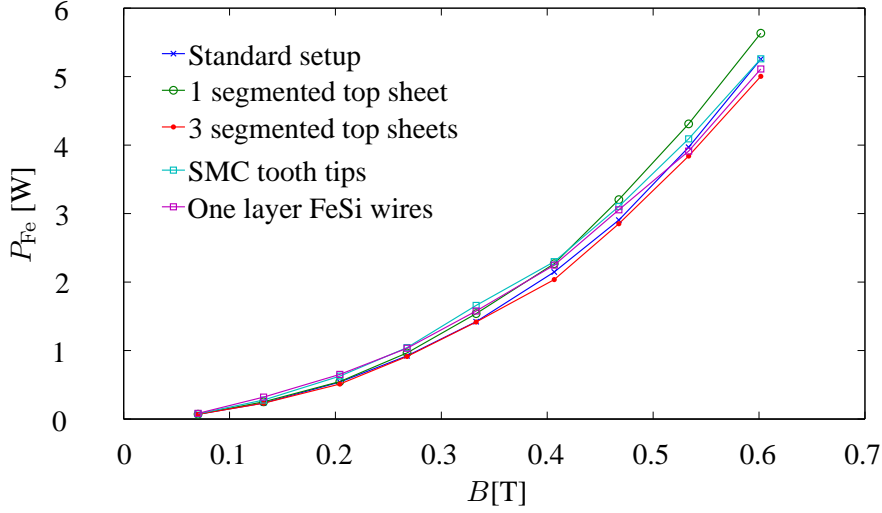


Figure 4.25: Total measured iron losses for the standard LSSS, a LSSS with one segmented top and bottom sheet, a LSSS with three segmented top and bottom sheets, a LSSS with SMC tooth tips and a LSSS with one top and bottom layer of adjacent axial oriented ferromagnetic wires. The frequency is 200 Hz.

4.8 Conclusion

A simplified non-rotating experimental setup of the AFPMSM is presented, which makes it possible to measure iron losses very accurately. This simplified non-rotating setup consists of motor teeth, each excited by a tooth coil and a return yoke.

The field models of chapter 2 are compared with each other and validated on the simplified experimental non-rotating setup. The magnetic characterisation from chapter 3 is included in the modelling.

On this simplified non-rotating setup, a detailed study is done of the losses caused by fringing flux coming from the armature reaction. The losses are validated on the simplified non-rotating setup. The validated field simulations give a very good idea of the origin and the behaviour of fringing flux losses coming from the armature reaction.

In the last part of this chapter, three approaches for reducing these losses are discussed. The first method directly restricts the eddy-current losses by segmenting the lamination surface. The second method deflects the fringing flux by using Soft Magnetic Composite (SMC). The third method magnetically short-circuits the fringing flux using ferromagnetic wires. The technique using segmented top and bottom laminations obtained the best result in reducing iron losses due to fringing flux.



Chapter 5

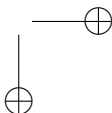
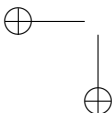
Fringing flux loss in the complete Axial Flux Permanent Magnet Synchronous Machine

5.1 Introduction

Chapter 1 has given an overview on the operating principle of the Yokeless and Segmented Armature Axial flux machine. As explained in that chapter, this machine is known to have a high efficiency and a high power density [7]. Before the start of this PhD, the geometry and electromagnetic properties of the machine were already optimized in a “conventional” way, considering iron losses, copper losses and magnet losses. This was done by several research groups e.g. prof. McCulloch and dr. Woolmer at the University of Oxford (UK) [14], prof. Di Gerlando at Politecnico di Milano in (Italy) [21], prof. Pyrhönen and dr. Parvainen at Lappeenranta University of Technology (Finland) [61], and also at Ghent University, EELAB [7]. In this PhD, the goal is not to redo this optimization. The research goal is to further improve the efficiency of the existing machine by having a deep focus on the loss components, in particular the fringing flux losses. We first give an overview of the conventional iron and copper losses of the machine, and then study the fringing flux losses in detail. The full understanding of the effects of fringing flux in YASA machines makes it possible in the future to further increase the efficiency of this type of machines.

According to literature, the fringing flux caused by the permanent magnets on the rotor or the end windings on the stator can increase the losses in electrical machines, especially if the stack length is rather short compared to the airgap width and the end winding size [62]. Fringing fluxes have been studied in several papers, mainly for radial flux machines.

In [63], the 3-D finite-element analysis (FEA) shows the excessive end core and radial-flux fringing effects in the axial-flux configuration of a switched reluctance



motor. The paper presents geometry modifications to reduce the radial fringing flux because it reduces the torque of the machine (higher flux in the unaligned position). Notice that the goal of this paper is not to increase the efficiency, but to increase the torque of the machine.

In [62], the fringing flux was investigated for linear induction motors. As expected, the authors found that the fringing flux increases the magnetization inductance and that it becomes more significant when the airgap becomes larger. Interesting parametrized studies were done, showing the quantitative influence of airgap width, stator width and end portion width on the thrust force of the linear motor and on its circuit parameters.

The effect of end windings is studied also for synchronous machines, in [64] for large 150MW turbo-generators. Similar to the above cited papers, a 3D FEM analysis was done. The main concern of this paper is the induction of eddy currents in metal components in the end region, which leads to heat generation. The use of copper and magnetic screens was studied in order to reduce the total eddy-current losses of end metal structures.

In [65] the in-plane eddy currents were analysed for end and interior stator core packets of turbine generators (the stator core of turbine generators is divided into packets in order to provide duct-space). A 3D FEM analysis was done considering each lamination by the 3D finite elements, in order to calculate the in-plane eddy currents accurately. The authors found that the in-plane eddy current density was not only large in the laminations of the end stator core packets but also in the top lamination of interior core packets. It was found that the maximum current density in the top lamination of the interior core packet was comparable with the current densities in the laminations of the end stator core packets.

The paper [66] analyses the behaviour of the radial and axial flux density components and the corresponding eddy currents inside the laminated cores of a large-sized squirrel-cage induction motor. The 3D model is shown in figure 5.1(a). For comparing the eddy-current losses in the core ends at different axial depths conveniently, the active region was divided into forty 10-mm-thick slices perpendicular to the rotor shaft. Only a no-load situation was considered. The axial flux density component, caused mainly by the airgap fringing flux and the end-winding leakage flux, appears in the end portion of the cores, and decays rapidly towards the middle of the cores. The decay occurs roughly by a factor 3 in subsequent laminations towards the middle of the stack. The authors have studied not only the decay of the amplitude, but also the phase lagging of this axial flux density component, which is shown in figure 5.1(b) for the 10 outermost slices at the tip of a stator tooth. The phase shift indicates that the axial flux penetrates the laminated stack like in a diffusion problem, causing phase delay from the stack end (slice 40) towards the machine centre (slice 1). This phenomenon was not observed in the rotor: there were almost no eddy currents in the rotor as the authors considered only no-load (slip zero). The radial component of the flux density had a rather limited decay (20%) from the stack end towards the centre of the stack, but this compo-

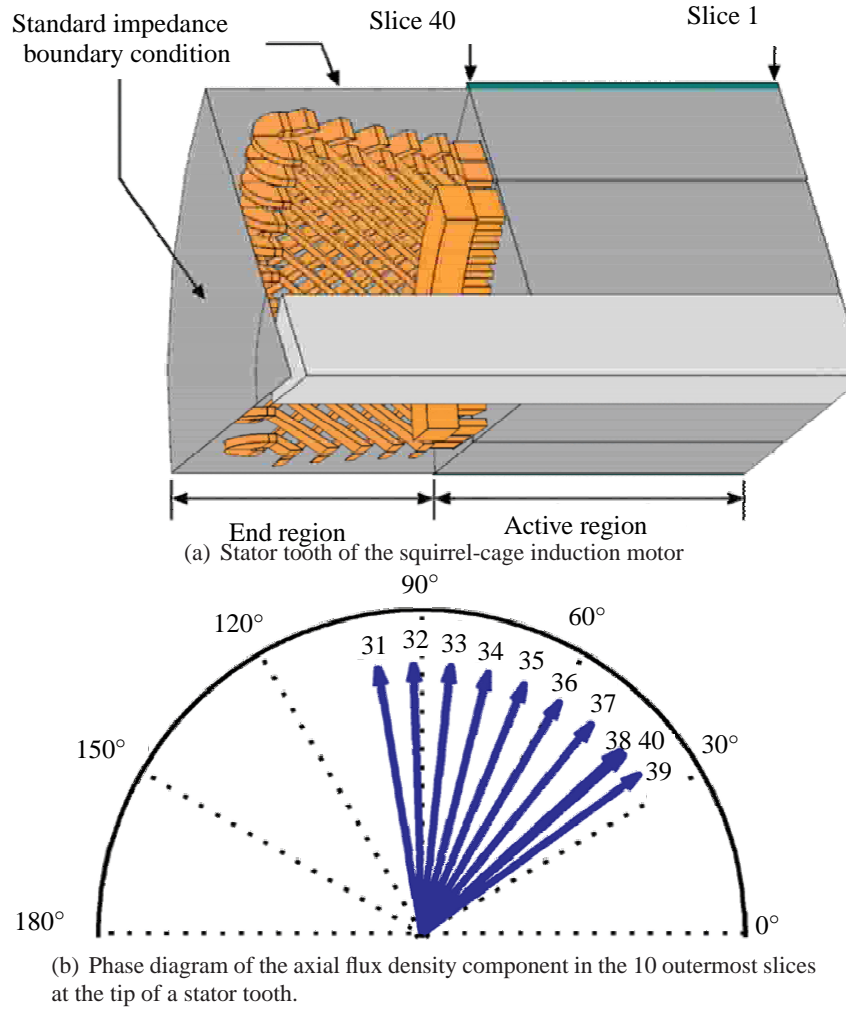


Figure 5.1: a) The 3D model of the squirrel-cage induction motor of paper [66], b) phase angles of the axial flux density component in the 10 outermost slices at the tip of a stator tooth.

nent showed almost no phase shift. The eddy-current losses were found to be small (about 43 W in the stator core for a 1.25 MW machine, compared to 306 W no load copper losses of the stator phase winding), but the authors only considered no-load, and the axial length of the machine is very large compared to the airgap length.

For YASA machines, the phase shift of the field perpendicular to the laminations was studied in chapter 4 and [67] for the simplified setup of the YASA axial flux machine. Similar conclusions were found. The eddy currents caused by the

main flux – the flux in the plane of the lamination – are resistance limited and have about 90 degrees phase shift with the flux. The eddy currents caused by fringing flux – flux perpendicular to the lamination plane – behave as in a diffusion problem: the phase shift is larger – between 90 and 180 degrees – and skin effect is observed for this flux: the amplitude of the flux decays in azimuthal direction, from the edges towards the middle of the laminations.

The YASA machine considered in this PhD has a stack length – which is in radial direction – that is usually rather short in comparison to radial flux machines of the same size and power. For axial flux machines, almost no literature can be found on fringing fluxes and their effect on losses. Moreover, an additional problem occurs in axial flux PM machines compared to radial flux PM machines. The problem occurs if the rotor magnets are rectangular or trapezoidal, which is often the case. When the magnet passes a stator tooth, the edges of the magnet protrude in radial direction, causing larger fringing flux as shown further in this chapter. This chapter presents a study of the losses caused by fringing flux as a function of several parameters such as rotational speed and airgap size. In addition, in contrast to several cited papers that consider no-load only, the influence of the stator current is investigated. In the last sections of the chapter, we consider first the no-load situation. Here, the fringing flux losses are caused only by the rotating permanent magnets. Then, full load is considered. At full load, the stator currents cause additional fringing fluxes. Finally, the effect of speed and airgap thickness is explained.

5.2 The machine under study

5.2.1 The considered YASA machine

The design of a 4 kW YASA machine as well as the study of the different loss terms have been studied by several researchers at the laboratory EELAB and have been published in a number of papers. The design and study were done as a function of several geometrical parameters, for several magnetic materials, for several current waveforms and at different operating speeds.

All studies have been done for the same YASA machine, initially introduced in [68]: a machine of 150 mm outer diameter, 15 stator slots and 16 rotor poles. The machine has a rated power of 4 kW and a rated speed of 2500 RPM. The main specifications are given in Table 5.1, and further details of this machine are explained later in this chapter. Also in this PhD, the same YASA machine is considered, so that e.g. values of losses found in earlier studies can be numerically compared to new studies in this PhD.

The following sections give an overview of the studies done on this machine: the global design and the study of loss components. The goal of the overview is not to give a detailed report of these studies, which are available in the scientific literature. The goal of the following sections is to give an idea of the order of

Table 5.1: Axial flux PM machine prototype specifications.

Parameter	Value	Unit
Rated mechanical output power	4000	W
Rated speed	2500	RPM
Rated torque	15	Nm
Rated current	10	A
Pole number	16	-
Slot/tooth number	15	-
Outer diameter housing	195	mm
Outer diameter (active)	148	mm
Inner diameter (active)	100	mm
Axial length stator	61	mm
Total mass	9	kg
Magnet thickness	4	mm
Magnet segments width	18/21/24	mm
Magnets	NdFeB 40SH	-
Stator core material	M100-23P	-
Rotor back iron thickness	8	mm
Airgap length (adjustable)	1.0 – 5.0	mm
Slot width	11	mm
Slot opening	3	mm

magnitude of the different loss components in the considered machine, so that a later comparison with fringing flux losses is more useful.

5.2.2 Global design of the machine for high efficiency

In [68], the efficiency optimization of the YASA machine was done, by using the multislice 2D technique of section 2.3.4. Also the influence of mass on the optimal values of the geometry parameters and the efficiency is considered. It was found that the mass can be reduced significantly with only a small decrease of efficiency. Furthermore, in [69], two types of silicon steel were compared to study their influence on the efficiency: non-oriented and grain oriented steels. The work about optimization, published by Dr. H. Vansompel, and the work about the comparison of magnetic materials, published by Dr. D. Kowal, were the oldest published work on the YASA machine in the research group EELAB. These publications were the basis for later, more detailed research on losses. In the optimization, it was already noticed that some parameters have a contrary effect on the different losses in the machine. For example, a high axial length of the stator cores combined with large slot openings is beneficial with respect to the copper losses, but it results in higher stator core losses. The work considered rather conventional loss modelling, but it was important to optimize the geometry of the machine towards high efficiency

and power density.

5.3 Loss analysis in the YASA machine

In this section, the several loss terms of the YASA machine are investigated in detail: iron losses, copper losses, permanent magnet losses, bearing loss and windage losses. Evidently, these losses depend on the geometry, the electromagnetic properties (magnetic materials), the sources (stator currents, permanent magnets), as well as on the rotation speed. The following sections give an overview of work that is not done in the framework of this PhD, but that is published in the literature by the research group EELAB.

5.3.1 Stator core losses

Non-oriented versus grain oriented magnetic material

The possibility to use grain oriented material is an important advantage of the YASA machine. This material is not much more expensive than conventional non-oriented magnetic material, but it has two advantages: 1) it has a higher flux density at typical magnetic field levels in machines, and 2) it has much lower losses in the rolling direction: as low as 1.0 W/kg is possible at 1.7 T and 50 Hz, while conventional non-oriented steel with the same thickness has usually at least 2.3 W/kg at an even lower flux density of 1.5 T and at the same 50 Hz frequency.

The comparison of oriented and non-oriented (M700-50A) material, published by D. Kowal [69], was carried out for the described 4 kW YASA machine. The hysteresis loops were measured – see figure 5.2 – showing both the higher flux density (about 1.8T instead of 1.5T at 2000A/m) and the lower losses (smaller enclosed surface of the hysteresis loop) of the grain oriented material. In the paper [69], the losses were studied as a function of the frequency: figure 5.3. This figure gives a quantitative impression of the iron losses in the considered machine, as a function of speed. With the grain oriented material, the YASA machine has only about 1/5 of the iron losses of non-oriented material at the same speed: for example at a speed of 2000 RPM, it is seen that the expected iron losses are about 30W for the grain oriented material and 150W for the non-oriented material. In addition, a 10% higher torque is obtained for the same current. Also, when extrapolating to the rated speed of 2500 RPM in a quadratic way (worst case), the expected iron losses are about 47W.

Influence of the slot openings on the stator core losses

The effect of geometrical parameters on the stator core losses are illustrated in [30]. Here, the influence of the stator slot openings is investigated. This is an important study because it has a link with the study of iron losses on the simplified setup of

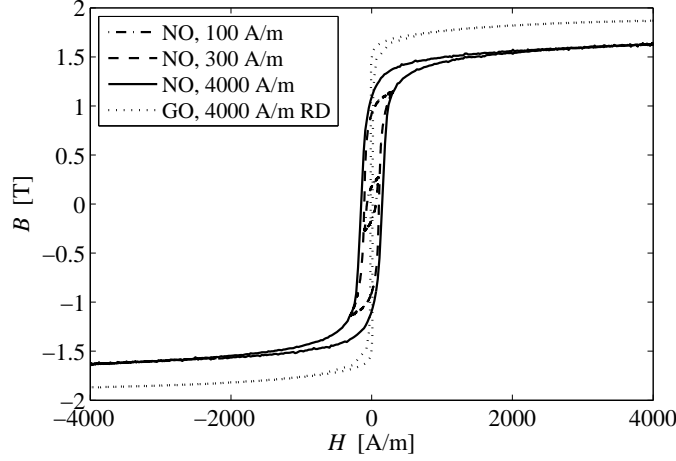


Figure 5.2: Measured hysteresis loops for non-oriented (NO) and grain oriented (GO) material [69]

the axial flux machine, as explained in chapter 4. In chapter 4, a comparison was made between on the one hand a stack of rectangular silicon steel sheets and on the other hand the same stack of rectangular silicon steel sheets with added SMC tooth tips for capturing fringing flux. The tooth tips also decrease the slot opening width. It was concluded that for low frequencies the total iron losses are higher in case of added SMC tooth tips because of the high hysteresis losses of SMC and that for high frequencies the total iron losses are lower in case of added SMC tooth tips because of the low classical losses of SMC.

The width of the stator slot openings near the airgap has a large influence on the losses in the stator iron and in the permanent magnets of concentrated winding machines such as the YASA machine. This was shown by V. Xuan [70], who investigated the influence of stator slotting on the performance of a radial flux permanent magnet machine. On the one hand, the increase in stator slot openings results in lower losses in the stator iron. On the other hand, it also results in increased losses in the permanent magnets. Also the torque is reduced for large (13 mm) but also for very small slot openings (1 mm).

To clearly illustrate the influence of the slot opening width b_0 , two values are chosen in all further examples: rather closed slots with $b_0 = 3$ mm and rather open slots with $b_0 = 9$ mm.

When considering only permanent magnet flux, an unequal distribution of the magnetic field over the tooth is observed in radial direction. Due to the shape of the permanent magnets, the magnetic flux density in the laminations near the inner radius is found to be higher than the one at the outer radius. This is caused by the variable tooth pitch as a function of the diameter combined with a constant

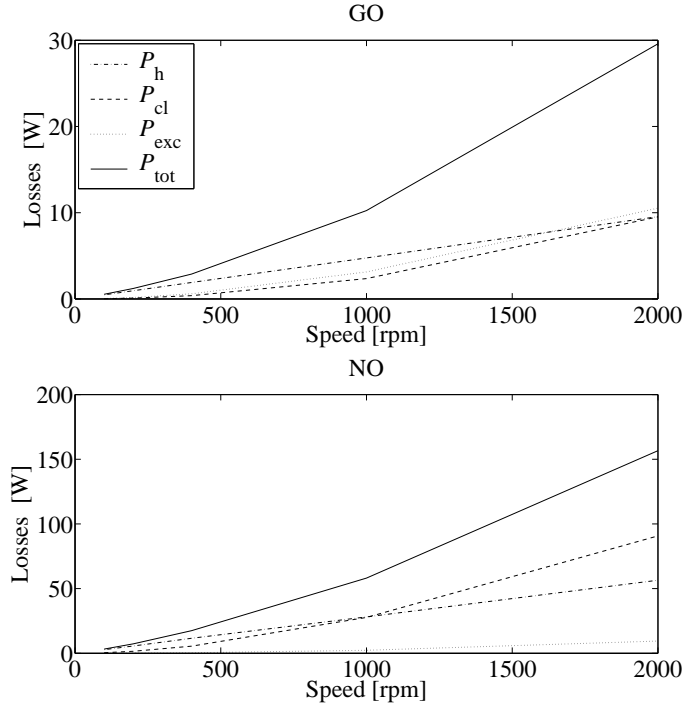


Figure 5.3: Iron losses in the stator for non-oriented and grain oriented material [69]

slot width. Flux leveling over the laminations by radial magnetic flux components, is limited due to the very poor permeability of the stator cores in the direction perpendicular to the lamination planes. The effect is further studied by 3D FEM in section 5.3.5. However, it can be seen also by 2D FEM presented in [30]: in Fig. 5.4 the magnetic flux density pattern in the stator core element is illustrated in case only permanent magnets were present and aligned with the stator core element in case of 3 mm slot opening width.

The influence of increasing the slot opening width from 3 to 9 mm is illustrated in Fig. 5.5. At the inner diameter lamination regions, the magnetic flux density in case of $b_0 = 9$ mm has decreased with an average value of 0.3 T compared to the case of $b_0 = 3$ mm as the smaller tooth tips catch less magnetic flux. With larger slot openings, the total magnetic flux in the stator core element reduces.

When considering only armature reaction current – that means that the remanent flux density of the permanent magnets is set to zero – higher magnetic flux densities are found at the inner diameter regions compared to the outer diameter regions. The magnetic flux density pattern is plotted in Fig. 5.6 for the 3 mm slot width opening and in Fig. 5.7 for 9 mm, both at rated current [30]. The increase

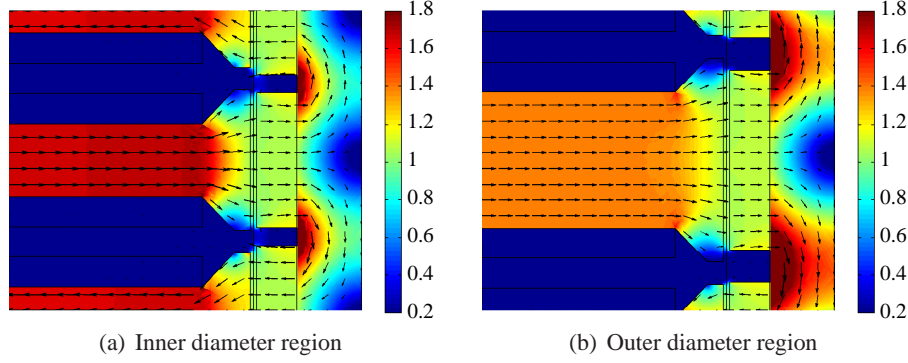


Figure 5.4: Magnetic flux density in tesla in the stator core when the permanent magnet is aligned with the stator core for the 3 mm stator slot openings width [30].

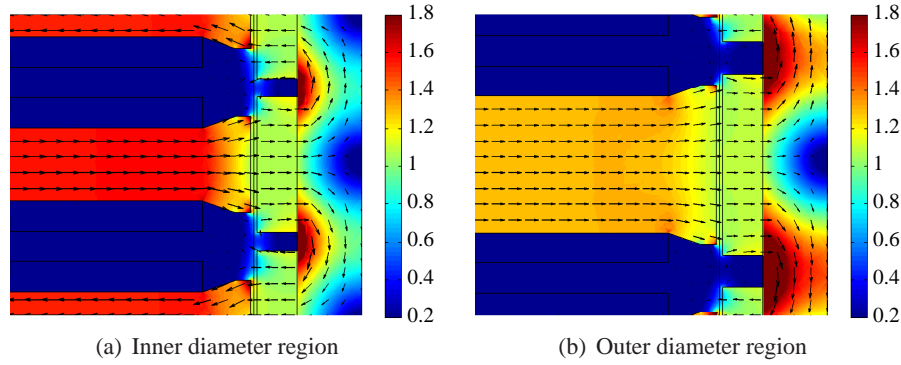


Figure 5.5: Magnetic flux density in Tesla in the stator core when the permanent magnet is aligned with the stator core for the 9 mm stator slot openings width [30].

of the slot openings increases the reluctance for the slot leakage flux, and hence reduces the magnetic flux density levels in the stator core elements. The reduction of the magnetic flux density is higher at the inner diameter regions compared to the outer diameter regions.

When combining permanent magnet flux with armature reaction flux, lower stator core losses are expected for the machine with the wide slot openings. This is indeed observed when evaluating the iron losses in the machine both at load and at no-load. Table 5.2 shows the results.

Analysis of Table 5.2 indicates that the stator core losses mostly exceed 100 W. Note that in this table a non-oriented material was used. Both for no load and load

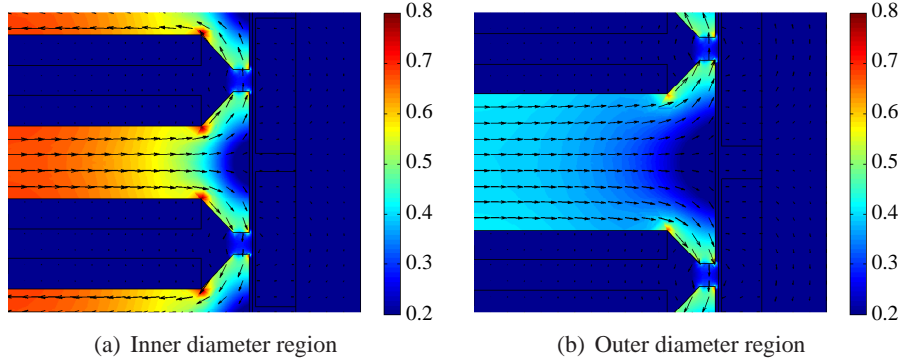


Figure 5.6: Magnetic flux density in Tesla in the stator core taking only armature reaction into account for the 3 mm stator slot openings width [30].

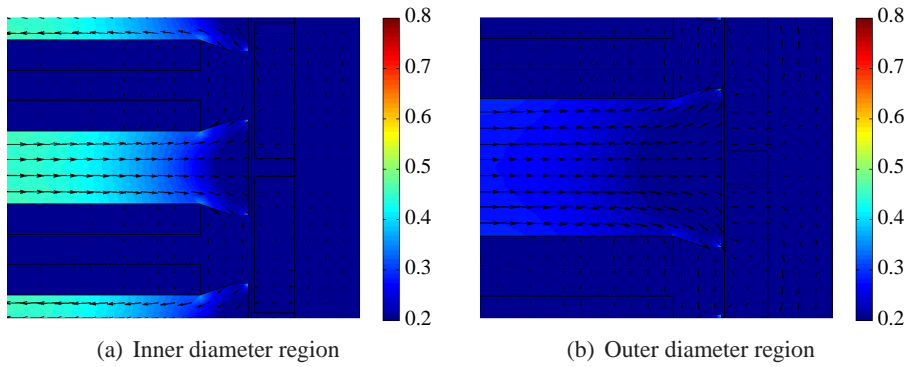


Figure 5.7: Magnetic flux density in Tesla in the stator core taking only armature reaction into account for the 9 mm stator slot openings width [30].

working conditions, the iron losses decrease as the stator slot openings become wider. The difference between the core losses with closed slots and open slots is large: almost 50% at rated load. Further in this PhD, a slot opening of 3 mm is considered, leading to stator core losses in rated conditions (2500 RPM, full load) of 135 W with non-oriented material (Table 5.2) and – by extrapolation of results in [69] – 47 W with grain oriented material.

5.3.2 Copper losses

For the same size, power and speed, the copper losses in YASA type machines – and in machines with concentrated windings (tooth coil windings) in general –

Table 5.2: Influence of the stator slot opening width on the losses, torque and power, at rated speed (2500 RPM), rated load current (7 A) and with 4 segments per magnet. The copper losses in the windings are estimated at 60.8 W. [30]

Stator slot openings width [mm]	Average torque [Nm]	Average power [kW]	Load losses			No load losses		
			Core [W]	PM [W]	Total [W]	Core [W]	PM [W]	Total [W]
1	18.22	4.769	148.0	5.446	214.3	124.4	0.1691	124.6
3	18.50	4.844	135.1	10.15	206.1	124.5	5.877	130.4
5	18.38	4.811	127.3	21.91	210.0	120.3	18.42	138.7
7	18.09	4.736	118.7	33.45	213.0	113.5	30.33	143.8
9	17.65	4.622	109.2	40.52	210.5	104.8	37.55	142.4
11	17.07	4.470	98.95	42.56	202.3	95.07	39.69	134.8

are typically lower than in machines with distributed windings. This is thanks to the short end windings and the resulting rather low resistance per phase [71]. The phase resistance can be reduced further by aiming at a high slot fill factor. For the considered YASA machine, the slot fill factor is about 0.5. The total copper losses at rated load are about 60 W. The section of the wire is chosen sufficiently small so that the AC resistance is not much higher than the DC resistance. It is observed that these losses are dominant at rated load and speed when using grain oriented magnetic material (iron losses are about 47 W), and that iron losses are dominant when using conventional silicon steel M700-50A: the iron losses are between 95 and 148 W according to Table 5.2.

The copper losses can be further reduced for the same power by introducing the combined star-delta winding. This technique increases the winding factor and by consequence the *emf* of the machine by about 3% for the considered machine with 16 poles and 15 stator slots [72]. As power is determined by the product of *emf* and current, it is clear that either the power increases by 3% for the same copper losses, or the copper losses can be reduced by about 6% for the same output power.

Finally, it is well known that reducing copper losses requires a low winding temperature. The copper resistance increases with temperature by a factor $(1 + \alpha_{Cu}\Delta T)$ with $\alpha_{Cu} = 0.004/\text{K}$. A good thermal management is crucial to keep the windings at an acceptable temperature at high load. Therefore, in [73], a coupled electromagnetic and thermal modelling technique is developed for the considered YASA machine and validated with measurements. It was found that the machine reaches a steady state temperature of about 70°C at 2500 RPM and at rated load. This is much lower than the allowable temperature of 155°C for enamelled wire class F, and results in 1/3 less copper resistance than at 155°C.

5.3.3 Eddy-current losses in the permanent magnets

Eddy currents in the permanent magnets of the YASA machine originate from changing flux density (dB/dt) in the magnets, causing induced voltages. The induced voltages in the electrically conductive NdFeB magnets lead to induced currents and eddy-current losses. The dB/dt has three possible causes:

- Reluctance effects caused by the stator slotting. This is the only term causing losses at no-load operation. It is absent in slotless machines.
- Space harmonics of the current. The mmf of the stator currents in the slots of the machine is a stepwise function along the circumference of the machine: each stator slot causes a step. The Fourier spectrum of this function has many harmonics, especially in fractional slot machines. Even if sinusoidal time waveforms of the currents are injected in these slots, the airgap flux density contains harmonics that rotate in a non-synchronous way. These harmonics cause eddy currents in the magnets.
- Time harmonics of the current. Additional harmonics are created if the time waveform of the current is not sinusoidal. When using Pulse Width Modulation (PWM), several harmonics are introduced. Also these harmonics result in eddy currents in the magnets.

The eddy-current losses in the permanent magnets are evaluated in different ways. A fast computation technique is based on the multislice 2D - 2D model, introduced by H. Vansompel in [7]. The study was done for the same YASA machine as the one described further in this PhD in section 5.2.1, and with properties given in Table 5.1. The losses in no-load depend on the rotational speed, the segmentation of the magnets, and the geometry of the stator teeth. At load, the losses also depend on the current distribution in space, and the current waveforms in time. The computational approach in the paper is fast, but only valid for rather low frequencies, where the eddy currents are “resistance limited”. As explained in chapter 4, this means that the induced currents in the magnets are too weak to influence the source field that creates them.

In Table 5.2, taken from [30], the magnet losses are shown for different stator slot opening widths, from 1 mm to 11 mm. The losses are computed with the multislice 2D - 2D model of [7]. In this table, the permanent magnets are assumed to consist of four electrically isolated segments. At load, evidently, the magnet losses are higher than at no-load. The values range from 5 W for almost closed stator slots to 43 W for almost open slots. The increase with the slot opening is mainly due to the first cause of eddy currents: the reluctance effects.

Segmenting the magnets is a known technique to reduce eddy-current losses. Table 5.3 shows the loss in the magnets for other segmentations in case of $b_0 = 3$ mm. It is seen that with sufficient segmentation (two rotors were made

Table 5.3: Effect of segmentation on the eddy-current losses in the magnets for 3 mm slot opening [30]

# segments	Magnet eddy-current losses [W]	
	no-load	rated load
1	8.14	15.42
2	6.61	11.76
4	5.88	10.15
14	2.89	4.09

with 16 magnets consisting of 14 segments), the magnet losses can be reduced to 4W at full load and speed, which is almost negligible compared to other losses.

Other methods for loss computation in the magnets of the same YASA machine were presented by A. Hemeida in [74]. This paper describes an analytical model for the eddy currents in the permanent magnets (PMs) in the YASA machine using a coupled solution of Maxwell's equations and a magnetic equivalent circuit (MEC). The method includes the effect of armature field and slots. The permanent magnets are modelled by a simple electric network, composed of resistances and inductances. The model can describe the reaction field effect of the eddy currents flowing in the magnets and also the skin effect. It is shown for many cases how big the error in the computed losses is if the reaction field is neglected, by comparing with a transient 3D FEM. The authors conclude that inclusion of the reaction field is necessary when the machine is excited by a Pulse Width Modulated (PWM) current, while for a sinusoidal excitation, the reaction field effect has minor contributions to the total eddy losses. As expected, the influence of the reaction field increases with the speed. The losses found in the machine were 3.8 W at no-load, and 22 W at full load. This corresponds with earlier published values [30] in Table 5.3, obtained by the multislice 2D - 2D technique.

In [74], also PWM losses were studied in the permanent magnets of the YASA machine. Using PWM has a significant effect on the losses in the magnets: according to [74], the loss with 5 kHz PWM increases from 22W to 33W in case of one magnet segment. Evidently, segmentation can reduce these losses to 17.7W (two segments) or 12.8W (four segments).

To conclude, the losses in the permanent magnets can be as high as 22 W or even 33 W if PWM is included and if the magnets are not segmented. However the permanent magnet losses can be reduced to an almost negligible 4W if sufficient segmentation is considered.

5.3.4 Windage losses and bearing losses

The windage losses of the machine have been investigated by A. Rasekh via Computational Fluid Dynamics. Also this study was done for the considered YASA machine [75]. Here, for the same prototype with an airgap thickness of 1.0 mm, the windage losses were found to be 5 W per rotor, at a reference speed of 30 m/s.

This corresponds to about 3800 RPM. It was shown that the losses – as expected – are third power of speed. At 2500 RPM and considering both rotors, this means that the windage losses are less than 3 W and by consequence almost negligible for speeds lower than or equal to 2500 RPM.

For the bearing losses, the bearing supplier gives loss curves as a function of the axial and radial load. The construction of the machine is made in such a way that not the complete axial force between rotors and stator is seen by the bearings. Nevertheless, a sufficient axial load must be foreseen on the bearings to avoid small axial displacements in the bearings. The latter would cause unequal airgap thicknesses and are therefore not allowed. The axial force is a trade-off between sufficient axial stiffness on the one hand and low losses on the other hand. According to simulations in software of Schaeffler, a bearing loss of a few Watts is found at rated speed.

5.3.5 Influence of lamination stacking and magnet shapes

For yokeless and segmented armature (YASA) axial flux permanent-magnet machines, several lamination stacking methods and magnet shapes are discussed in [76], in terms of output torque, cogging torque, efficiency and power density. By evaluating the different combinations of lamination stacking methods and magnet shapes, it is shown that some combinations suffer from local saturation, lower output torque and higher losses. Especially the local saturation may have an influence on the fringing flux in the machine. In Chapter 4, it was seen that flux migrates from one sheet to another in the first few adjacent sheets closest to the excitation winding, because of saturation, which causes even more flux falling in perpendicular to the sheets. Therefore, it is interesting to summarize the results of the cited work in order to see how the flux density behaves in radial direction, for the YASA topologies with several lamination stacking methods and magnet shapes.

Four types of lamination stacking are compared: conventional lamination stacking (CLS) and 3 simplified lamination stackings (SLS1, SLS2 and SLS3). The four types of lamination stacking are shown in figure 5.8: 1) the conventional lamination stacking in Fig. 5.8(a), 2) the rectangular lamination stacking SLS1 in Fig. 5.8(b), 3) the T-shape stacking SLS3 in Fig. 5.8(c) and 4) the overlap lamination stacking SLS3 in Fig. 5.8(d).

The two considered magnet shapes are on the one hand trapezoidal magnets (Fig. 5.9(a)) with a width of 0.8 times the pole pitch, and on the other hand an assembly of two rectangular magnet segments that are combined into a T-shaped magnet (Fig. 5.9(b)). The width of the upper magnet is limited to the width of the pole pitch at the average radius.

The comparison of lamination stacking methods and magnet shapes in terms of losses, power density and efficiency is given in Tables 5.4 and 5.5. The Tables show that the lamination stacking technique has an effect on the output power and the efficiency: compared to the CLS, the rectangular stacking has about 6%

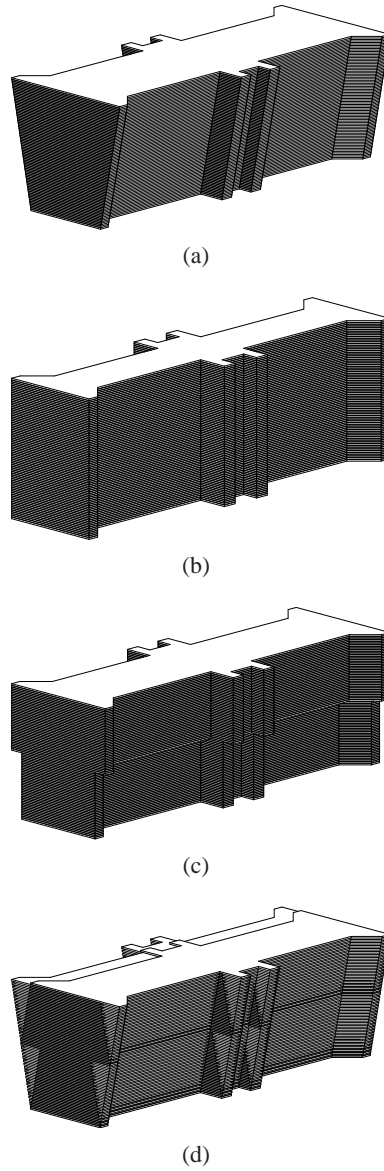


Figure 5.8: Overview of the lamination stacking methods; (a) CLS: conventional stacking method; (b) Rectangular LS: a simple stacking method with only one lamination profile; (c) T-shape LS: a simple stacking method with only two lamination profiles that are stacked straight; (d) Overlap LS: simple stacking method with only two lamination profiles that are stacked in an alternating way so that they overlap partially [76].

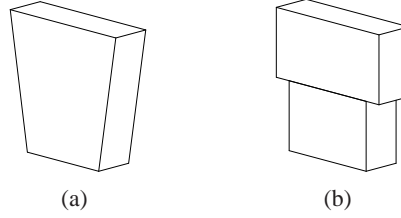


Figure 5.9: Overview of the magnet shapes; (a) trapezoidal; (b) T-shaped as a combination of two rectangular magnets [76].

lower output power and 0.57% point lower efficiency at full load. The magnet shape however has only a very small influence on these two quantities, as is seen by comparing both tables. Although this PhD does not focus on cogging torque, it is interesting to mention that the cogging torque is strongly influenced by the lamination stacking method while the magnet shape has almost no effect. Note that the considered machine with 15 stator teeth and 16 magnets has an inherently low cogging torque because no symmetry in the machine exists.

Table 5.4: Comparison of simulation results for trapezoidal magnets [76]

parameter	CLS	Rectangular LS	T-shape LS	Overlap LS
full-load torque (Nm)	15.19	14.24	14.71	14.89
no-load iron-losses (W)	35.84	50.71	42.88	35.95
full-load iron-losses (W)	32.83	45.68	38.67	31.66
output power (W)	3977.1	3728.6	3851.8	3897.7
power density (kW/kg)	0.5136	0.5560	0.5345	0.5408
efficiency at full-load (%)	96.15	95.58	95.89	96.10

Table 5.5: Comparison of simulation results for T-shaped magnets [76]

parameter	CLS	Rectangular LS	T-shape LS	Overlap LS
full-load torque (Nm)	15.19	14.23	14.75	14.91
no-load iron-losses (W)	35.98	50.52	43.19	36.19
full-load iron-losses (W)	32.95	45.68	38.94	31.79
output power (W)	3977.0	3728.6	3860.8	3902.2
power density (kW/kg)	0.5136	0.5560	0.5327	0.5414
efficiency at full-load (%)	96.15	95.58	95.89	96.10

The interesting part for the research on fringing flux, is related to the 3D magnetic field distribution in the machine, for the different lamination stacking techniques and magnet shapes. In Fig. 5.10, an overview of the magnitude of the magnetic flux densities in the different 3D-models is given.

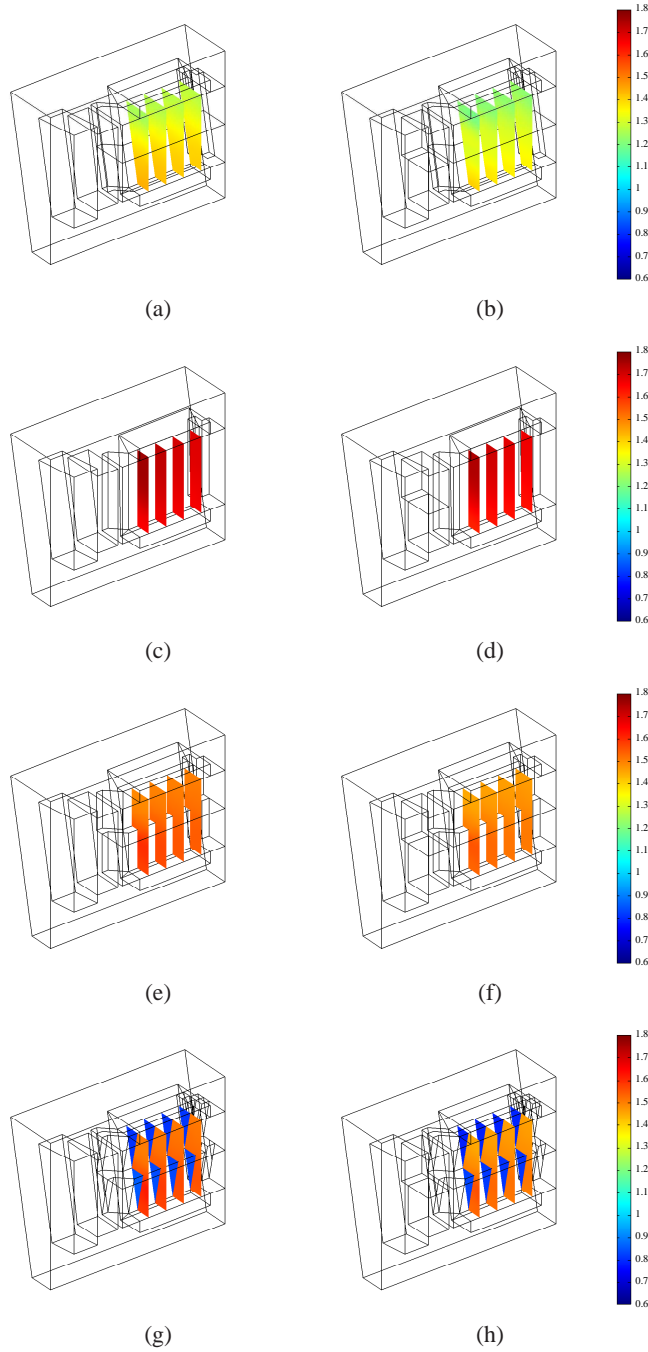


Figure 5.10: Overview of the magnitude of the flux density distribution in the tooth for each combination of lamination stacking methods and magnet shapes. The rows represent the lamination stacking method: CLS, Rectangular LS, T-shape LS, Overlap LS. The columns represent the magnet shapes: trapezoidal, and T-shaped [76]

Fig. 5.10 (a) and (b) show that with CLS, a lower flux density is obtained in the laminated steel than with the other stacking methods. This results in lower iron losses and hence higher efficiency.

Fig. 5.10 (c) and (d), show that local saturation of the lamination with rectangular LS takes place at the upper layers while the material is still not saturated at the lower layers. Therefore the output power (Tables 5.4 and 5.5) is smaller compared to the other combinations with trapezoidal and T-shaped magnets. Moreover, the no- and full load iron-losses are high, leading to a less efficient machine. It can be summarized that the Rectangular LS is not appropriate in combination with trapezoidal and T-shaped magnets.

The conclusion is that some combinations – especially the rectangular lamination stacking – result in local saturation, which may lead to higher fringing fluxes perpendicular to the lamination plane. The CLS has the lowest flux density in spite of the high output power, which causes a high efficiency because of low conventional iron losses and low expected fringing flux losses. Because all laminations have a different geometry in the CLS, this technique is unfortunately also the most expensive. Only the Overlap LS-method shows comparable properties as the CLS-method and is therefore a good alternative for the CLS because of its lower cost.

Because of the lowest production cost and the above consideration, the prototype of the machine was made with T-shape stacking, and with T-shaped magnets. Instead of 2 segments however, 3 segments for the magnets were taken, and 6 different geometries for the stator core. Further details are given in section 5.4.

5.3.6 Summary of the losses in the YASA machine

A numerical overview is given of the losses in the prototype YASA machine based on the previous studies of all loss contributions. Table 5.6 gives the summary of the conventional losses. As it is understood that geometric details such as e.g. slot opening have a large influence on the losses, the values in Table 5.6 should be seen as indicative values only.

Table 5.6: Summary of conventional losses in the YASA machine at rated speed of 2500 RPM and rated power of 4.0 kW

	Loss	Remark
Iron losses	40 – 50 W	When using grain oriented M100-23P
Copper losses	60 – 70 W	At operating temperature of 70°C
Permanent magnet losses	5 – 33 W	Highest value for 1 segment, incl. PWM
Bearing losses	2 – 20 W	Depends strongly on axial load
Windage losses	2 – 3 W	At 2500 RPM
Efficiency at full-load	≈ 95%	

5.4 Construction of the prototype

5.4.1 Overview of the prototype construction

In [7], the electromagnetic design of a 4 kW, 2500 RPM YASA-machine was optimized for energy-efficiency. This design optimization has resulted in a set of parameters listed in table 5.1. In this new design, the rated current is 10A (instead of 7 A), this because of geometrical reasons, the number of turns of the coil is adjusted (reduced) to the left space between adjacent stator teeth, which is different from the first prototype because of the aluminium fins. The mmf of both designs is the same.

Later, in [73], thermal aspects of the prototype YASA-machine have been investigated. As the rotors in axial flux machines have a disc shape, inherent self-ventilation [77] will have a significant contribution to the transfer of heat out of the machine. This effect becomes particularly interesting for axial flux PM topologies with two rotors and a single stator [78]. Nevertheless, in high torque density applications, this self-ventilation will become insufficient [79]. Therefore, an additional stator heat extraction system is suggested which consists of inward heat extraction fins *cfr* section 5.4.4.

In the construction of the stator of the YASA machine in section 5.4.4, epoxy potting techniques will be used to get the different stator parts bonded into a single solid stator structure. As this epoxy potting material has both a thermal and mechanical function, extensive tests on different epoxy materials have been carried out in the concept study towards the stator casting process.

The combination of the optimized electromagnetic design, the thermal analysis and the extensive tests on different epoxy materials have resulted in a YASA-machine of which a cross-section overview is given in figure 5.11. As this prototype machine is used for various experiments and measurements, some additional features have been added, *i.e.* adjustable airgaps and the integration of multiple sensors in the stator. The construction of this prototype is discussed in the following sections.

5.4.2 Construction of the rotors

The two rotor discs are made of 8 mm thick steel C45, and combine two major functions. Firstly, they are a back-iron for the magnetic flux, and secondly they carry the high mechanical attraction forces from the permanent magnets to the stator cores. In general, the required thickness of these rotor discs is set by mechanical constraints rather than the electromagnetic ones.

On these rotor discs, the permanent magnets are glued. These magnets are 4 mm thick in the axial direction, which is also the direction of the magnetization. In circumferential direction, adjacent magnets are magnetized in the opposite (axial) direction. In this prototype YASA-machine, each disc has 16 magnets, which results in a machine with eight pole pairs.

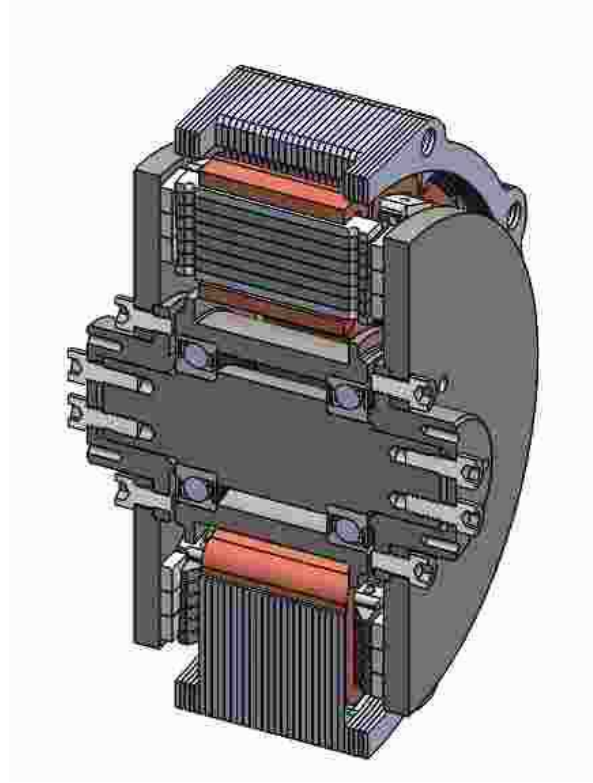


Figure 5.11: Cross section view on the prototype YASA-machine.

The permanent magnet material is NdFeB 40SH. This material grade combines a high remanent flux density, *i.e.* 1.30 T at 20 °C, with a sufficiently high maximal operating temperature of 150°C. As this material has a relatively good electrical conductivity, the eddy currents will be induced in the permanent magnets by stator slotting and stator armature reaction. To limit the eddy currents and their corresponding power losses, segmentation of the permanent magnets [74] is introduced. The segmentation reduces the eddy-current loss in the magnets as already explained earlier and shown in Table 5.3. In the prototype machine, the radial height (24 mm) of the magnet is divided into three (3 times 8 mm). The tangential lengths become 18, 21 and 24 mm. The axial thickness *i.e.* the magnetization direction is 4 mm. This 4 mm thickness results in an airgap flux density of about 0.95T. To protect the permanent magnet material from corrosion, each magnet segment is coated with a copper-nickel alloy. The rotors are shown in figure 5.12. The picture shows clearly that each magnet pole consists of 3 rectangular block magnets.

The permanent magnet segments are glued on the rotor disc. The thermal expansion coefficient of the NdFeB is negative (-0.8×10^{-6} 1/K) in the direction



Figure 5.12: Rotor discs of the prototype YASA-machine, showing the glued magnet segments.

perpendicular to the magnetization direction, and the one of steel C45 is positive and relatively big ($11.7 \times 10^{-6} \text{ 1/K}$). The big difference in thermal expansion coefficients requires flexibility of the glue. Moreover, the strength of the glue should not reduce significantly at the nominal operating temperature. In the prototype machine, a 2-part, room temperature curing methyl-methacrylate (Permabond TA 4246) based structural adhesive is used.

5.4.3 Construction of the modular stator element

Together with the rotor discs with the permanent magnets, the modular stator elements are the electromagnetic active components of the machine. Such a modular stator element includes a ferromagnetic core and a concentrated winding.

In the prototype YASA-machine, the ferromagnetic core is made of thin laminated silicon steel sheets. As the direction of the magnetic field in these cores is always in the axial direction, a grain oriented material M100-23P is used. As explained in section 5.3.1, in the YASA-machines, the use of such a grain oriented material results in strong reduction of the core losses in comparison with non-oriented ones [69]. In theory ¹, the use of this grain oriented material results in core losses of about 40 W at rated load and speed in the prototype machine (30 W is given in [69] but at a speed of 2000 RPM; quadratic extrapolation to 2500 RPM

¹Neglecting the degradation of the magnetic material properties due to cutting process, perpendicular fringing fluxes, *etc.*

gives 47 W).

As the magnetic flux density over the radial direction in a stator core element is not uniform, a variable airgap is also introduced in the prototype machine [29]. The variable airgap is obtained by shortening the axial direction of the stator laminations in the radial direction. A variable airgap has a higher airgap thickness at the inner radius of the core elements, because these elements are generally more sensitive to local saturation. As a consequence, the higher airgap thickness at the inner radius results in a desaturation of the core at the inner radius, and if the variation in the airgap is chosen carefully, a uniform magnetic flux density over the radial direction in the core. This results in less iron losses for the same flux per tooth, and by consequence in less power losses for the same output power.

After the stack of the stator core is made, it is impregnated in an epoxy resin to keep the individual steel laminates in place. Then, an electrical isolation foil is wound around the core. On this insulation foil, the winding is placed. This winding is composed of two parallel strands of 1.12 mm diameter. The number of turns is equal to 57. The wires of each core element are brought to the outside of the stator; in such a way the individual electromagnetic behaviour of each coil can be measured. Finally, a second layer of electrical isolation is put over the winding. This isolation layer is required because of the close contact between the winding and the heat extraction fin *cfr.* section 5.4.4. The housing structure with radially inward fins can be seen in figure 5.13, as well as one finished stator module that is to be inserted between the radial fins. A detailed image of a modular stator element is shown in figure 5.14.

5.4.4 Casting techniques for the stator

In a next production step, a stator assembly needs to be made out of the 15 pre-assembled stator modules. Also a connection with the rotors and the final application needs to be provided. Moreover an additional cooling system for the stator modules is introduced.

The 15 pre-assembled stator modules are arranged in a circle configuration, and the bearing block is put concentrically with them. The bearing block will be the interface between the stator and the rotors; the bearings and shaft will be integrated in a later construction step. The outer cylindrical boundary is formed by the stator housing. This housing is also used to mount the prototype machine to the application. Figure 5.15 shows the manufacturing of the housing by stacking the aluminium sheets, and figure 5.13 shows the finished stator housing.

The remaining openings between the inner bearing block and the outer stator housing will be filled with epoxy. The use of epoxy resins as a potting material has also a major impact on the thermal design of the machine. These epoxy resins have a relatively low thermal conductivity between 0.25-0.85 W/m·K [80]. By consequence, a high thermal resistivity between the heat sources, *i.e.* the iron losses in the cores and the copper losses in the winding, and the surface of the stator



Figure 5.13: The stator housing of the prototype YASA-machine with one of the 15 stator modules shown at the bottom right. The white cover of the stator module is a glass fiber insulation.

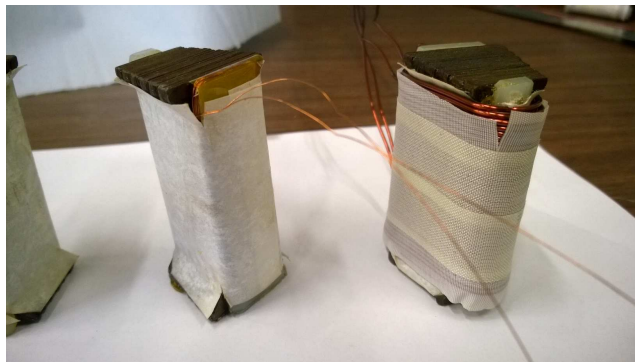


Figure 5.14: Stator modules. The location of the search coil to measure the fringing flux are shown on top of the lamination stack (left). Afterwards the lamination stack is provided with the main winding and electrical isolation (right).

housing limits the power output of the machine. To increase the conductive heat flux from the stator modules to the stator surface, inward heat extraction fins are integrated in the stator housing as illustrated in figures 5.13, 5.15 and 5.16. The fins reach up to the inner diameter of the stator winding to have a high contact surface with the stator winding. Moreover, the stator housing is made of an aluminium alloy because of its good thermal conductivity. In order to avoid eddy currents [81]

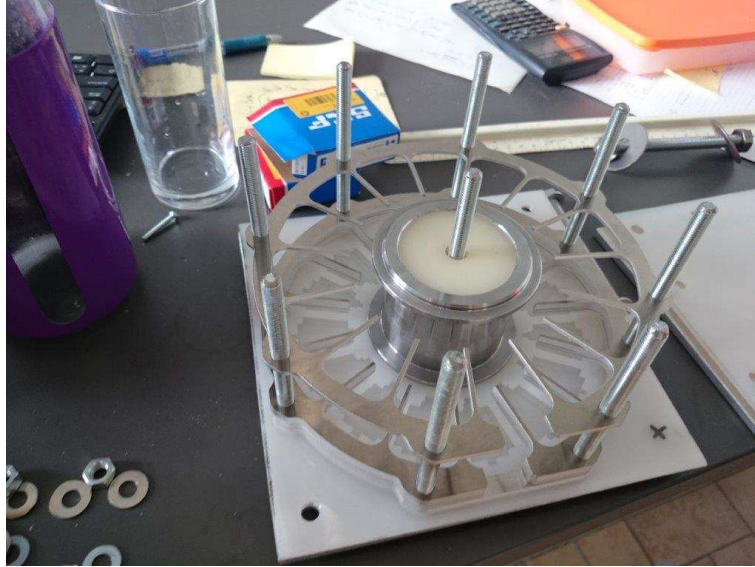


Figure 5.15: The construction of the stator housing of the prototype YASA-machine, and the bearing block in the middle. The white material in the middle is in a later stage replaced by the ball bearing. The finished stator housing is shown in figure 5.13.

in the inward heat extraction fins due to leakage fluxes in the slot openings, the stator is made by a stack of coated aluminium profiles as can be seen in the figures 5.13 and 5.15. Near the end windings, a sufficiently high distance is maintained towards electrically conductive parts in order to avoid eddy-current losses. Despite the reduction of the thermal resistance, the inward heat extraction fins reduce the winding thickness, and hence, will result in an increase of the copper resistance and copper losses. The ratio between the fin thickness, *i.e.* better cooling, and the winding thickness, *i.e.* lower copper losses, is optimized in the multiphysics design.

As mentioned previously, the epoxy resin is used as a potting material and fills all the remaining openings between a mold formed by the bearing block at the inner diameter and the stator housing at the outer diameter. As a consequence, the epoxy material is the only securing means to keep the stator modules in place. On the other hand, the epoxy material has also an effect on the thermal properties of the machine. Therefore, the selection of the epoxy resin is critical in this construction method.

First of all, the epoxy resin should have a *high strength up to high temperature* as it must be capable to withstand the high forces from the rotor-stator interaction. These forces can be in the axial direction *e.g.* during the mounting of the discs or because of small asymmetry in the airgaps or magnetization of the rotors. The

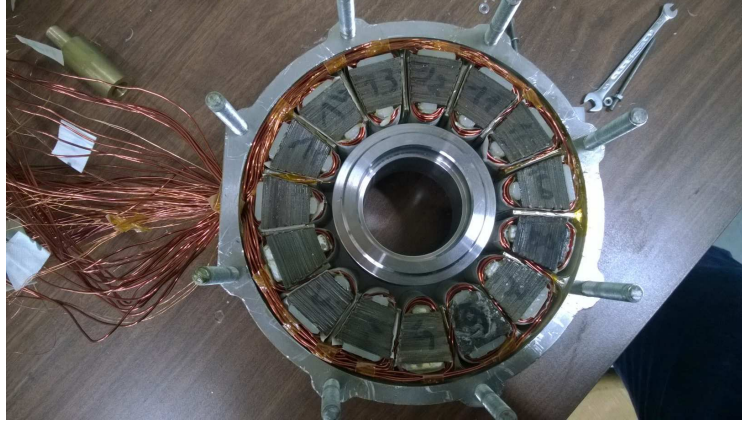


Figure 5.16: Axial-flux PM machine stator before the epoxy potting process.

forces can also be in the circumferential direction *e.g.* because of torque production. The epoxy resin should be capable to withstand these forces at operating temperatures. A critical parameter in the selection of the epoxy resin is therefore the glass transition temperature. At this glass transition temperature, the epoxy resin loses its strength. As a consequence, the glass transition temperature of the epoxy resin should be sufficiently higher than the maximum temperature during operation of the machine.

Secondly, the *thermal expansion coefficient* of the epoxy resin is also important. In many places in the stator, there is a very thin layer of epoxy between copper-iron and copper-aluminium alloy surfaces. Temperature transients during operation of the machine will result in expansion of the different stator parts. An epoxy resin with a thermal expansion coefficient that is more or less in the range of these of copper, steel and aluminium alloy is therefore advantageous.

Thirdly, the *thermal conductivity* must be as high as possible. The epoxy resin will have an influence on the thermal properties of the machine. Despite the inward heat extraction fins have been introduced to have a better heat conduction path in the machine, an epoxy resin with a high thermal conductivity is still advantageous. The epoxy resin will fill the thin gaps between *e.g.* different wires of the stator module coils and the inward heat extraction fins, and hence, also contribute to better thermal conductive paths between the different stator parts.

The epoxy resin should have a *viscosity* as low as possible during the casting process, to fill even the smallest cavities in the stator. Although the epoxy resins have a relatively poor thermal conductivity, air inclusions have an even worse influence on the heat evacuation of the machine. Low viscosity epoxy resins will result in less air inclusions, and hence, a better thermal performance. Moreover, too many air inclusions will also reduce the strength of the stator. The choice of the epoxy resin with low viscosity is not the only way to eliminate air inclusions. Pre-

heating of the epoxy resin before casting will also lower the viscosity of the resin. Also preheating of the stator components can be help; although the epoxy resin is preheated, direct contact with a cold stator part will immediately cool down the epoxy resin with an increase of the viscosity as a consequence. Last but not least, air inclusions can be eliminated by mechanical vibrations and vacuum casting.

During the selection of the epoxy resin, taking the previously mentioned requirements into consideration, four resins have been retained. The Elantas Epoxylite TSA220S, Henkel Stycast 3050 with catalyst 28, Henkel Stycast 2850 FT with catalyst 27-1 and Henkel Hysol EO 1058. The main parameters of these epoxy resins are mentioned in table 5.7.

Before the casting of the entire stator, the properties of the epoxy resins were evaluated in small test samples. In these test samples, a steel cylinder was consecutively wound with a first layer of electrical isolation material, a copper winding and another layer of electrical isolation material. Finally, this assembly is put into an aluminium alloy casting profile. These small test samples are very similar to a stator module, but use less effort and cost to produce.

As mentioned previously, the samples are heated up to 80 °C for lowering the viscosity of the epoxy resin. During the curing, the sample filled with epoxy is heated at the listed curing temperature and time. Consecutively, the sample is heated for 2 more hours at the service temperature *i.e.* 120 °C. After these 2 hours, the temperature is gradually decreased in a period of about 8 hours.

After the casting process, the samples are cut to evaluate the occurrence of cavities in the epoxy resins into the different sample structures and the presence of cracks. In figure 5.17, the presence of cavities and cracks in the epoxy resins is shown for the different sample structures in the test sample are shown.

Evaluation of the test samples showed that the Epoxylite TSA220S suffered from major cracks into the massive epoxy parts. Even when using filling materials *e.g.* cut glass fibers, the cracks remained in the massive epoxy parts. The Stycast 2850 is interesting because of its high thermal conductivity, but the interpenetration into the winding was less effective: the cavities in the blue resin are clearly visible on the picture. This is due to the relatively high viscosity of the Stycast 2850. Despite the Hysol EO 1058 has also a relatively high viscosity, here, the interpenetration of the epoxy resin into the different sample parts was more effective. Moreover, the Hysol EO 1058 is a single component, and hence, easy to use. Nevertheless, its relatively high viscosity and by consequence the risk on cavities was decisive to choose the Stycast 3050: the resin with lowest viscosity but unfortunately also a rather low thermal conductivity (compared to Stycast 2850).

Before the casting of the stator, some research was done on the mechanical stresses during and after the casting process. Initially, there are no mechanical stresses in the stator modules, bearing block and stator housing. During the casting process, these pieces are heated up to the curing temperature. During this process, the elevated temperature introduces mechanical stresses in the stator modules, bearing block and stator housing, while no mechanical stresses are present

Table 5.7: Properties of the selected epoxy resins. In case of two component epoxy resins, the properties for the mix (epoxy+catalyst) is given.

Property	Unit	Epoxylite TSA220S	Stycast 3050	Stycast 2850 FT	Hysol EO 1058
Color	g/cm ³	amber	maroon	blue	black
Density	g/cm ³	1.18	1.55	2.3-2.5	1.65
Brookfield viscosity	Pa·s	5.5	2	200-300	50
Glass transition temperature	°C	143			140
Hardness	Shore D	90	88	94	90
Tensile strength	MPA	110	54		69
Compressive strength	MPA		144		
Coefficient of thermal expansion	μm/m·°C	50	40		24
Thermal conductivity	W/m·K	0.23	0.4	1.0661	0.54
Temperature range of use	°C		-40 to +130	-40 to +175	?
Cure temperature	°C	165	120	120	140

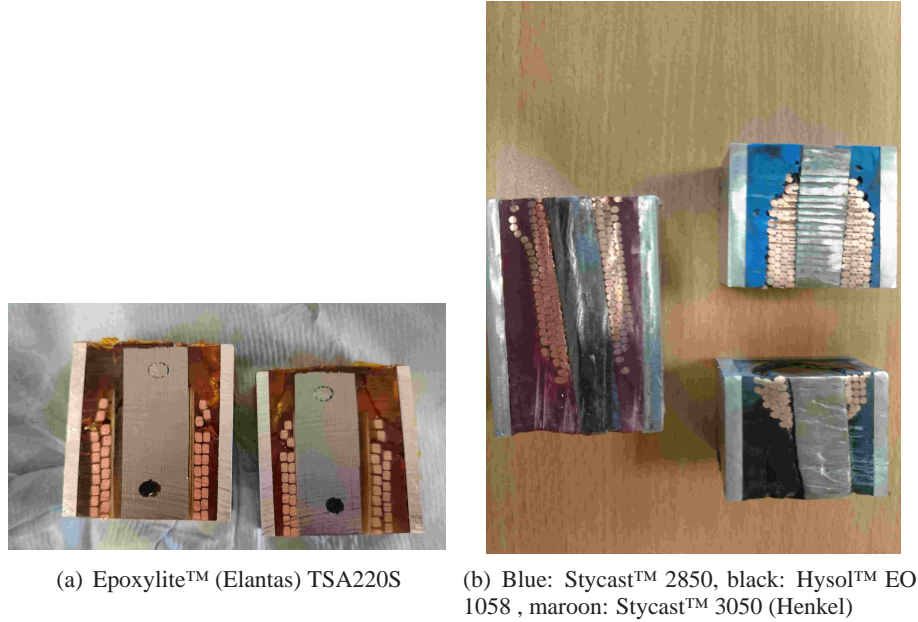


Figure 5.17: Evaluation of cavities and cracks in the epoxy resins for casting experiments in the different sample structures in the test sample.

into the epoxy resin. After the curing, the temperature is decreased again. During the cooling, the residual stresses in the stator modules, bearing block and stator housing compensate somewhat the higher coefficient of thermal expansion of the epoxy resin in comparison to these of the stator modules, bearing block and stator housing.

5.4.5 Mechanical assembly allowing adjustable airgaps

To measure the effect of the airgap thickness on the fringing fluxes at the stator cores, both airgaps of the prototype YASA-machines are adjustable. Therefore, an adaptor interface is used which connects the shaft with the rotors. On the rotor discs, two types of holes are made. The first type of holes is provided with (screw) thread. This thread is also used to mount the rotors on the adaptor interfaces. Initially, bolts are placed in these holes and are maximally inserted into the rotors. This results in a distance between the magnets and the stator cores, so that the attraction forces between both is still limited. Then these bolts are gradually unscrewed, which results in a decrease of the airgap due to the attraction forces between the magnets and the stator cores. Finally, when the airgap has the right thickness, a set of additional bolts is used to secure the position. Therefore, the adaptor interface is equipped with holes with thread.

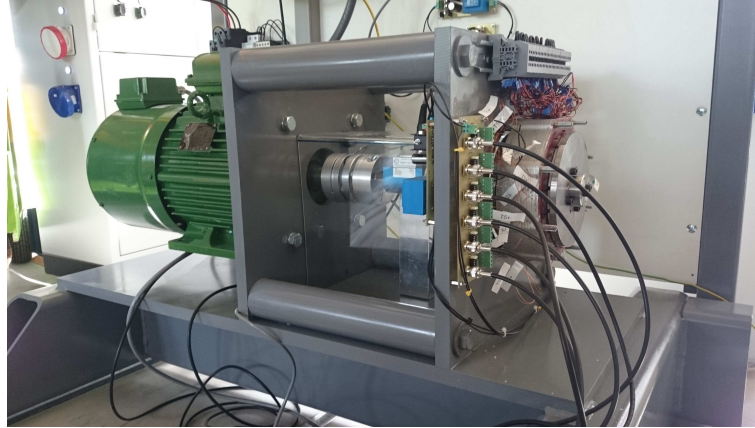


Figure 5.18: Axial-flux PM machine test set-up. From left to right: load (asynchronous) machine, torque sensor with couplings, axial flux PM prototype machine.

This mechanical assembly does not only allow a uniform variation of the air-gap, but also non-uniform airgaps over the circumference are possible. These non-uniform airgaps are required to study the effect of eccentricity [82].

5.4.6 Search coils for fringing flux

During the construction of the AFPMSM prototype, multiple sensors have been integrated inside the machine: search coils to measure the induced voltages caused by the main flux in a module, at both sides of the stator core, and search coils to measure the fringing flux, and multiple RTD-sensors to measure the temperatures in different parts of the machine.

The most important for this research is the fringing flux search coil. Figure 5.14 shows this coil mounted on top of the lamination stack of a stator module core. The search coil consists of 20 turns of 0.2 mm wire diameter and encloses a surface of 17.3 mm by 7.3 mm.

5.5 Experimental set-up

5.5.1 Overview of the complete setup

To perform measurements, the axial flux PM prototype is placed into a test set-up of which an overview is given in figure 5.18. In this test set-up, an asynchronous 7.5 kW, 3000 RPM motor is used as a load machine and is powered by a commercial drive. Set-points to this drive for the speed (or torque) are given by a dSPACE 1104 platform. The feedback of the speed signal is realised by an incremental

encoder attached to the asynchronous motor. Together with the torque value measured by the Lorenz DR2112 (nominal torque of 50 Nm, accuracy of 0.1%) torque sensor, an accurate value of the mechanical power is achieved. Measurement of the power on the electrical side of the prototype machine is done using a Tektronix PA4000 power analyser. Interface boards are made to transfer the different sensor signals into the dSPACE platform.

The axial flux PM machine can be operated using a dSPACE controlled custom-designed inverter using a Semikron SEMiX101GD12E4s IGBT-module, or can be connected to a fully-programmable three-phase load. For the measurements performed in this research, the axial flux PM machine is used as generator connected to the fully-programmable three-phase load. This load has the advantage of using no pulse-width modulation, which make the measurements less sensitive to EMI.

5.5.2 Measurements of torque and total losses

Figure 5.19 shows the total measured losses in the machine in function of the speed and torque. The corresponding efficiency is given in figure 5.20. The smooth colours are a result of smoothing. It can be seen that the efficiency is above 94% in a lot of operation points. Table 5.8 shows the individual loss components of the machine at rated speed of 2500 RPM and an RMS stator current of 7 A. The total fringing flux losses in rated for this condition is 1.508 W, which is 3.2 % of the total iron losses. The bearing losses are not accurate, because of the torque sensor limitations (small torque values compared to the measurement range of the torque sensor). The bearing and windage losses are measured with non-ferromagnetic rotors in order to exclude iron losses.

Table 5.8: Summary of losses in the YASA prototype machine at rated speed of 2500 RPM and an RMS stator current of 7 A

	Loss	Remark
Iron losses	47 W	
Copper losses	70 W	At operating temperature of 70°C
Permanent magnet losses	12.8 W	
Bearing losses	20 W	Depends strongly on axial load
Windage losses	3 W	At 2500 RPM
Fringing flux losses from PM	0.03 W%	
Fringing flux losses from armature reaction	1.478 W%	

5.5.3 Low noise data acquisition of the fringing flux coil signal

The voltage induced in the fringing flux coil remains very limited; from 74,1 mV peak at rated speed and no phase currents, to 150 mV peak at rated speed and rated

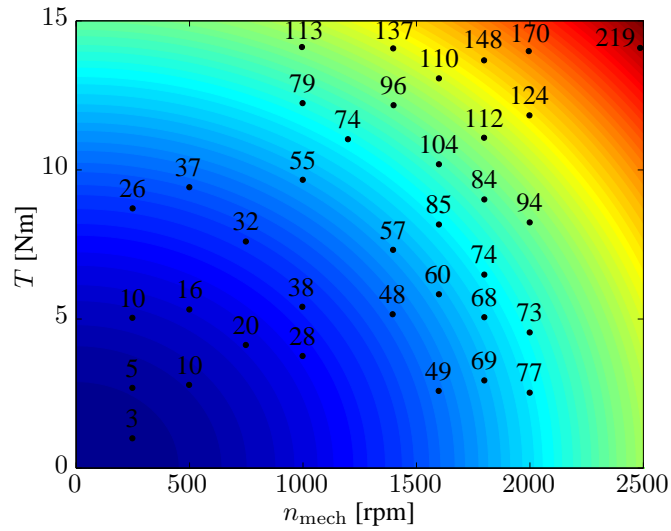


Figure 5.19: Measured total losses [W] in function of the mechanical speed n_{mech} and torque T of the prototype machine.

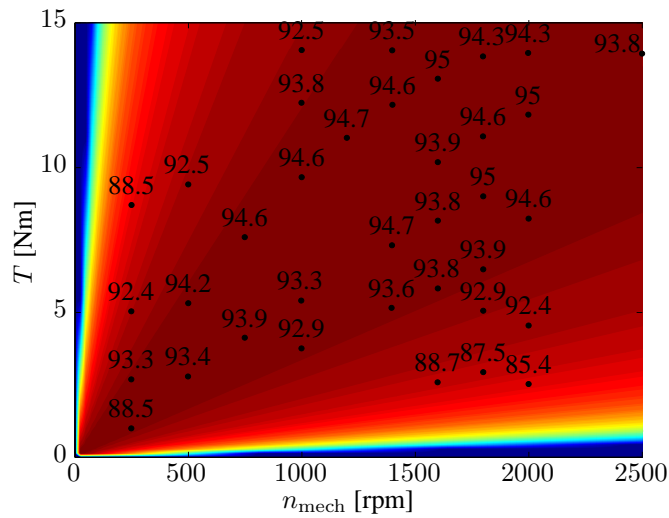


Figure 5.20: Measured efficiency of the mechanical speed n_{mech} and torque T of the prototype machine.

phase currents. Therefore some actions are performed to improve the signal-to-noise ratio.

The axial flux PM machine is used as a generator connected to the fully-programmable three phase load instead of the custom-designed axial flux PM machine inverter. In contrast to the inverter, the three phase load uses no pulse-width

modulation (PWM). As a consequence, the absence of a high frequency switching signal of the PWM has a positive impact on the electromagnetic interference (EMI), and hence, improves the signal-to-noise ratio.

In order to amplify the low voltage signal of the fringing flux coil to a sufficiently high level, *i.e.* ± 10 V for the ADCs of the dSPACE 1104 platform, a noninverting operational amplifier circuit is used. To cancel out EMI in the connection wires between the fringing flux coil and the amplifier circuit, twisted-pair cabling is used. Moreover the amplifier circuit is located as close as possible to the stator sensor wire opening to reduce the length of the fringing flux coil wires.

5.6 At no-load: fringing flux caused by the permanent magnets

5.6.1 Waveforms of flux in the tooth search coil

The tooth search coil is not to be confused with the fringing flux coils for measuring fringing flux. The tooth search coil is a winding around a stator tooth, to measure the main flux, which is in axial direction. Before studying the fringing flux, we first validate the main flux in the stator tooth of the 3D FEM model (as described in section 2.3.6 of chapter 2), by comparing it with measurements. The machine was at no load and at a speed of 2500 RPM. The measured flux in the tooth search coil is compared with the simulated flux in 3D FEM. Figures 5.21 and 5.22 show respectively the measured and simulated flux through the tooth search coil. In the measurement, the flux is obtained by integrating the voltage in the tooth search coil. It is seen that the noise level on the measured flux is quite low, and that the simulated waveform is smooth, indicating a sufficiently fine discretization in both time and space. Moreover, the correspondence between the measured and simulated waveforms is good.

5.6.2 Waveforms of emf in the fringing flux search coil

The waveforms in the fringing flux search coil of the prototype machine are measured and simulated at a constant speed of 2500 RPM, without stator currents. The airgap widths are constant, at 1.0 mm. The influence of different rotation speeds, different stator currents, and different airgap sizes is studied in later sections in this chapter.

Figure 5.23 shows the measured induced voltage (blue) in the fringing flux search coil. As can be seen in the picture of the search coil in figure 5.14, the coil has a small surface and a – for construction reasons – rather small number of turns. Therefore, the signal has a very low voltage, and by consequence the signal-to-noise ratio in the signal is low.

From the raw signal, a signal with reduced noise is constructed in the following way. First, the time signal is captured during a complete mechanical revolution.

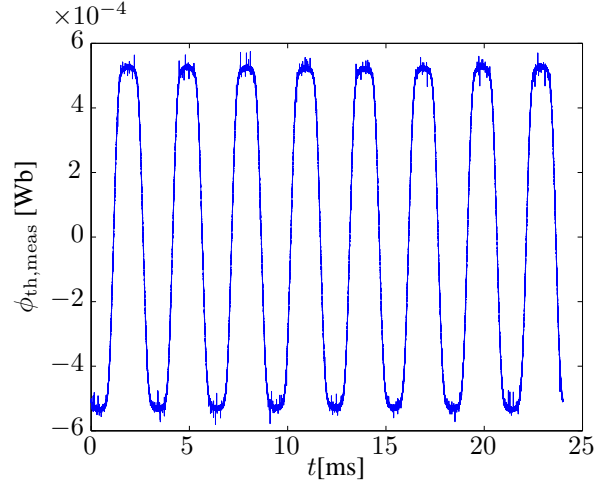


Figure 5.21: Measured flux through the tooth search coil $\phi_{th, meas}$.

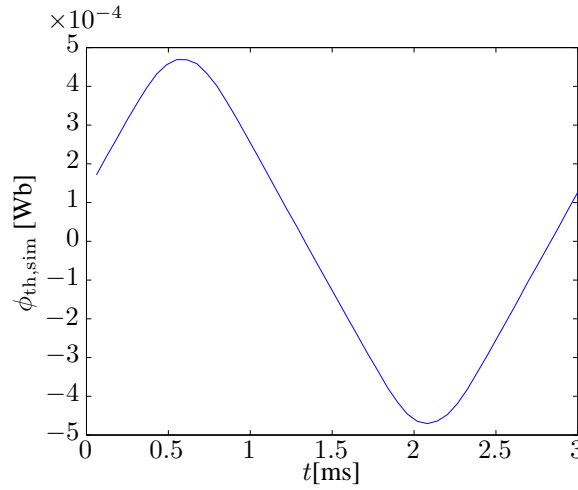


Figure 5.22: Simulated flux through the tooth search coil $\phi_{th, sim}$.

The resulting waveform is transformed into a Fourier series of which figure 5.24 shows the harmonic content. It can be seen that the fundamental frequency, third and fifth harmonic are dominant i.e. orders 8, 24 and 40. Other harmonics are at least 5 times smaller than the 40th and at least 40 times smaller than the 8th. It is not surprising to see these harmonics to be dominant in this no-load experiment, as also these harmonics are dominant in the spatial spectrum of the permanent magnets. To make the waveform clear, the time domain signal is reproduced by considering only those three dominant harmonics. The result is the red waveform in figure 5.23.

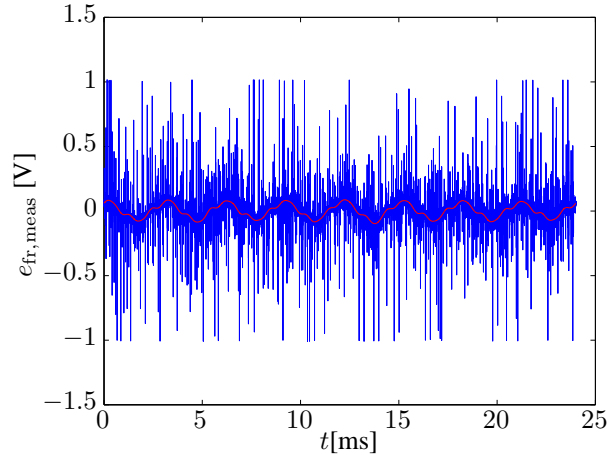


Figure 5.23: Measured *emf* in the fringing flux search coil $e_{fr,meas}$ in function of time t : unfiltered waveform (blue) and waveform considering only the three most dominant harmonics (red).

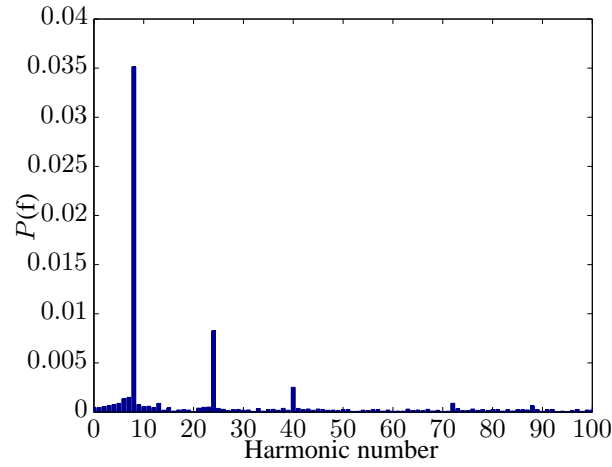


Figure 5.24: Present harmonics in the measured (unfiltered) *emf* waveform of the fringing flux search coil.

The “noise free” time signal – which is the same as the red curve in figure 5.23 – of the induced voltage in the search coil is shown in detail in figure 5.25. The flux through the coil – which is the fringing flux – is found by integrating the measured noise free signal: see figure 5.26.

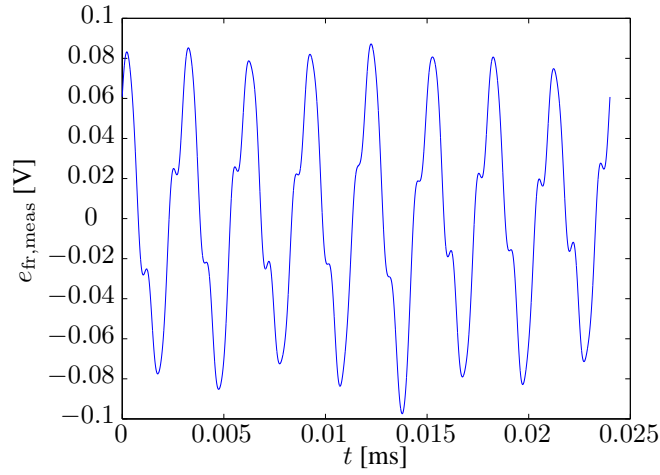


Figure 5.25: Measured *emf* in the fringing flux search coil $e_{\text{fr,meas}}$ without noise at a speed of 2500 rpm.

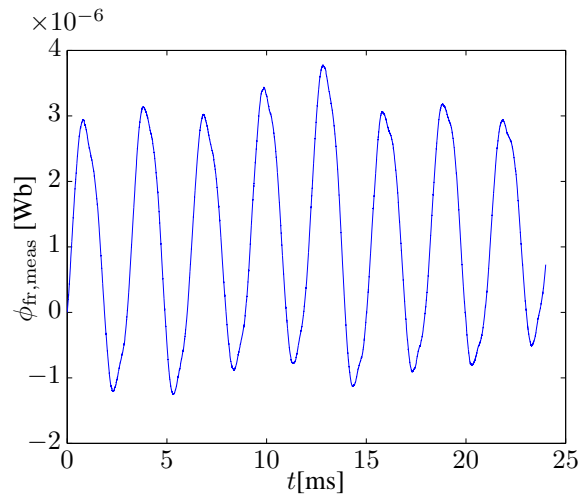


Figure 5.26: Measured flux through the fringing flux search coil $\phi_{\text{fr,meas}}$.

5.6.3 Origin of the dips in the emf waveform

The waveform in figure 5.25 clearly shows some “dips”. These dips are not measurement noise. The following paragraph explains their origin by making a comparison with 3D FEM simulations and field plots.

Figure 5.27 and 5.28 show the field lines at no load for a speed of 2500 RPM, at the moment that the PM is respectively aligned and unaligned relative to the stator tooth. It can be seen that in the case of an unaligned PM, more fringing flux is falling in perpendicularly to the plane of the lamination sheets, especially

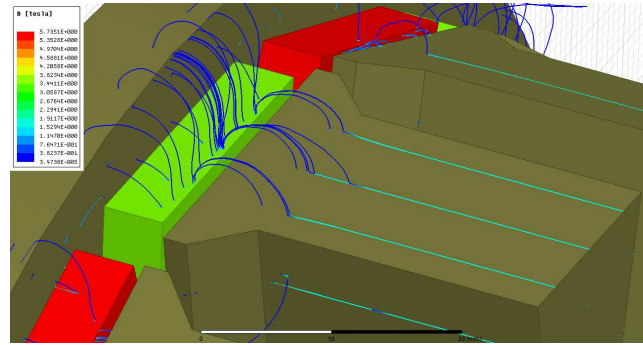


Figure 5.27: Field plot at no-load and 2500 RPM; magnet pole aligned with stator tooth.

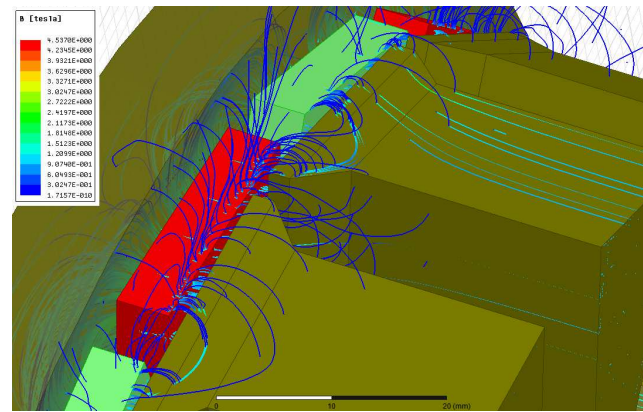


Figure 5.28: Field plot at no-load and 2500 RPM; magnet pole unaligned with stator tooth.

at the edges. The cause is the shape of the pole in permanent magnets. Each pole consists of 3 rectangular block magnets – see section 5.4.2 about rotor construction of the prototype – and does not have the arc of a circle at highest radius. By consequence, the magnet “protrudes” the plane at outer radius r_0 (radius of the top of the laminated stack) in the unaligned position in figure 5.28.

This increase of the flux in unaligned position can also be proven numerically by computing the flux linkage with the search coil. In FEM, a surface integral of the normal flux density component was taken over a surface with identical position and dimensions as the search coil of figure 5.14. This is done as a function of time, resulting in the simulated flux waveform shown in Figure 5.29. At points a and c, the PM is unaligned relative to the stator tooth, as is the case in figure 5.28. At point b, the PM is aligned relative to the stator tooth as is the case in figure 5.27. It is observed that there is a little drop in flux in the aligned position. By taking

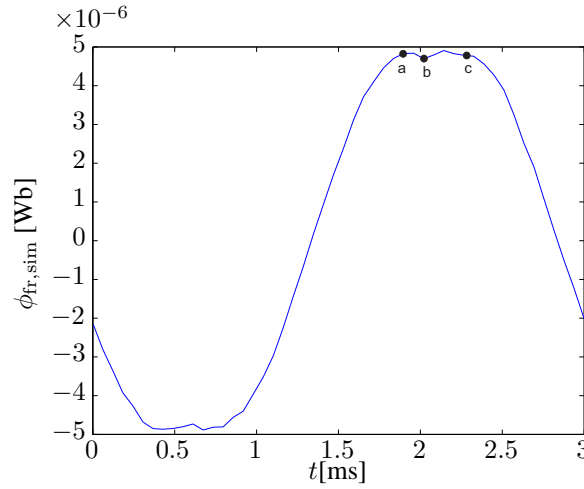


Figure 5.29: Simulated flux through the fringing flux search coil $\phi_{fr,sim}$ in no-load operation mode.

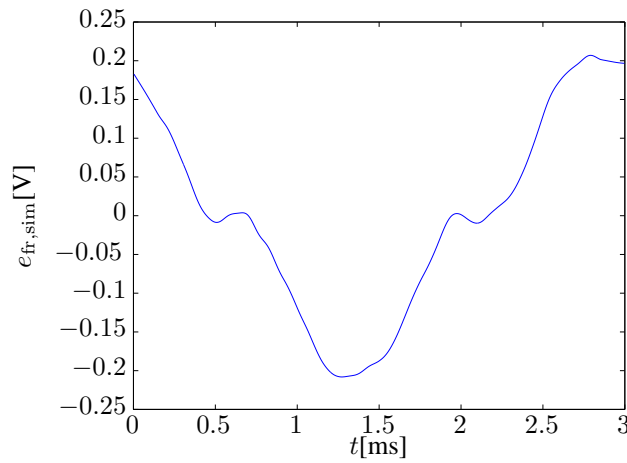


Figure 5.30: Simulated *emf* in the fringing flux search coil $e_{fr,sim}$ at no-load and at a rated speed of 2500 RPM.

the derivative of this simulated flux and multiplying it with the number of turns, the *emf* in the search coil is obtained from 3D FEM. The resulting waveform is shown in figure 5.30. The drops in the simulated *emf* are similar to the drops in the measured *emf*, as shown in figure 5.25.

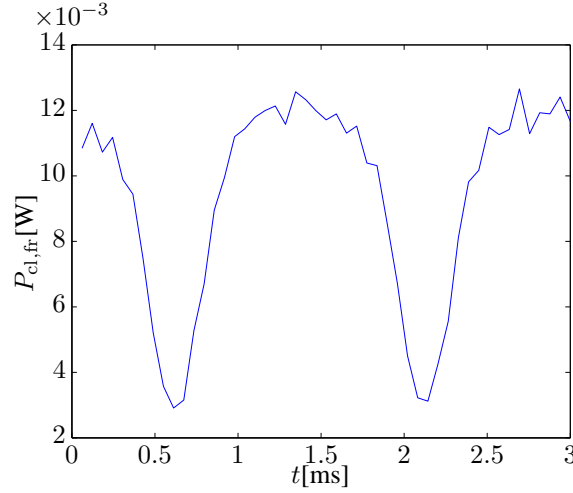


Figure 5.31: Simulated instantaneous eddy-current losses due to fringing flux $P_{cl,fr}$ at no load and 2500 RPM in one half of a motor tooth.

5.6.4 Fringing flux losses

Figure 5.31 shows the instantaneous eddy-current losses caused by fringing flux calculated directly by the 3D FEM model of a half motor tooth. These inductance limited eddy-current losses are separated from the resistance limited eddy-current losses by use of the second separation technique of section 2.2.3. This loss (30 mW for the complete machine) has to be compared with the total iron losses in the same operating condition, as found in section 5.5.2. The fringing flux loss at no-load is 0,75% of the total iron losses.

5.7 At load: fringing flux caused by PM's and stator currents

5.7.1 Waveforms of emf in the fringing flux search coil

Figure 5.32 and 5.33 show the waveform of the induced voltage and flux linkage of the fringing flux search coil at a load current of 5 A. When comparing figure 5.26 with figure 5.33, it is clear that the excitation winding has a larger influence on the fringing flux than the permanent magnets: the peak value of the *emf* (74,1 mV) at no load is much smaller compared to the *emf* (150 mV) at a load of 5 A.

Similar to the no-load situation, Figure 5.32 shows dips in the *emf* waveform. It is expected that these dips are also caused by the magnets that protrude the plane $r_0 = \text{cst}$ in unaligned position, where r_0 is again the outer radius of the lamination stack. This is indeed proven by 3D field plots for the considered loading condition:

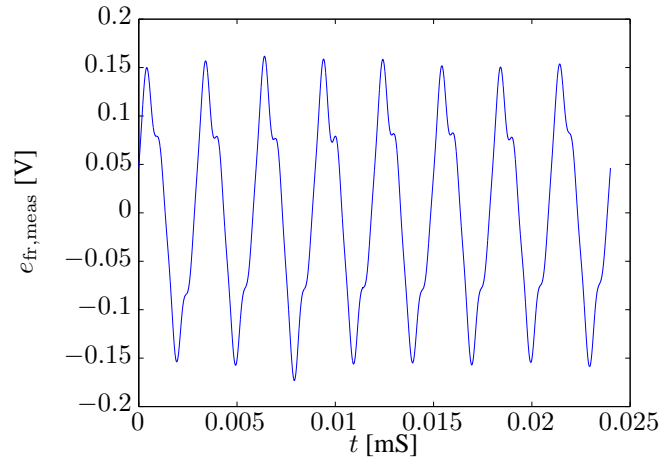


Figure 5.32: Measured *emf* in the fringing flux search coil $e_{\text{fr,meas}}$ without noise at a rated speed of 2500 RPM and a load current of 5 A.

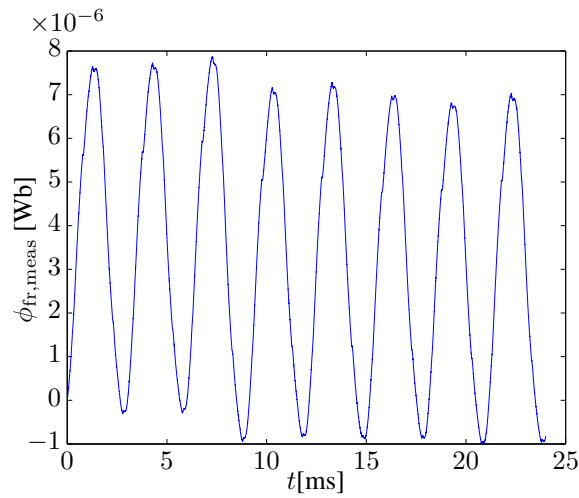


Figure 5.33: Measured flux through the fringing flux search coil $\phi_{\text{fr,meas}}$ at a rated speed of 2500 RPM and a load current of 5 A.

figure 5.34 and figure 5.35 show the field lines at full load for a speed of 2500 RPM, at the moment when the PM is respectively aligned and unaligned relative to the stator tooth. Therefore, the same explanation for the dips can be given as at no-load.

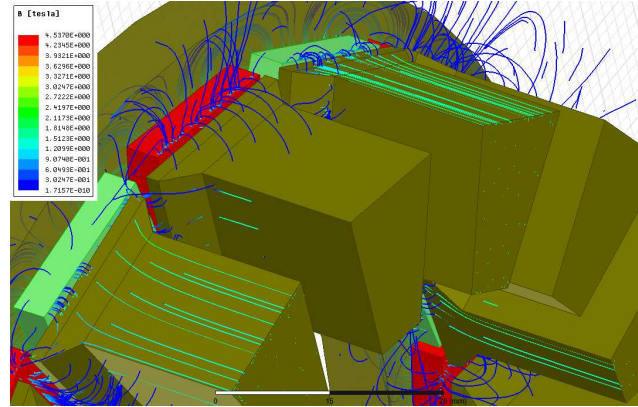


Figure 5.34: Field plot at full load and 2500 RPM; magnet pole aligned with stator tooth

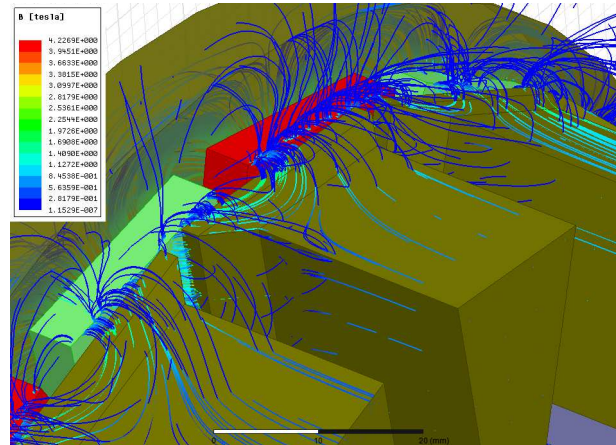


Figure 5.35: Field plot at full load and 2500 RPM; magnet pole unaligned with stator tooth

5.7.2 Influence of stator current amplitude on fringing flux

Figure 5.36 shows the measured stator current waveform in function of time at a load of 5 A and a speed of 750RPM. It is already observed that the induced voltage in the fringing flux search coil is higher at load than at no-load. It is interesting to study the influence of the stator current amplitude. This is shown in figure 5.37. As expected, more fringing flux is generated for increasing stator current. This effect is already observed in chapter 4 and can be seen in figure 4.6. The experiment is done at 1000 RPM. It is observed that at 0 A (no-load) and at 5 A current, the induced voltages are about 23.4 mV and 38 mV, while they were found to be 74 mV

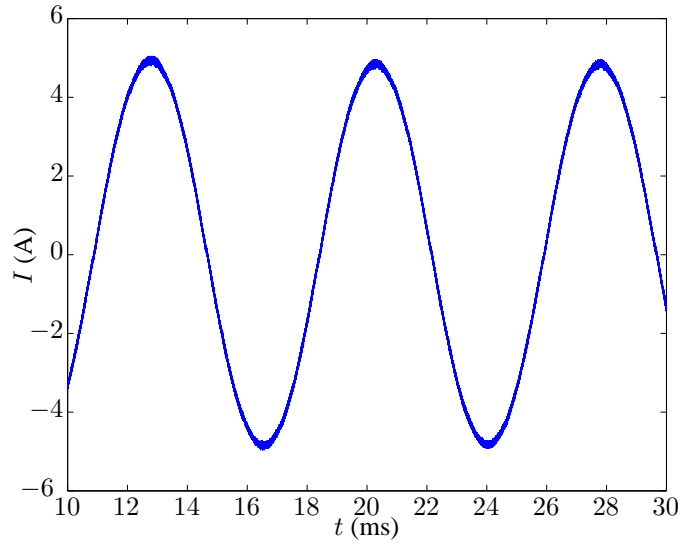


Figure 5.36: measured stator current waveform at a load of 5 A current and 750 RPM.

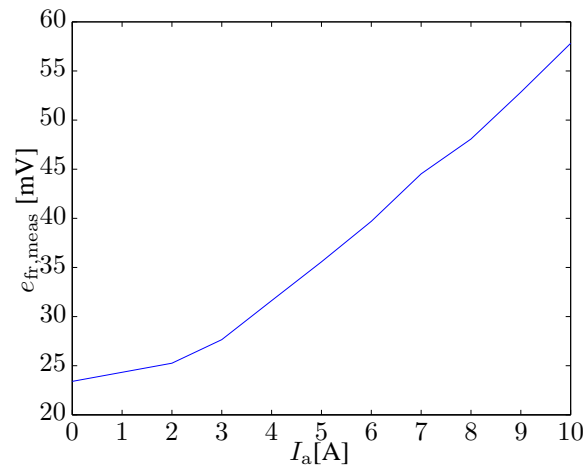


Figure 5.37: Measured *emf* in the fringing flux search coil $e_{fr,meas}$ in function of the armature load current I_a at a speed of 1000 RPM.

and 150 mV resp. for the same currents and at 2500 RPM. For full load, the *emf* is about 43 mV. It can be concluded that the induced voltage almost doubles from no-load to full load, and that this statement can be done at both 1000 RPM and 2500 RPM.

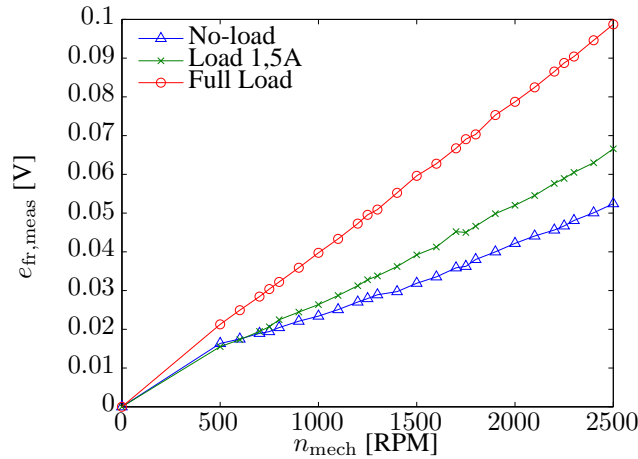


Figure 5.38: Measured *emf* in the fringing flux search coil $e_{\text{fr,meas}}$ in function of the mechanical speed n_{mech} .

5.8 Fringing flux as a function of rotation speed

Figure 5.38 shows the induced voltage in the fringing flux search coil of figure 5.14 in function of the mechanical speed. Because of the low signal-to-noise ratio at very low speeds, it was not possible to do accurate measurements below 500 RPM. Several measurements were done between 500 RPM and 2500 RPM, for no-load, part load (1.5 A stator current) and full load (7 A stator current).

In order to have a more detailed view on the behaviour of the induced voltage, a new figure (figure 5.39) is made wherein the measured induced voltage of figure 5.38 is divided by the mechanical speed. From this figure, interesting conclusions can be drawn regarding the behaviour of the fringing flux as a function of speed.

At low frequencies, the flux penetrates through the upper laminations. The induced currents are almost uniformly distributed over the available surface, and are too weak to oppose the field.

For higher frequencies, the flux is pushed towards the edges of the laminations. The fringing flux causes larger eddy currents only in the first few sheets closest to the excitation winding. The field coming from those currents opposes the fringing field, reducing the induced voltage in the search coil. Above a sufficiently high frequency (corresponding to about 1000 RPM in the considered machine), the flux is almost completely flowing at the edges, causing almost no change any more in the induced voltage. The figure again shows the more or less double amplitude of the induced voltage at full load, compared to no-load. In figure 4.5 of chapter 4, it is also observed that for perpendicular flux coming from the excitation coil, higher frequencies cause higher losses. Higher losses for higher frequencies, means higher opposing fringing fields.

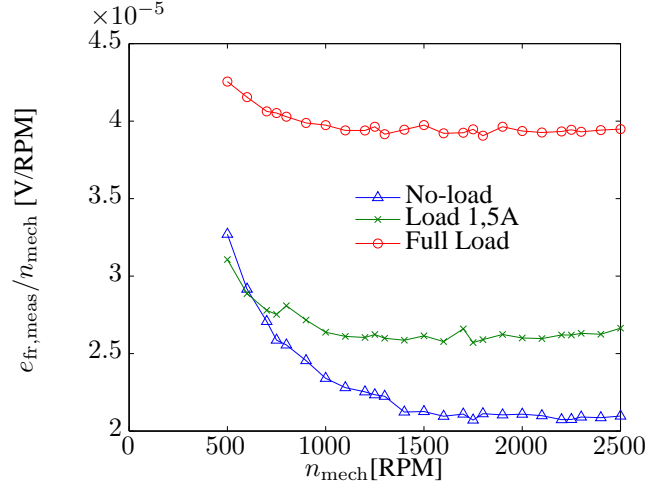


Figure 5.39: Measured *emf* in the fringing flux search coil $e_{\text{fr,meas}}$ in function of the mechanical speed divided by the mechanical speed n_{mech} .

5.9 Fringing flux as a function of airgap width

When the airgap width increases, the reluctance for the main flux increases. For this reason, the ratio between the reluctance for the main flux and the reluctance of the fringing flux decreases. The result is that more fringing flux occurs, as can be seen in figure 5.40: the induced voltage due to fringing flux is increasing for increasing airgap width. Five measurement points are considered. These measurements are very difficult, because they suffer from certain errors like asymmetries of the machine, also the precise thickness of the air gap is difficult to measure.

The effect of the airgap width can be seen easily from 2D FEM simulations. These are computations done by the 2D FEM described in chapter 2, where all laminations and the coatings in between them are modelled and meshed explicitly. The 2D geometry is shown in figure 4.4. The 2D FEM results are shown in figure 5.41a and 5.41b, where the magnetic vector potential in the out of plane direction is plotted for the simplified setup of chapter 4 for a frequency of 50 Hz, an excitation of 300 Atturns and an airgap of 1 mm and 5 mm respectively. It can be seen that more fringing flux is falling in perpendicularly to the plane of the lamination sheets for a larger air gap.

5.10 Conclusion

In this chapter, the losses of the complete axial flux permanent magnet synchronous machine were studied. At full load, the conventional iron losses of the prototype machine are about 40 W. In addition, there are copper losses of about 100 W and

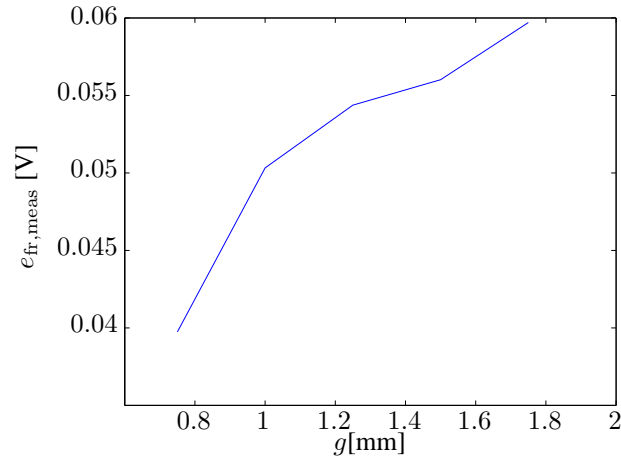


Figure 5.40: Measured *emf* in the fringing flux search coil $e_{fr,meas}$ in function of the airgap width g for a constant current of 5 A and a constant speed of 1000 RPM.

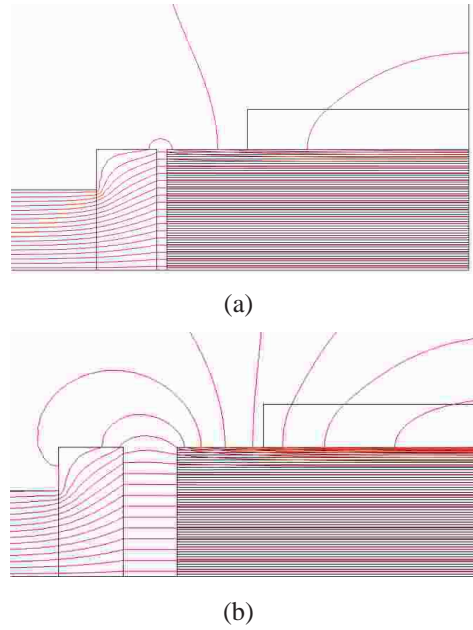
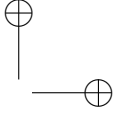
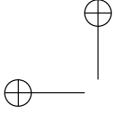
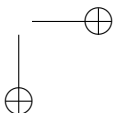
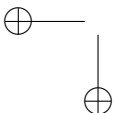


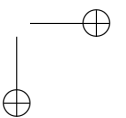
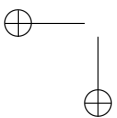
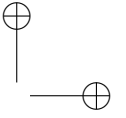
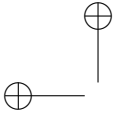
Figure 5.41: 2D field plot of the magnetic vector potential in the out of plane direction of the simplified setup described in chapter 4 with an airgap of (a) 1 mm, and (b) 5 mm.

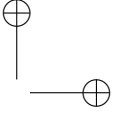
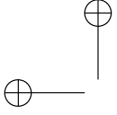


a number of smaller losses such as losses in the permanent magnets, bearings and windage losses. The fringing flux losses increase the iron losses, but are usually small. The losses increase with increasing stator current, and also with airgap width. They are more or less quadratic with the rotational speed.

The construction of the prototype is explained in detail: construction of the modular stator teeth, the rotors, and the assembly of the stator. A lot of effort was done by colleagues at Ghent University for finding the appropriate epoxy resin and casting technique, as the properties of the resin are very important: it should have high strength up to high temperature, a thermal expansion coefficient similar to the one of copper and aluminium, a high thermal conductivity, and a low viscosity. Many tests have been done to investigate cavities, cracks and behaviour at high temperature. Measurements on the prototype have shown that the chosen resin in combination with the aluminium housing with inward fins leads to an excellent thermal and mechanical behaviour of the machine.







Chapter 6

Concluding Remarks

6.1 Conclusion

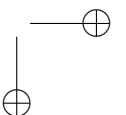
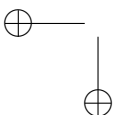
First, the working principle of axial flux permanent magnet machines is explained. After this, a comparison is made of competing topologies. Out of this comparison, the YASA topology is selected because of its advantages: modular construction, high power density and high efficiency. The construction of the YASA topology has been explained.

The second part of this work was dedicated to the behaviour of eddy currents in laminations and the influence of several electromagnetic parameters. Skin effect and penetration depth are studied in a stack of laminates. The field models used in this research, together with their model requirements were discussed: 2D FEM, 2D multislice, 3D FIT and 3D FEM.

The third part studied the magnetic characteristics of the materials and the losses in these materials: silicon steel (grain oriented and non-oriented), soft magnetic composite and ferromagnetic wire. Several homogenization techniques were compared in order to model the laminated materials in finite element models.

The following chapter presented a detailed study of the losses caused by fringing flux coming from the armature reaction on a simplified non-rotating setup, consisting of two tooth coils and a closing yoke. The validated field simulations give a very good image of the cause and the behaviour of fringing flux losses coming from the armature reaction. The last part of this chapter discusses three approaches for reducing these losses. The first method directly restricts the eddy-current losses by segmenting the lamination surface. The second method deflects the fringing flux by using Soft Magnetic Composite (SMC). The third method magnetically short-circuits the fringing flux using ferromagnetic wires. Here the magnetic characterisation from chapter 3 is included in the modelling.

The last chapter presented a study of the losses caused by fringing flux coming from the armature reaction and the permanent magnets of the complete axial flux machine. The study is done as a function of several parameters such as rotational



speed and airgap size. In addition, in contrast to several cited papers that consider no-load only, the influence of the stator current is investigated. In the last sections of the chapter, we consider first the no-load situation. Here, the fringing flux losses are caused only by the rotating permanent magnets. Then, full load is considered. At full load, the stator currents cause additional fringing fluxes. Finally, the effect of speed and air gap thickness is explained.

6.2 Recommendation for future research

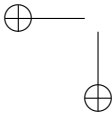
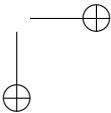
In the future, further research on fringing fluxes can be done. In this PhD, the influence of a number of parameters on fringing flux loss was done: stator current amplitude, airgap thickness, combination of several techniques to reduce fringing flux losses. Further research can be focussed on the influence of several parameters that were not studied in this work: the stack height, the stator slot openings, the magnetic material grade, the geometry of the coil end windings, ...

Another further research activity will be on the production methodology of the YASA machine. As low cost is very important in commercial motors, it is crucial to find construction techniques suitable for mass production. Several practical problems must be solved: the accurate positioning of the stator modules during stator assembly, the casting process, the connection of the wires of the several stator modules,... For example, in the prototype, this connection is done manually by soldering. In mass production however, an automated solution is required, e.g. via busbars or specially designed printed circuit boards.

A last topic is the further research on the thermal behaviour of the machine. A lot of research is done already in the framework of other PhDs, but the future study may focus on very high temperatures, in combination with the mechanical behaviour. Indeed, a machine with high power density is usually a machine that can operate at higher temperature than conventional machines (typically 155°C). This is only possible if all components (enamelled wire, magnets, resins,...) are functioning properly at these temperatures. Here, the epoxy resins play a crucial role. Further testing of the properties of the resins is required, making sure that strong temperature gradients in the machine do not cause excessive mechanical stress or cracks in the machine. Also resins should be studied with good mechanical properties at these high temperatures.



Bibliography

- [1] P. Waide and C. U. Brunner, “Energy-efficiency policy opportunities for electric motor-driven systems,” *International Energy Agency Working Paper*, 2011.
 - [2] IEC, “Iec e-tech,” www.iectech.org.
 - [3] A. Van den Bossche, “Combined heat power system,” Mar. 18 2014, uS Patent App. 8/674,525.
 - [4] A. Parviainen *et al.*, “Design of axial-flux permanent-magnet low-speed machines and performance comparison between radial-flux and axial-flux machines,” *PhD dissertation, Acta Universitatis Lappeenrantaensis*, 2005.
 - [5] F. Libert, “Design, optimization and comparison of permanent magnet motors for a low-speed direct-driven mixer,” *Licentiate Thesis, Royal Institute of Technology, TRITA-ETS-2004-12, ISSN-1650-674x, Stockholm*, 2004.
 - [6] F. Sahin, A. Tuckey, and A. Vandenput, “Design, development and testing of a high-speed axial-flux permanent-magnet machine,” in *Industry Applications Conference, 2001. Thirty-Sixth IAS Annual Meeting. Conference Record of the 2001 IEEE*, vol. 3. IEEE, 2001, pp. 1640–1647.
 - [7] H. Vansompel, “Design of an energy efficient axial flux permanent magnet machine,” *Ph.D. dissertation, Ghent University*, 2013.
 - [8] J. Gieras, R. Wang, and M. Kamper, *Axial Flux Permanent Magnet Brushless Machines*, 1st ed. Kluwer Academic publishers, Dordrecht, 2005.
 - [9] M. Aydin, S. Huang, and T. Lipo, “Axial flux permanent magnet disc machines: A review,” in *Symposium on Power Electronics, Electrical Drives, Automation, and Motion (SPEEDAM)*, 2004, pp. 61–71.
 - [10] F. Caricchi, F. Crescimbeni, O. Honorati, G. L. Bianco, and E. Santini, “Performance of coreless-winding axial-flux permanent-magnet generator with power output at 400 hz, 3000 r/min,” *IEEE Transactions on Industry Applications*, vol. 34, no. 6, pp. 1263–1269, 1998.
- 
- 

- [11] S. M. Hosseini, M. Agha-Mirsalim, and M. Mirzaei, "Design, prototyping, and analysis of a low cost axial-flux coreless permanent-magnet generator," *IEEE Transactions on Magnetics*, vol. 44, no. 1, pp. 75–80, 2008.
- [12] M. J. Kamper, R.-J. Wang, and F. G. Rossouw, "Analysis and performance of axial flux permanent-magnet machine with air-cored nonoverlapping concentrated stator windings," *IEEE Transactions on Industry Applications*, vol. 44, no. 5, pp. 1495–1504, 2008.
- [13] S. Huang, M. Aydin, and T. A. Lipo, "Torus concept machines: pre-prototyping design assessment for two major topologies," in *Industry Applications Conference, 2001. Thirty-Sixth IAS Annual Meeting. Conference Record of the 2001 IEEE*, vol. 3. IEEE, 2001, pp. 1619–1625.
- [14] T. Woolmer and M. McCulloch, "Analysis of the yokeless and segmented armature machine," *IEEE International Electric Machines & Drives Conference*, vol. 1, pp. 704–708, 3–6 May 2007.
- [15] T. Woolmer, "Electric machine-flux," Feb. 12 2010, uS Patent App. 13/148,863.
- [16] W. Fei, P. Luk, and K. Jinupun, "A new axial flux permanent magnet segmented-armature-torus machine for in-wheel direct drive applications," in *Power Electronics Specialists Conference, 2008. PESC 2008. IEEE*. IEEE, 2008, pp. 2197–2202.
- [17] A. Di Gerlando, G. Foglia, M. F. Iacchetti, and R. Perini, "Axial flux pm machines with concentrated armature windings: Design analysis and test validation of wind energy generators," *IEEE Transactions on Industrial Electronics*, vol. 58, no. 9, pp. 3795–3805, 2011.
- [18] H. Vansompel, P. Sergeant, L. Dupré, and A. Van den Bossche, "Improving the torque output in radial- and axial-flux permanent-magnet synchronous machines with concentrated windings by using a combined wye-delta connection," in *2011 IEEE International Electric Machines Drives Conference (IEMDC)*, May 2011, pp. 936–941.
- [19] A. Parviainen, J. Pyrhönen, and P. Kontkanen, "Axial flux permanent magnet generator with concentrated winding for small wind power applications," in *2005 IEEE International Conference on Electric Machines and Drives*. IEEE, 2005, pp. 1187–1191.
- [20] F. Caricchi, F. G. Capponi, F. Crescimbin, and L. Solero, "Experimental study on reducing cogging torque and no-load power loss in axial-flux permanent-magnet machines with slotted winding," *IEEE Transactions on Industry Applications*, vol. 40, no. 4, pp. 1066–1075, 2004.

- [21] A. Di Gerlando, G. Foglia, M. Iacchetti, and R. Perini, "Evaluation of manufacturing dissymmetry effects in axial flux permanent-magnet machines: Analysis method based on field functions," *IEEE Transactions on Magnetics*, vol. 48, no. 2, pp. 1995–2008, 2012.
- [22] R. D. Stefano and F. Marignetti, "A comparison between soft magnetic cores for axial flux pm synchronous machines," in *2012 XXth International Conference on Electrical Machines*, Sept 2012, pp. 1922–1927.
- [23] O. Maloberti, R. Figueredo, C. Marchand, Y. Choua, D. Condamin, L. Kobylanski, and E. Bommé, "3-d-2-d dynamic magnetic modeling of an axial flux permanent magnet motor with soft magnetic composites for hybrid electric vehicles," *IEEE Transactions on Magnetics*, vol. 50, no. 8201511, pp. 1–11, June 2014.
- [24] H. De Gersem, S. Vanaverbeke, and G. Samaey, "Three-Dimensional-Two-Dimensional coupled model for eddy currents in laminated iron cores," *IEEE Transactions on Magnetics*, vol. 48, no. 2, pp. 815–818, feb 2012.
- [25] R. Stoll, *The Analysis of Eddy Currents*, 1st ed. Oxford: Clarendon Press, 1974.
- [26] K. Shima, T. Murai, T. Fukami, Y. Furukawa, and A. Komura, "Measurement and analysis of in-plane eddy current in lamination steel using a new tester," in *2012 XXth International Conference on Electrical Machines (ICEM)*, Sept 2012, pp. 1771–1777.
- [27] K. Preis, O. Bíró, and I. Tičar, "Fem analysis of eddy current losses in non-linear laminated iron cores," *IEEE Transactions on Magnetics*, vol. 41, pp. 1412–1415, 2005.
- [28] T. Nakano, Y. Kawase, T. Yamaguchi, M. Nakamura, and N. Nishikawa, "3-d finite element analysis of eddy current in laminated cores of the interior permanent-magnet motor," *IEEE Transactions on Magnetics*, vol. 49, pp. 1945–1948, 2013.
- [29] H. Vansompel, P. Sergeant, L. Dupré, and A. Van den Bossche, "Axial-Flux PM Machines With Variable Air Gap," *IEEE Transactions on Industrial Electronics*, vol. 61, no. 2, pp. 730–737, 2014.
- [30] P. Sergeant, H. Vansompel, and L. Dupré, "Influence of stator slot openings on losses and torque in axial flux permanent magnet machines," *Mathematics and Computers in Simulation*, vol. 130, pp. 22–31, 2016.
- [31] F. Marketos, D. Marnay, and T. Ngnegueu, "Experimental and numerical investigation of flux density distribution in the individual packets of a 100 kVA

- transformer core,” *IEEE Transactions on Magnetism*, vol. 48, no. 4, pp. 1677–1680, April 2012.
- [32] J. Lammeraner and M. Staffl, *Eddy currents*, 1st ed. ILIFFE Books Ltd., London, 1966.
- [33] J. R. Brauer and Z. J. Cendes, “Laminated steel eddy-current loss versus frequency computed using finite elements,” *IEEE Transactions on Industry Applications*, vol. 36, pp. 1132–1137, 2000.
- [34] A. Barchanski, T. Genstys, C. Degen, I. Fischer, and W. Elsasser, “Efficient calculation of current densities in the human body induced by arbitrary shaped, low-frequency magnetic field sources,” *Journal of Computational Physics*, vol. 214, pp. 81–95, 2006.
- [35] P. Zhou, D. Lin, C. Lu, N. Chen, and M. Rosu, “A new algorithm to consider the effects of core losses on 3-d transient magnetic fields,” *IEEE Transactions on Magnetism*, vol. 50, no. 2, pp. 365–368, Feb 2014.
- [36] J. Wang, H. Lin, Y. Huang, and X. Sun, “A new formulation of anisotropic equivalent conductivity in laminations,” *IEEE Transactions on Magnetism*, vol. 47, pp. 1378–1381, 2011.
- [37] K. Muramatsu, T. Okitsu, H. Fujitsu, and F. Shimanoe, “Method of nonlinear magnetic field analysis taking into account eddy current in laminated core,” *IEEE Transactions on Magnetism*, vol. 40, pp. 896–899, 2004.
- [38] J. Gyselinck, L. Vandevelde, and J. Melkebeek, “Calculation of eddy currents and associated losses in electrical steel laminations,” *IEEE Transactions on Magnetism*, vol. 35, pp. 1191–1194, 1999.
- [39] P. Silvester and R. Ferrari, *Finite Elements for Electrical Engineers*, 2nd ed. Cambridge: Cambridge University Press, 1996.
- [40] L. Krähenbühl and D. Muller, “Thin layers in electrical engineering. example of shell models in analyzing eddy-currents by boundary and finite element methods,” *IEEE Transactions on Magnetism*, vol. 29, no. 5, pp. 1450–1455, 1993.
- [41] C. Poignard, P. Dular, R. Perrussel, L. Krähenbühl, L. Nicolas, and M. Schatzman, “Approximate conditions replacing thin layers,” *IEEE Transactions on Magnetism*, vol. 44, no. 6, pp. 1154–1157, 2008.
- [42] M. Clemens, “Large systems of equations in a discrete electromagnetism: formulations and numerical algorithms,” *IEE Proceedings - Science, Measurement and Technology*, vol. 152, no. 2, pp. 50–72, March 2005.

- [43] R. Schuhmann, P. Schmidt, and T. Weiland, "A new whitney-based material operator for the finite-integration technique on triangular grids," *IEEE Transactions on Magnetics*, vol. 38, no. 2, pp. 409–412, Mar 2002.
- [44] O. Biro and K. Preis, "Finite element analysis of 3-d eddy currents," *IEEE Transactions on Magnetics*, vol. 26, pp. 418–423, Mar 1990.
- [45] G. Bertotti, *Hysteresis In Magnetism*, 1st ed. Academic Press, 1998.
- [46] E. Barbisio, F. Fiorillo, and C. Ragusa, "Predicting loss in magnetic steels under arbitrary induction waveform and with minor hysteresis loops," *IEEE Transactions on Magnetics*, vol. 40, no. 4, pp. 1810–1819, July 2004.
- [47] H. Haas and F. Schmellebeck, "Approximation of nonlinear anisotropic magnetization characteristics," *IEEE Transactions on Magnetics*, vol. 28, no. 2, pp. 1255–1258, Mar 1992.
- [48] J. Gyselinck, "Twee-dimensionale dynamische eindig-elementenmodellering van statische en roterende elektromagnetische energieomzetters," Ph.D. dissertation, Ghent University, 2000.
- [49] F. Fiorillo, L. Dupré, C. Appino, and A. Rietto, "Comprehensive model of magnetization curve, hysteresis loops, and losses in any direction in grain-oriented fe-si," *IEEE Transactions on Magnetics*, vol. 38, no. 3, pp. 1467–1476, 2002.
- [50] A. Schoppa and P. Delarbre, "Soft magnetic powder composites and potential applications in modern electric machines and devices," *IEEE Transactions on Magnetics*, vol. 50, no. 4, pp. 1–4, April 2014.
- [51] L. Dupré, O. Bottauscio, M. Chiampi, M. Repetto, and J. Melkebeek, "Modeling of electromagnetic phenomena in soft magnetic materials under unidirectional time periodic flux excitations," *IEEE Transactions on Magnetics*, vol. 35, no. 5, pp. 4171–4184, Sep 1999.
- [52] T. Nakata, N. Takahashi, and K. Fujiwara, "Investigation of a model to verify softwares for 3-d nonlinear eddy current analysis," *IEEE Transactions on Magnetics*, vol. 26, no. 2, pp. 501–504, Mar 1990.
- [53] P. Hahne, R. Dietz, B. Rieth, and T. Weiland, "Determination of anisotropic equivalent conductivity of laminated cores for numerical computation," *IEEE Transactions on Magnetics*, vol. 32, pp. 1184–1187, May 1996.
- [54] S. Koch, H. D. Gersem, T. Weiland, E. Fischer, and G. Moritz, "Transient 3d finite element simulations of the sis100 magnet considering anisotropic, nonlinear material models for the ferromagnetic yoke," *IEEE Transactions on Applied Superconductivity*, vol. 18, pp. 1601–1604, June 2008.

- [55] I. Niyonzima, R. V. Sabariego, P. Dular, and C. Geuzaine, "Nonlinear computational homogenization method for the evaluation of eddy currents in soft magnetic composites," *IEEE Transactions on Magnetics*, vol. 50, pp. 61–64, 2014.
- [56] H. Kaimori, A. Kameari, and K. Fujiwara, "FEM computation of magnetic field and iron loss in laminated iron core using homogenization method," *IEEE Transactions on Magnetics*, vol. 43, no. 4, pp. 1405–1408, apr 2007.
- [57] WAASNER, "Waasner," www.waasner.de.
- [58] Z. Cheng, N. Takahashi, B. Forghani, G. Gilbert, Z. J., L. Liu, Y. Fan, X. Zhang, Y. Du, and J. Wang, "Analysis and Measurements of Iron Loss and Flux Inside Silicon Steel Laminations," *IEEE Transactions on Magnetics*, vol. 45, no. 3, pp. 1222–1225, 2009.
- [59] M. Bali and A. Muetze, "Influences of co2 laser, fkl laser, and mechanical cutting on the magnetic properties of electrical steel sheets," *IEEE Transactions on Industry Applications*, vol. 51, no. 6, pp. 4446–4454, Nov 2015.
- [60] G. Cvetkovski and L. Petkovska, "Performance improvement of pm synchronous motor by using soft magnetic composite material," *IEEE Transactions on Magnetics*, vol. 44, no. 11, pp. 3812–3815, Nov 2008.
- [61] A. Parviainen, M. Niemelä, and J. J. Pyrhönen, "Modeling of axial permanent-magnet machines," *IEEE Transactions on Industry Applications*, vol. 40, no. 5, pp. 1333–1340, 2004.
- [62] Y. Zhang, W. Ma, J. Lu, Z. Sun, J. Xu, and W. Li, "A new approach to research the transverse edge effect in linear induction motor considering the edge fringing flux," *IEEE Transactions on Magnetics*, vol. 47, no. 11, pp. 4660–4668, Nov 2011.
- [63] A. Labak and N. C. Kar, "Designing and prototyping a novel five-phase pancake-shaped axial-flux srm for electric vehicle application through dynamic fea incorporating flux-tube modeling," *IEEE Transactions on Industry Applications*, vol. 49, no. 3, pp. 1276–1288, May 2013.
- [64] L. Wang, W. Chen, D. Tao, W. Li, and B. Ge, "Research on the impact of screen properties on eddy current and flux in end region of a large air-cooled turbo-generator," *IEEE Transactions on Energy Conversion*, vol. 31, no. 1, pp. 218–227, March 2016.
- [65] K. Yamazaki, Y. Yamato, H. Mogi, C. Kaido, A. Nakahara, K. Takahashi, K. Ide, and K. Hattori, "In-plane eddy current analysis for end and interior stator core packets of turbine generators," in *2008 18th International Conference on Electrical Machines*, Sept 2008, pp. 1–6.

- [66] R. Lin, A. Haavisto, and A. Arkkio, "Axial flux and eddy-current loss in active region of a large-sized squirrel-cage induction motor," *IEEE Transactions on Magnetics*, vol. 46, no. 11, pp. 3933–3938, Nov 2010.
- [67] B. Scheerlinck, H. D. Gersem, and P. Sergeant, "Reducing losses due to fringing flux in an axial-flux permanent-magnet synchronous machine," *IEEE Transactions on Magnetics*, vol. 52, no. 10, pp. 1–8, Oct 2016.
- [68] H. Vansompel, P. Sergeant, and L. Dupré, "Optimized design considering the mass influence of an Axial Flux Permanent-Magnet Synchronous Generator with Concentrated Pole Windings," *IEEE Transactions on Magnetics*, vol. 46, no. 12, pp. 4101–4107, 2010.
- [69] D. Kowal, P. Sergeant, L. Dupré, and A. Van den Bossche, "Comparison of nonoriented and grain-oriented material in an axial flux permanent-magnet machine," *IEEE Transactions on Magnetics*, vol. 46, no. 2, pp. 279–285, 2010.
- [70] H. Vu Xuan, D. Lahaye, H. Polinder, and J. Ferreira, "Influence of stator slotting on the performance of permanent-magnet machines with concentrated windings," *IEEE Transactions on Magnetics*, vol. 49, no. 2, pp. 929–938, 2013.
- [71] F. G. Capponi, G. D. Donato, G. A. Rivellini, and F. Caricchi, "Fractional-slot concentrated-winding axial-flux permanent-magnet machine with tooth-wound coils," *IEEE Transactions on Industry Applications*, vol. 50, no. 4, pp. 2446–2457, July 2014.
- [72] H. Vansompel, P. Sergeant, L. Dupré, and A. Van den Bossche, "A combined wye-delta connection to increase the performance of axial-flux pm machines with concentrated windings," *IEEE Transactions on Energy Conversion*, vol. 27, no. 2, pp. 403–410, June 2012.
- [73] H. Vansompel, A. Rasekh, A. Hemeida, J. Vierendeels, and P. Sergeant, "Coupled electromagnetic and thermal analysis of an axial flux pm machine," *IEEE Transactions on Magnetics*, vol. 51, no. 11, pp. 1–4, 2015.
- [74] A. Hemeida, P. Sergeant, and H. Vansompel, "Comparison of methods for eddy current loss computations with and without reaction field considerations in axial flux PMSM," *IEEE Transactions on Magnetics*, vol. 51, no. 9, p. 8107511, 2015.
- [75] A. Rasekh, P. Sergeant, and J. Vierendeels, "Development of Correlations for Windage Power Losses Modeling in an Axial Flux Permanent Synchronous Machine with Geometrical Features of the magnets," *Energies*, vol. 9, no. Art. 1009, 2016.

- [76] H. Vansompel, P. Sergeant, L. Dupré, and A. Van den Bossche, "Evaluation of simple lamination stacking methods for the teeth of an axial flux permanent-magnet synchronous machine with concentrated stator windings," *IEEE Transactions on Magnetics*, vol. 48, no. 2, pp. 999–1002, 2012.
- [77] A. Rasekh, P. Sergeant, and J. Vierendeels, "Fully predictive heat transfer coefficient modeling of an axial flux permanent magnet synchronous machine with geometrical parameters of the magnets," *Applied Thermal Engineering*, vol. 110, pp. 1343–1357, 2017.
- [78] Y. C. Chong, E. J. E. Subiabre, M. A. Mueller, J. Chick, D. A. Staton, and A. S. McDonald, "The ventilation effect on stator convective heat transfer of an axial-flux permanent-magnet machine," *IEEE Transactions on Industrial Electronics*, vol. 61, no. 8, pp. 4392–4403, 2014.
- [79] M. Polikarpova, P. Ponomarev, P. Lindh, I. Petrov, W. Jara, V. Naumanen, J. Tapia, and J. Pyrhönen, "Hybrid cooling method of axial-flux permanent-magnet machines for vehicle applications," *IEEE Transactions on Industrial Electronics*, vol. 62, no. 12, pp. 7382–7390, 2015.
- [80] S. Nategh, A. Krings, O. Wallmark, and M. Leksell, "Evaluation of impregnation materials for thermal management of liquid-cooled electric machines," *IEEE Transactions on Industrial Electronics*, vol. 61, no. 11, pp. 5956–5965, 2014.
- [81] M. Galea, C. Gerada, T. Raminosoa, and P. Wheeler, "A thermal improvement technique for the phase windings of electrical machines," *IEEE Transactions on Industry Applications*, vol. 48, no. 1, pp. 79–87, 2012.
- [82] M. Andriollo, M. De Bortoli, G. Martinelli, A. Morini, and A. Tortella, "Analysis of the air-gap asymmetry in axial-flux permanent magnet generators," in *IEEE International Electric Machines and Drives Conference, 2009. IEMDC'09*. IEEE, 2009, pp. 344–351.